Transport of Water, Vapour, Heat and Solutes in Concrete for Storing Radioactive Waste

PhD Thesis

Hydrogeology Group (UPC-CSIC)

Department of Civil and Environmental Engineering,

Universitat Politècnica de Catalunya (UPC)

Institute of Environmental Assessment and Water Research (IDAEA), CSIC.

M. Carme Chaparro Sánchez

Advisor: Maarten W. Saaltink

Co-advisor: Josep M. Soler Matamala

January, 2016

Als qui m'han aportat

algun dels granets de sorra

de la duna que conforma aquesta tesi.

Abstract

Cementitious materials are used as barriers in radioactive waste storage. Hence, transport processes in this kind of material are important. The objective of this thesis is to improve the understanding of transport of water (liquid and gas), heat and solutes in concrete. This is applied to the concrete from the low-and intermediate- level radioactive waste facility at El Cabril (Southern Spain). To do so, the following studies were done.

First, evaporation tests in concrete columns have been simulated in order to obtain thermo-hydraulic parameters. The conceptual model considers unsaturated liquid flow and transport of vapour and energy. The retention curve was estimated from relative humidity and gravimetric water content at the end of the tests. Relative permeability, thermal conductivity and tortuosity factor for vapour diffusion were obtained by calibrating the numerical model. Results show that the vapour diffusion is the dominant water transport process above an evaporation front and liquid advection is dominant below it.

Second, numerical models simulating the processes that take place inside the concrete cells have been carried out. Temperature and relative humidity measured by sensors in the cells and thermo-hydraulic parameters from laboratory tests have been used. Results show that temperature oscillations outside the cell create a temperature difference between the two sides of an air gap between the concrete containers and the wall of the cell. Water rises

from the phreatic level into the wall of the cell through capillary rise. Water evaporates at the hot side (wall of the cell in summer and containers in winter) and diffuses as vapour from the hot to the cold side. Condensation is produced at the cold side. Consequently, water runs off to the drain. In order to avoid this phenomenon, various scenarios have been studied.

Third, a laboratory-scale tracer test in concrete has been carried out using a high entry pressure. The conceptual model considers matrix diffusion between a mobile pore domain, were water can flow, and an immobile zone with only diffusion. Three geometries have been compared, considering the immobile zone as slabs, spheres or tubes. Porosity of the mobile zone and characteristic time were estimated by calibrating the model results to the measured breakthrough curves of deuterium and bromide. The calculated values show that the characteristic time depends on the geometry, and a similar porosity of the mobile zone was estimated for all geometries. Bromide behaviour could not be reproduced even when linear retardation was applied.

Finally, reactive transport models of concrete has been applied in order to study the changes in mineralogy produced during the performance of the tracer test. All minerals are considered in the immobile zone. The cement paste consists of alite, belite, gypsum, calcite, C-S-H gel, portlandite and ettringite. The aggregates are composed of quartz. Overall model results show mineral dissolution of alite, belite, gypsum and quartz and precipitation of C-S-H gel, portlandite, ettringite and calcite. The model shows that the porosity in the immobile zone increases due to mineral dissolution. However, the conceptual model used cannot reproduce the changes in permeability.

Resum

Els materials fets amb ciment s'utilitzen en l'emmagatzematge de residus radioactius. Per tant, els processos de transport en aquest tipus de materials són importants. L'objectiu d'aquesta tesi és millorar la comprensió del transport d'aigua (en fase líquida i gasosa), calor i soluts en el formigó. Concretament l'utilitzat en l'emmagatzematge de residus radioactius de mitja i baixa activitat del centre d'emmagatzematge El Cabril (Sud d'Espanya). Per tal de dur a terme aquest objectiu s'han realitzat els estudis que es detallen a continuació.

En primer lloc, s'han simulat assaigs d'evaporació en formigó per tal d'obtenir-ne els paràmetres termo-hidràulics. El model conceptual considera flux en medi no saturat, transport de vapor i d'energia. S'ha estimat la corba de retenció a partir de les dades d'humitat relativa i contingut gravimètric del final de l'assaig. Mitjançant la calibració del model numèric, s'ha obtingut la permeabilitat relativa, la conductivitat tèrmica i el factor de tortuositat de la difusió de vapor. Els resultats del model numèric mostren que el procés de difusió de vapor és dominant per sobre d'un front d'evaporació i l'advecció de líquid ho és per sota d'aquest front.

En segon lloc, s'han fet models numèrics per simular els processos que tenen lloc en les estructures d'emmagatzematge de residus. S'han utilitzat dades de temperatur i humitat relativa mesurades per sensors en les cel·les d'emmagatzematge, i també paràmetres

termo-hidràulics obtinguts a partir d'assaigs de laboratori. Els resultats mostren que les oscil·lacions de temperatura de l'exterior creen una diferencia de temperatura dins la cel·la d'emmagatzematge. Concretament, entre els dos costats d'un espai d'aire que hi ha entre la paret de la cel·la i els contenidors. L'aigua ascendeix des del nivell freàtic a la paret de la cel·la a través d'ascens capil·lar. Es produeix evaporació al costat calent (paret de la cel·la a l'estiu i contenidor a l'hivern), i es produeix condensació al costat fred. Com a conseqüència, es recull aigua al desguàs. S'han estudiat diferents casos per evitar aquest fenomen.

En tercer lloc, s'ha realitzat un assaig de traçadors en formigó, a escala de laboratori, on s'han utilitzat elevades pressions d'infiltració. El model conceptual considera difusió en la matriu, entre una zona mòbil on l'aigua pot fluir i una zona immòbil on només hi ha difusió. S'han comparat tres geometries, considerant la zona immòbil com a blocs, esferes o tubs. La porositat de la zona mòbil i el temps característic s'han estimat calibrant el model numèric amb les corbes d'arribada de deuteri i bromur. Els resultats mostren que el temps característic depèn de la geometria utilitzada, i s'obté una porositat de la zona mòbil similar per a totes les geometries. El comportament del bromur no es pot reproduir encara que s'apliqui un retard lineal.

Finalment, s'han utilitzat models de transport reactiu en formigó per estudiar els canvis en la mineralogia produïts durant l'assaig de traçadors. Tots els minerals estan en la zona immòbil. El ciment està format per alita, bel·lita, guix, calcita, gel C-S-H, portlandita i ettringita. Els agregats estan formats per quars. Els resultats mostren dissolució d'alita, bel·lita, guix i quars, i precipitació de gel C-S-H, portlandita, ettringita i calcita. El model mostra que la porositat de la zona immòbil augmenta degut a la dissolució de minerals. No obstant, el model conceptual utilitzat no pot reproduir els canvis en la permeabilitat.

Resumen

Los materiales cementicios se utilizan para el almacenamiento de residuos radiactivos. Por lo tanto, los procesos de transporte en este tipo de materiales son importantes. El objetivo de esta tesis es mejorar la comprensión del transporte de agua (en fase líquida y gaseosa), calor y solutos en el hormigón. Concretamente el que se utiliza en el almacenamiento de residuos radiactivos de media y baja actividad del centro de almacenamiento El Cabril (Sur de España). Para llevar a cabo este objetivo se han realizado los siguientes estudios.

En primer lugar, se han simulado ensayos de evaporación en hormigón con el fin de obtener los parámetros termo-hidráulicos. El modelo conceptual considera flujo en medio no saturado, transporte de vapor y de energía. Se ha estimado la curva de retención a partir de los datos de humedad relativa y contenido gravimétrico del final del ensayo. Mediante la calibración del modelo numérico, se ha obtenido la permeabilidad relativa, la conductividad térmica y el factor de tortuosidad de la difusión de vapor. Los resultados del modelo numérico muestran que el proceso de difusión de vapor es dominante por encima de un frente de evaporación y la advección de líquido lo es por debajo de este frente.

En segundo lugar, se han hecho modelos numéricos para simular los procesos que tienen lugar en las estructuras de almacenamiento de residuos. Se han utilizado datos de temperatura y humedad relativa medidas por sensores en las celdas de almacenamiento, y también

parámetros termo-hidráulicos obtenidos a partir de ensayos de laboratorio. Los resultados muestran que las oscilaciones de temperatura del exterior crean una diferencia de temperatura dentro de la celda de almacenamiento. Concretamente, entre los dos lados de un espacio de aire que hay entre la pared de la celda y los contenedores. El agua asciende desde el nivel freático hacia la pared de la celda mediante ascenso capilar. Se produce evaporación del lado caliente (pared de la celda en verano y contenedor en invierno), y se produce condensación en el lado frío. Como consecuencia, se recoge agua en el desagüe. Se han estudiado diferentes casos para evitar este fenómeno.

En tercer lugar, se ha realizado un ensayo de trazadores en hormigón, a escala de laboratorio, utilizando elevadas presiones de infiltración. El modelo conceptual considera difusión en la matriz, entre una zona móvil donde el agua puede fluir y una zona inmóvil donde sólo hay difusión. Se han comparado tres geometrías, considerando la zona inmóvil como bloques, esferas o tubos. La porosidad de la zona móvil y el tiempo característico se han estimado calibrando el modelo numérico con las curvas de llegada de deuterio y bromuro. Los resultados muestran que el tiempo característico depende de la geometría utilizada, y se obtiene una porosidad de la zona móvil similar para todas las geometrías. El comportamiento del bromuro no se puede reproducir aunque se aplique un retardo lineal.

Finalmente, se han utilizado modelos de transporte reactivo en hormigón para estudiar los cambios en la mineralogía producidos durante el ensayo de trazadores. Se considera que todos los minerales están en la zona inmóvil. El cemento está formado por alita, belita, yeso, calcita, gel CSH, portlandita y ettringita. Los agregados están formados por cuarzo. Los resultados muestran disolución de alita, belita, yeso y cuarzo, y precipitación de gel CSH, portlandita, ettringita y calcita. El modelo muestra que la porosidad de la zona inmóvil aumenta debido a la disolución de minerales. No obstante, el modelo conceptual no puede reproducir los cambios en la permeabilidad.

Agraïments

M'agradaria agrair al meu director de tesi Maarten Saaltink i al meu co-director Josep M. Soler, per haver-me donat l'oportunitat de treballar i aprendre al seu costat, també per la seva ajuda i dedicació.

A l'Urs Mäder per haver-me obert les portes del seu laboratori i per haver col·laborat en aquesta tesi.

Als co-autors dels articles Luit Jan Slooten i María Victoria Villar, i amb els qui he compartit docència Marcel Hürlimann, Jose Moya i Joan Martínez, perquè ha estat un plaer treballar amb vosaltres.

Al Florian Dolder, Andreas Jenni i Jordi Illa per la seva ajuda al laboratori.

A la meva família, als amics, companys del Grup d'Hidrologia Subterrània, del Departament d'Enginyeria del Terreny i del Departament de Física Aplicada que han estat al meu costat quan els he necessitat. També, als meus companys de la Universitat de Berna per haver-me fet sentir com a casa des del primer dia.

Table of Contents

List of Figures

List of Tables

Chapter 1

Introduction

1.1 Motivation

Radioactive waste is a hazardous material due to its radioactivity, which is harmful and potentially lethal. Therefore, it requires special care for its final disposal. Radioactive waste can be divided into waste of low, intermediate and high level of radioactivity. The radioactive waste of low and intermediate activity level is material contaminated with radioactive isotopes, which has a half-life lower than 30 years. This kind of radioactive waste contains concentrations of medium-life radionuclide (isotopes emitting alpha and beta radiation) and low concentrations of long-life radionuclide (alpha emissions). After several hundreds of years they cease to be dangerous. This waste comes from industries, hospitals, research laboratories and nuclear power plants. There is also radioactive waste of very low activity level that contains small amounts of radioactivity (lower than 100 Bq/g), which does not need special treatment for their management. Another kind of radioactive waste is the waste with high activity level, from the nuclear fuel used in nuclear power plants and other

materials with high level of radioactivity. They contain large concentrations of long-life radionuclide, which generate large amounts of heat. They have a half-life higher that 30 years and remain dangerous for several thousands of years.

El Cabril is the radioactive waste disposal facility of Spain. The low and intermediate radioactive waste is stored there since 1961. It is located in Sierra de Albarrana in Córdoba (South of Spain). The installation consists of two platforms used to store the low and intermediate activity level of radioactive waste. Another platform is used for storing very low radioactive waste. (Figure 1.1).

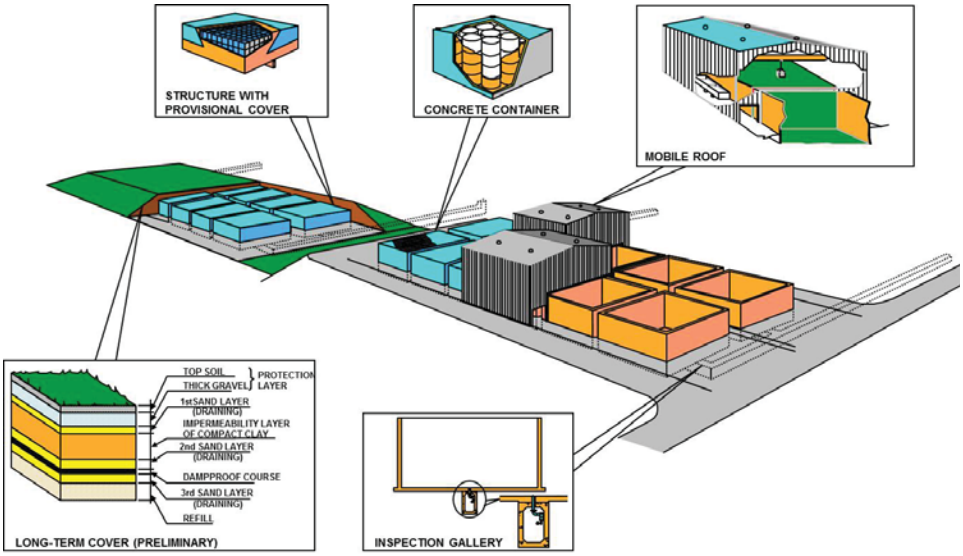

Figure 1.1: Scheme of the installation El Cabril, where the low and intermediate radioactive waste is stored (*Zuloaga et al.*, 2006).

First, the waste, which is a solid material, is stored in metal drums. Second, they are placed in concrete containers that measure 2.25 m by 2.25 m by 2.20 m. When the containers are full, they are filled with mortar. Third, the containers are placed in a concrete cell. Each cell measures 19.3 m by 23.8 m by 9 m and can store 1000 m^3 of waste. When the cell is completely full it is sealed with a concrete slab at the top. Finally, it is painted using

a waterproof paint. Each cell has a drain at the center, which is accessible through a gallery. This gallery connects all the cells in the platform. The cells are partly buried (3 m) into the underlying rock. The rest is exposed to the atmosphere with its temperature oscillations. El Cabril has 28 concrete cells storing the radioactive waste. In the future, when all the cells are full, the whole facility will be protected with a multilayer cover (*Gran-Esforzado*, 2015). It is foreseen that the repository stores the radioactive waste during 300 years under vigilance and control.

The first cell was sealed in 1992. From 2003 onwards, water is collected from the drain installed at the center of each cell, indicating flow of water within the cell. This occurred in two periods every year, the first one between August and October and the second one during the winter. The larger amount of water is collected in winter. The collected water contains between 3000 and 100000 Bq/l of Tritium. This phenomenon caused concern because the water transports radioactive contaminants and also the flow within the concrete could reduce its durability. For this reason ENRESA (Spanish Nuclear Waste Management Company) wanted to know the cause that produces this phenomenon. Several hypotheses were suggested. One of them was related to the rainwater, but there was no correlation between the rain and the periods of the collected water in the drain. Another hypothesis was the fact that junctions of the concrete could allow the infiltration of water. However, this hypothesis could not explain the quantity of collected water. Finally, the hypothesis proposed to explain this phenomenon consists of capillary rise from groundwater, evaporation and condensation within the cell, produced by temperature gradients caused by seasonal temperature fluctuations outside (*Saaltink et al.*, 2005; *Massana and Saaltink*, 2006; *Zuloaga et al.*, 2006; *Saaltink*, 2006; *Gamazo et al.*, 2007). A combination of several factors contributes to this phenomenon. The aquifer is approximately 3 m below the base of the cell and is hydraulically connected to the walls of the cell, allowing a capillary rise. The

concrete used to build the cells has a low intrinsic permeability and high water retention capacity. Hence, it contains water available for evaporation. A gap of air exists between the wall of the cell and the containers, causing a temperature difference which allows vapour diffusion.

With the aim of verifying this hypothesis, in 2006 some cells were monitored in order to measure the temperature and relative humidity inside and outside the cells. Moreover, in 2007, CIEMAT started laboratory test for the thermo-hydraulic characterization of the concrete used to built the cells.

1.2 Objective

The general objective of this thesis was to study the transport properties of water, vapour, heat and solutes in the concrete used to store the radioactive waste. To do so, this objective was divided in four specific objectives:

- The first objective was to obtain the thermo-hydraulic parameters of the concrete by modelling evaporation tests in non-isothermal conditions.
- The second was to study the processes that are taking place inside the cells by means of numerical models. The models take into account the measured temperature and relative humidity and the thermo-hydraulic parameters of the concrete.
- The third was to improve the understanding of conservative transport of solutes in concrete, considering processes like advection, dispersion, diffusion and also diffusion into a matrix, with pores filled with immobile water.
- The last objective was to study the reactive transport of solutes in the concrete em-

phasising the effect of matrix diffusion.

1.3 Thesis outline

This thesis is divided in six chapters, where the first one corresponds to this introduction. Then, there is one chapter for each specific objective, which are based on a published articles (chapters 2 and 4), an article under review (chapter 3) or in preparation for publication (chapter 5) in international journals. Finally, the last chapter gives the general conclusions.

Chapter 2 corresponds to the first objective, which consist of obtaining the thermo-hydraulic parameters of the concrete used for building the cells. The data of relative humidity and gravimetric water content from two evaporation test in non-isothermal conditions made by (*Villar et al.*, 2009) was used in order to obtain the drying retention curve of the concrete. The simulations of these evaporation test and their calibration by adjusting the model results to the experimental data are used to find thermo-hydraulic parameters, such as relative permeability, the tortuosity factor and the thermal conductivity.

Chapter 3 consist of modelling the processes that take place inside the cells taking into account the conceptual model of capillary rise from groundwater, evaporation and condensation within the cell produced by temperature gradients. Data of relative humidity and temperature measured by the sensors inside and outside the cells are taken into account. Also the thermo-hydraulic parameters obtained in the previous chapter are used. Furthermore, some possible scenarios are given to remediable and avoid the phenomenon that takes place in the cells.

Chapter 4 addresses the third objective, which consist of studying the conservative solute transport in concrete taking into account matrix diffusion between a mobile pore domain

(with advection, dispersion and diffusion) and an immobile zone (with diffusion). A tracer test in the concrete have been carried out using high entry pressure. A simulation of the test allowed the estimation of the porosity and other transport parameters by calibrating the model results to the measured breakthrough curves of the tracers.

Chapter 5 refers to the fourth objective that studies the changes in mineralogy in the concrete that takes place during the performance of the infiltration test. In the numerical model of the last chapter the geochemistry is added. It looks at the dissolution and precipitation of minerals of the cement paste (C-S-H gel , portlandite, ettringite, calcite and gypsum, together with residual alite and belite) and of the aggregates (quartz).

Chapter 6 summarizes the main contributions of this thesis.

Chapter 2

Characterization of Concrete by Calibrating Thermo-Hydraulic Multiphase Flow Models*

2.1 Introduction

Concrete allows building a large number of architecture and engineering structures. The majority of them are exposed to alternating dry and wet conditions affecting their durability. Thermo-hydraulic processes such as flow of liquid and gas in unsaturated conditions, transport of heat, vapour and dissolved salts, and evaporation and condensation of water are known to play an important role in concrete (*Baroghel-Bouny*, 2007; *Carlier and Burlion*, 2011; *Poyet*, 2013).

*This chapter is based on the article: Chaparro MC, Saaltink MW, Villar MV (2015), Characterization of concrete by calibrating thermo-hydraulic multiphase flow models, Transport in Porous Media, 109:147-167, DOI 10.1007/s11242-015-0506-9.

Therefore, it is necessary to measure thermo-hydraulic parameters, such as retention curve, thermal conductivity and diffusion coefficients, in order to predict the processes taking place inside the concrete and affecting its durability. Various methods for determining these parameters can be found in the literature. For instance, *Leech et al.* (2006) estimated retention curves from mercury intrusion and water sorption isotherms. *Baroghel-Bouny* (2007) studied the relation between the pore structure and the retention curve by using water vapour desorption-adsorption experiments. *Carlier and Burlion* (2011) carried out evaporation tests in concrete under isothermal conditions, so as to obtain its retention curve and relative permeability parameters improving the van Genuchten-Mualem's equations. *Brue et al.* (2012) estimated desorption isotherms experimentally at different temperatures, by using a model based on Kelvin-Laplace's capillary law. *Chen et al.* (2012) obtained water retention properties and a relative gas permeability curve in concrete by studying the effect of water saturation on gas relative permeability. *Poyet* (2013) used alternative mathematical functions to characterize the retention curve to obtain the intrinsic permeability of concrete, by means of experimental tests in concrete columns at isothermal conditions.

Most of these experiments consist of small samples and all of them were performed in isothermal conditions. In this work we analyse evaporation tests of 20 cm long concrete columns performed in non-isothermal conditions, monitoring the temperature and relative humidity outside and inside the concrete. Such experiments involve various interacting processes and require the simultaneous calibration of several parameters. Of course, this makes obtaining parameters more complex and difficult than for the experiments mentioned in the previous paragraph. Despite of this difficulty, for soils, methods have been reported for modelling evaporation tests and calibrating parameters to experimental data. *Pintado et al.* (2002) calibrated models of experimental tests in bentonite using an algorithm based in the least squares method. *Acero et al.* (2009) modelled evaporation tests at high temperatures of vadose tailings and *Gran et al.* (2011) modelled and calibrated a saline soil using mul-

tiphase models coupled to reactive transport. Although evaporation tests in concrete and their models have been reported (*Šelih et al.*, 1996), the method of calibration for obtaining thermo-hydraulic parameters has not been applied yet. We feel calibration of these tests can be useful for obtaining parameters for concrete too.

The objective of this work was to obtain thermo-hydraulic parameters of concrete by modelling evaporation tests in concrete columns in non-isothermal conditions. We used a low permeability concrete employed at a radioactive waste disposal facility in El Cabril (Spain). To do so we applied the following methodology:

- Two evaporation tests in concrete columns were carried out. One of them in room conditions and another one heated with a lamp. The relative humidity and temperature were motorized by sensors inside and above the columns.

- The drying retention curve of this concrete was estimated from relative humidity and gravimetric water content measured at the end of the tests.

- Simulations of the evaporation tests and the subsequent calibration by adjusting the model results to the experimental data have allowed finding the relative permeability, the tortuosity factor, the thermal conductivity and the boundary conditions parameters.

- These thermo-hydraulic multiphase flow models were used to better understand the processes inside concrete.

2.2 Experimental tests

2.2.1 Material

The concrete of the Radioactive Waste Disposal Facility at El Cabril (Spain) is a low permeability concrete with a water-cement ratio (w/c) of 0.44. The specimens of concrete used for the evaporation tests were manufactured at El Cabril, using the same receipt and procedures used to manufacture the concrete of the disposal cells. Its composition is shown in table 2.1 (*Villar et al.*, 2009; *Villar and Romero*, 2014).

Table 2.1: Concrete composition.

Component	Quantity
Aggregates (4/16)	1023 kg/m^3
Sand (0/4)	634 kg/m^3
Sand (0/2)	203 kg/m^3
Cement I-42.5 R/SR	400 kg/m^3
Melcret-222 additive	6.5 kg/m^3
Water	175 L/m^3

2.2.2 Hydraulic properties

Besides the evaporation tests, several other hydraulic tests were conducted (*Villar et al.*, 2009, 2012; *Villar and Romero*, 2014). The grain density of the concrete (mass of solid per volume of solid) was 2.68 g/cm^3, obtained by the picnometer method with water. The porosities calculated from this value are between 0.17 and 0.19. An intrinsic permeability of $4.2 \cdot 10^{-18}$ m^2 was calculated from hydraulic conductivity, which was measured using a

constant-head permeameter with water. Water retention curves were also determined experimentally by controlling relative humidity in desiccators (*Villar and Romero*, 2014), which are compared with the one obtained from the evaporation test (see section 2.3.3, Figure 2.2).

2.2.3 Evaporation tests

The evaporation tests were conducted in PVC moulds of 8.5 cm in diameter and 20 cm in height (*Villar et al.*, 2009). Five 0.8 cm diameter perforations had been previously drilled at different levels, and plastic dummy cylinders had been placed in them. The moulds were filled with liquid concrete. The columns were cured for two months at room temperature and then placed in a room with relative humidity between 70 and 100%, where the non-heated column remained for 11 months and the heated column for 25 months. Just before the evaporation tests, the cylinders were replaced by sensors (Figure 2.1). The temperature and relative humidity were monitored by Sensirion SHT75 sensors, whose error is approximately 2% but rises to approximately 4% when the relative humidity is close to 0% or 100% at 25 °C. Moreover, the error increases with temperature. A sixth sensor was placed above the column to measure the laboratory conditions. One test was performed in room conditions, while the other column was heated with a lamp, situated 35 cm above the column surface. The latter was wrapped in an insulating wool whose temperature was monitored by two additional sensors, one of them placed between the column and the wool and the other at the outside of the wool. Rather than insulating, its purpose was to quantify heat loss by the difference in temperature of both sensors and the thermal conductivity of the wool (0.032 W m^{-1} K^{-1}). In both cases evaporation took place only through the upper surface of the columns.The columns were placed on a scale to measure the loss of weight. The amount of evaporation can be calculated from this loss. After nearly one year the tests were dismantled when the upper part of the columns did not show important changes in relative

humidity. Then, they were cut in 5 horizontal sections and their water content was measured gravimetrically by oven drying at 110 °C.

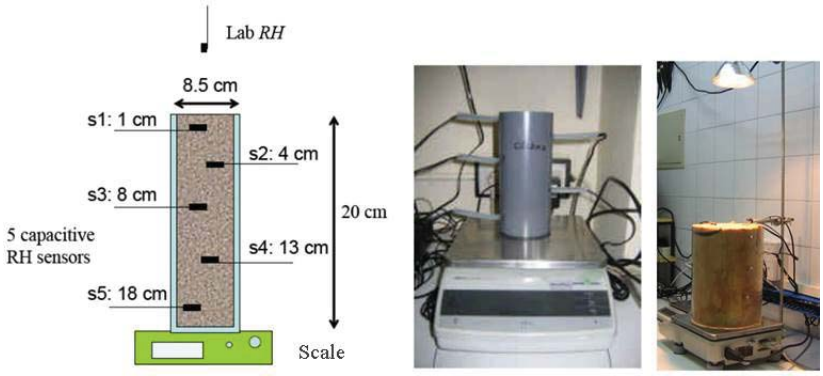

Figure 2.1: Set up for evaporation tests (*Villar et al.*, 2009); left: schematic cross section of the test; middle: non heated test; right: heated test.

2.3 Conceptual model and governing equations

2.3.1 Conceptual model

The evaporation tests were analysed by a comprehensive model that takes into account all relevant processes taking place. It considers the column as an unsaturated medium, composed of three phases: liquid, solid and gas. The solid phase has concrete as component. The liquid phase is composed of water, solutes and dissolved air. The gas phase is formed by a mixture of water vapour and dry air. Transport of vapour and heat was also considered through advection of the liquid and gas phases, diffusion and dispersion of vapour and heat convection. The gas pressure was not considered constant. In order to study the effect of the dissolved salts on vapour pressure and evaporation two models have been carried out for each test (heated and non-heated column): one model that did and another one that did not consider dissolved salts, leading to four models in total. The models with dissolved salts do

not take into account mineral precipitation. Hence, they overestimate the concentration of dissolved salts and its effect on evaporation. Therefore, these two assumptions can be seen as extreme cases between which reality is likely to occur.

2.3.2 Governing equations

The simulations were carried out with CODE_BRIGHT (*Olivella et al.*, 1996b), a finite element computer code that can handle multiphase flow, heat transfer and mass transport. It solves the balance equations for water (Eq. 2.1), air (Eq. 2.2), energy (Eq. 2.3) and/or salt (Eq. 2.4) (*Olivella et al.*, 1994).

$$\frac{\partial}{\partial t}\left(\theta_l \omega_l^w \rho_l + \theta_g \omega_g^w \rho_g\right) + \nabla \cdot \left(j_l^w + j_g^w\right) = f^w \tag{2.1}$$

$$\frac{\partial}{\partial t}\left(\theta_l \omega_l^a \rho_l + \theta_g \omega_g^a \rho_g\right) + \nabla \cdot \left(j_l^a + j_g^a\right) = f^a \tag{2.2}$$

$$\frac{\partial}{\partial t}\left(E_s \rho_s (1-\phi) + E_l \rho_l S_l \phi + E_g \rho_g S_g \phi\right) + \nabla \cdot \left(i_c + j_{Es} + j_{El} + j_{Eg}\right) = f^Q \tag{2.3}$$

$$\frac{\partial}{\partial t}\left(\theta_l \omega_l^h \rho_l\right) + \nabla \cdot j_l^h = f^h \tag{2.4}$$

Constitutive laws are used to express these balance equations as a function of the state variables liquid pressure, P_l, gas pressure, P_g, temperature, T and/or mass fraction of dissolved salt, ω_l^h. In this way we can account for all the relevant processes and properties, such as, relative humidity, retention curve, Darcy's law for an unsaturated medium, vapour

diffusion and heat conduction. Also properties such as surface tension, viscosity and density depend on temperature and/or salinity. Appendix A.2 gives a full list of all constitutive laws. For details on each equation we refer to *Olivella et al.* (1994).

2.3.3 Thermo-hydraulic parameters

The porosity and intrinsic permeability were taken from the experimental tests of *Villar et al.* (2009). We assumed the intrinsic permeability of the model to be constant and equal to the average of the values obtained from all experimental tests. Parameters which were not known or which were more sensitive to the model (relative permeability, tortuosity, thermal conductivity and boundary conditions parameters) were calibrated manually by fitting model results to data measured by the sensors.

The retention curve was obtained from the relative humidity measured by the sensors inside the columns at the end of the experiments and from the gravimetric water contents measured in the same positions after dismantling the columns. The results were fitted to the van Genuchten model (Appendix A.2, Eq.A.13; *Van Genuchten* 1980). An air entry pressure (P_0) of 7.7 MPa and shape parameter m of 0.34 were obtained (Figure 2.2). This high entry pressure reflects a very retentive material due to its small pores. We used the same air entry pressure (P_0) and shape parameter (m) for the heated and non heated column. Following *Wu et al.* (2014), our retention curve takes into account the effect of temperature and dissolved salts on the surface tension (Eq.A.13 and Eq.A.18). This simplifies the model reducing the number of parameters to calibrate. However, there is disagreement on the effect of temperature on the retention curve. For instance *Poyet* (2009) found an important effect of temperature, which was attributed to thermodynamic properties of the adsorbed water. The retention curve obtained by fitting the results of the evaporation tests is compared to the ones determined in desiccators measured by *Villar and Romero* (2014) (Figure 2.2). Re-

sults show that the latter never reach a saturation of 1. The most probable reason is that the samples had suffered drying during preparation. Before measuring the drying curve (i.e.,the retention curve from wet to dry) in the desiccators, the sample had to be re-saturated. However, this may entrap air in the pores giving a maximum saturation lower than 1. On the other hand, the evaporation test started after concrete had hardened without any previous drying, so it is assumed that the retention curve starts when the degree of saturation is 1.

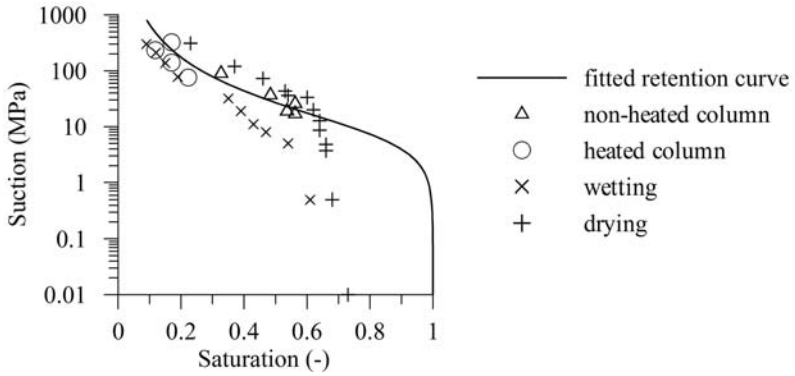

Figure 2.2: Fitted retention curve and measured data. The data from the non heated and heated column were measured at the end of each evaporation test. The wetting and drying data were obtained controlling the relative humidity in desiccators by *Villar and Romero* (2014).

2.3.4 Geometry and mesh

A one-dimensional domain of 20 cm length was assumed. The column was represented by a finite element mesh of 50 nodes and 49 elements with element sizes ranging from 2 cm at the bottom to 0.05 cm at the top.

2.3.5 Boundary conditions

Boundary conditions must be applied to take into account the exchange of vapour and heat between the column and its surroundings. For this, daily averaged temperature and relative

humidity were used, measured by the sensor situated above the columns (Figure 2.3). A summary of the parameters used in the boundary conditions is shown in Table 2.2. For vapour flux at the top of the columns a mixed boundary condition was applied (Eq. 2.5).

$$\begin{aligned} j_g^w &= \left(\omega_g^w\right)^0 \gamma_g \left(P_g^0 - P_g\right) + \beta_g \left[\left(\rho_g \omega_g^w\right)^0 - \left(\rho_g \omega_g^w\right)\right] \quad \text{if} \quad P_g^0 < P_g \\ j_g^w &= \left(\omega_g^w\right) \gamma_g \left(P_g^0 - P_g\right) + \beta_g \left[\left(\rho_g \omega_g^w\right)^0 - \left(\rho_g \omega_g^w\right)\right] \quad \text{if} \quad P_g^0 > P_g \end{aligned} \tag{2.5}$$

Where super index 0 refers to external values. The first term of the right hand side represents the advective vapour flux in gas flowing due to gas pressure difference between atmosphere and column. The parameter controlling this flow, γ_g, is high enough to nullify this gas pressure difference, so that it practically prescribes the gas pressure at the top of the column to the atmospheric pressure of 0.1 MPa. The second term of the right hand side represents a vapour flux due to the difference of vapour density ($\rho_g \omega_g^w$) between the atmosphere and the top of the column. Parameter β_g is a vapour exchange coefficient which depends on air movements and turbulent mixing between atmosphere and column. As it is difficult to assess a value to this parameter, it has been calibrated. For the air flux, similarly to the vapour flux, a mixed boundary condition was applied at the top of the column.

$$\begin{aligned} j_g^a &= \left(1 - \omega_g^w\right)^0 \gamma_g \left(P_g^0 - P_g\right) + \beta_g \left[\left(\rho_g \left(1 - \omega_g^w\right)\right)^0 - \left(\rho_g \left(1 - \omega_g^w\right)\right)\right] \\ &\qquad \text{if} \quad P_g^0 < P_g \\ j_g^a &= \left(1 - \omega_g^w\right) \gamma_g \left(P_g^0 - P_g\right) + \beta_g \left[\left(\rho_g \left(1 - \omega_g^w\right)\right)^0 - \left(\rho_g \left(1 - \omega_g^w\right)\right)\right] \\ &\qquad \text{if} \quad P_g^0 > P_g \end{aligned} \tag{2.6}$$

For the non-heated column no temperature gradient was observed by the sensors. Therefore, the temperature was prescribed in the entire column by means of a mixed boundary

condition for energy applied to the whole domain with a sufficiently high value for parameter γ_e (in the same way as γ_g). Note, however, that this prescribed temperature varies with time (Figure 2.3). For the heated column, another mixed boundary condition at the top of the column was applied in order to simulate energy flux (Eq. 2.7).

$$\begin{aligned} j_e &= j_e^0 + \gamma_e \left(T^0 - T\right) + E_g^w j_g^w \\ &\text{with} \quad \gamma_e = \rho_g^a c_a \beta_g \\ E_g^w &= E_g^w (T) \quad \text{if} \quad T > T^0 \\ E_g^w &= E_g^w \left(T^0\right) \quad \text{if} \quad T \leqslant T^0 \end{aligned} \tag{2.7}$$

In this case, γ_e was calculated from β_g assuming that energy and heat fluxes are controlled by the same turbulence mechanisms (*Arya*, 2001). For lateral heat exchange and that at the bottom the same mixed boundary condition was applied, but the parameter γ_e was calculated from thermal conductivity and thickness of the insulating wool and the radius of the column. No flow boundary conditions for salt and liquid were assumed ($j_l^w = 0$ and $j^h = 0$). External temperature T^0, vapour density, $(\rho_g \omega_g^w)^0$, and vapour mass fraction $(\omega_g^w)^0$ varies in time and were obtained from the sensor above the column (Figure 2.3).

2.3.6 Initial conditions

Initial conditions must be specified for each node and for all state variables (temperature, liquid pressure, gas pressure and (for the models considering dissolved salts) mass fraction of dissolved salt). Initial liquid pressure was calculated by the psychrometric law (Appendix A.2, Eq. A.7 and A.10) from initial values of temperature and relative humidity measured by sensors and then linearly interpolated. Initial gas pressure was assumed to be equal to an atmospheric pressure of 0.1 MPa. Also initial temperature was interpolated from initial

measured temperature. For the models considering dissolved salts (a sum of K, Na, Li, Ca, Sr, Ba, Cr, Mo, Fe, Al, Si, S and OH^-), an initial concentration was considered of 0.03 $kg_s kg_l^{-1}$ which was obtained from data from an ordinary Portland cement hardened after 317 days, published by *Lothenbach and Winnefeld* (2006).

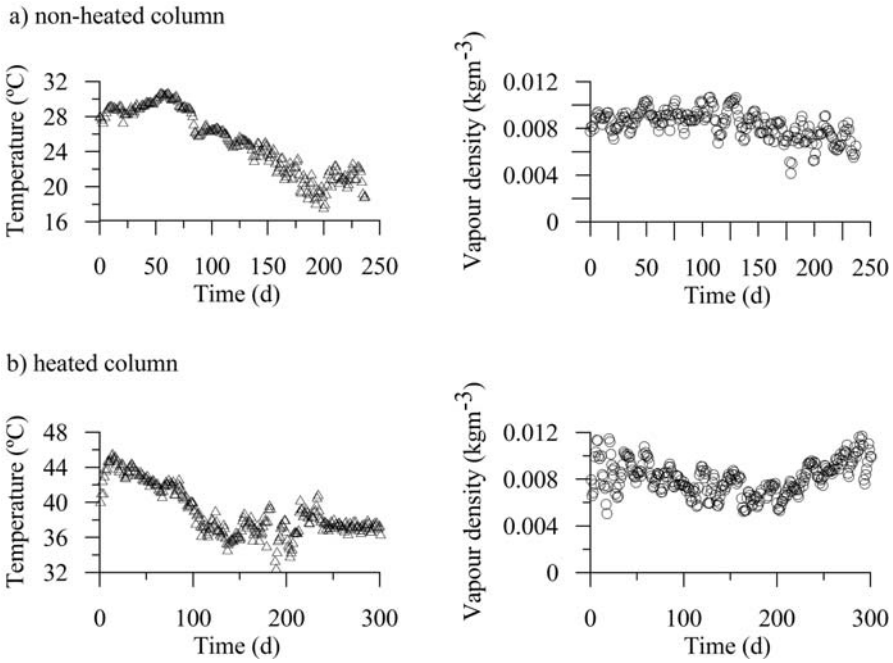

Figure 2.3: Boundary conditions. Evolution of temperature and vapour density in both experiments. Vapour density was calculated from temperature and relative humidity data measured by sensor situated above the columns (Eq. A.8, A.10 and A.20).

2.4 Results and discussion

2.4.1 Calibration

The parameters relative permeability (k_r, Eq. A.14 and A.15), tortuosity (τ, Eq. A.24), thermal conductivity (λ, Eq. A.30) and boundary exchange coefficient (β_g, Eq.2.5 and Table 2.2) were calibrated in order to fit the experimental data to the model results. The

Table 2.2: Parameters of the boundary conditions used in the models.

Position	column	
	non-heated	heated
top	$\beta_g = 10^{-3}\text{ms}^{-1}$	$\beta_g = 3.7 \cdot 10^{-2}\text{ms}^{-1}$
	$\gamma_g = 1$ kg s $^{-1}\text{m}^{-2}\text{MPa}^{-1}$	$\gamma_g = 0.5$ kg s $^{-1}\text{m}^{-2}\text{MPa}^{-1}$
	$(P_g)^0 = 0.1$ Mpa	$(P_g)^0 = 0.1$ Mpa
	$j_e^0 = 0$	$j_e^0 = 1100\text{J s}^{-1}\text{m}{-2}$
	$\gamma_e = 5$ J $\text{s}^{-1}\text{m}^{-2}$ $^\circ\text{C}^{-1}$	$\gamma_e = 41.61$ J $\text{s}^{-1}\text{m}^{-2}$ $^\circ\text{C}^{-1}$
lateral	$j_e^0 = 0$	$j_e^0 = 0$
	$\gamma_e = 5$ J $\text{s}^{-1}\text{m}^{-2}$ $^\circ\text{C}^{-1}$	$\gamma_e = 18.96$ J $\text{s}^{-1}\text{m}^{-2}$ $^\circ\text{C}^{-1}$
bottom	$j_e^0 = 0$	$j_e^0 = 0$
	$\gamma_e = 5$ J $\text{s}^{-1}\text{m}^{-2}$ $^\circ\text{C}^{-1}$	$\gamma_e = 0.64$ J $\text{s}^{-1}\text{m}^{-2}$ $^\circ\text{C}^{-1}$

calibration consists of changing these parameters and comparing the modelled results to the measured data by trial and error in order to obtain the best fit. Mathematically this could give rise to non-unique solutions, that is, various sets of parameters could give equally well fits. To avoid this, we required the parameters to be close to values from literature or the ones measured experimentally. This restriction allows us to find a unique set of values.

The relative permeability for both liquid and gas are functions of saturation through parameters A and n (Eq. A.14 and A.15). We also tried the van Genuchten-Mualem expression but the fitting was less satisfactory (not shown). Figure 2.4 shows liquid and gas relative permeability with the calibrated parameters. Theoretically A should have a value of 1 and for soils n normally has a value of 3. However, for liquid relative permeability we found values of 0.01 for A and 7 for n, which means that at saturation the relative permeability is not equal to 1. In comparison to granular media (soils and sand) the liquid relative permeability drops very fast with saturation. This behaviour in cement materials has also been

found in other studies (*Monlouis-Bonnaire et al.*, 2004; *Wardeh and Perrin*, 2006).

The tortuosity factor for vapour diffusion (Eq. A.24) had to be higher for the heated than for the non-heated column in order to achieve acceptable fits. This discrepancy reflects an often made observation that temperature gradients enhance vapour diffusion more than predicted by Fick's law of Eq. A.24. The mechanism may consist of the fact that at the pore scale vapour diffusion is linked to heat flux. Heat flux across a meniscus of water can transport vapour by condensing at one site and evaporating at the other side of the meniscus. This heat flux is larger than vapour diffusion. This phenomenon is call enhanced-vapour diffusion. *Ho and Webb* (1998) discuss this topic in more detail.

For the heated column, the dry and saturated thermal conductivity were calibrated. First, we used the experimental values measured by *Villar et al.* (2009) (λ between 2.2 and 3). However, using these values not enough gradient of temperature was simulated. So we reduce them in order to fit the model results to the experimental data of temperature. The values obtained (λ_{sat}=1.14 W m K^{-1} and λ_{dry}=0.66 W m K^{-1}, Eq. A.31) are low in comparison to those measured by *Villar et al.* (2009) but they are comparable with the ones reported by *Kim et al.* (2003). It is known that thermal conductivity is influenced by the type of aggregates, their volume fraction, temperature and porosity (*Marshall*, 1972; *Khan*, 2002; *Kim et al.*, 2003). The type of aggregates for the thermal conductivity experiments is probably different from the one used in the evaporation test. So do the volume fractions of these aggregates. Temperature is also different. The experimental thermal conductivity was measured at room conditions, while the evaporation test reach a temperature of 65°C. Moreover, despite of the same chemical composition of the cement, porosity could be slightly different for different samples maybe due to concrete manufacturing (for instance vibration process during manufacturing of the concrete sample).

For the non-heated column the calibrated value for the vapour exchange coefficient, β_g (Eq. 2.5 and Table 2.2) was high enough to practically fix the vapour density at the top of the

column. Hence this value has little physical meaning. For the heated column the calibration of vapour exchange coefficient β_g is linked to that of heat exchange coefficient, γ_e, (Eq. 2.7). The value obtained is similar to values found in other studies (*Pintado et al.*, 2002; *Gran et al.*, 2011).

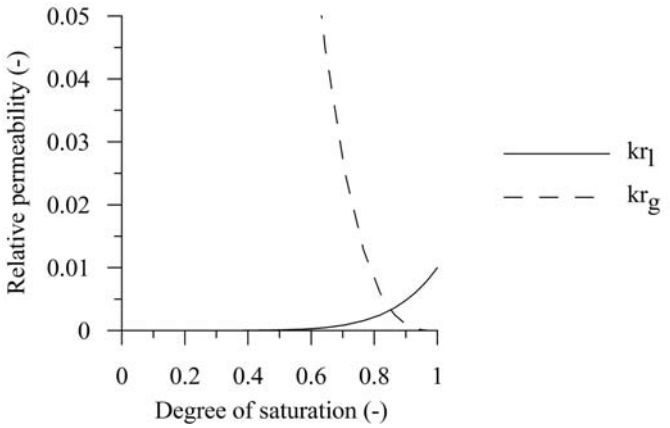

Figure 2.4: Relative permeability for liquid and gas phases.

2.4.2 Temperature

The temperature in the non-heated column is not particularly interesting. As explained in section 2.3, measured temperatures did not show any temperature gradient in the column and therefore we just fixed the temperature of the model to that measured by the sensor above the column (Figure 2.3a).

Figure 2.5 compares the evolution of temperature of the heated column measured by each sensor and calculated by the model without dissolved salts (the model with dissolved salts has practically the same calculated temperature, as it is not shown). There is a good agreement between the data and the model results. However, from day 189 the model overestimates the temperature. This could be because of the fact that the column was moved to another laboratory with more constant temperature. Moreover, the conditions in the two

laboratories (temperature and relative humidity) could lead to different values of boundary exchange coefficient (β_g and γ_e, Eq. 2.7 and Table 2.2). However, the models assume them to be constant. Note that there are only experimental data of sensor s5 at the beginning of the test. From the fifteenth day on, it stopped working because it was damaged.

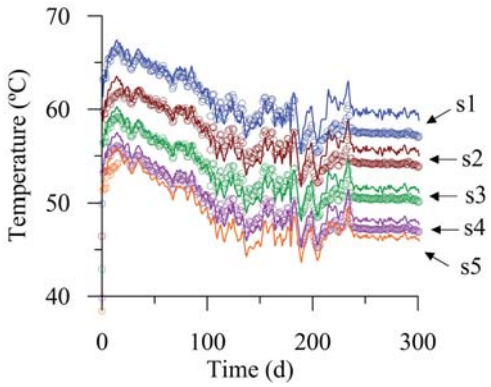

Figure 2.5: Evolution of temperature for each sensor in the heated column. Points are experimental data and continuous lines model results (no dissolved salts). The position of sensors is displayed in figure 2.1. After 189 days the column was moved to another room where temperature was more constant.

2.4.3 Concentration of dissolved salts

The concentration of dissolved salts, calculated for each column is displayed in Figure 2.6 (obviously, these results only correspond to the models which take into account the dissolved salts). In the non-heated column the dissolved salts do not have an important effect because the evaporation is low and, therefore, salt concentration does not increase much. However, in the heated column the concentration is higher due to the higher evaporation. The concentration is highest at the top of the column and this zone of maximum concentration extends downwards with time. This reflects a downward moving front where evaporation takes place and, as a result, concentration increases. Note that at the top of the column the final concentration of dissolved salts is slightly lower than at earlier times. This is due

to fluctuations in temperature and relative humidity and, hence, in evaporation rate.

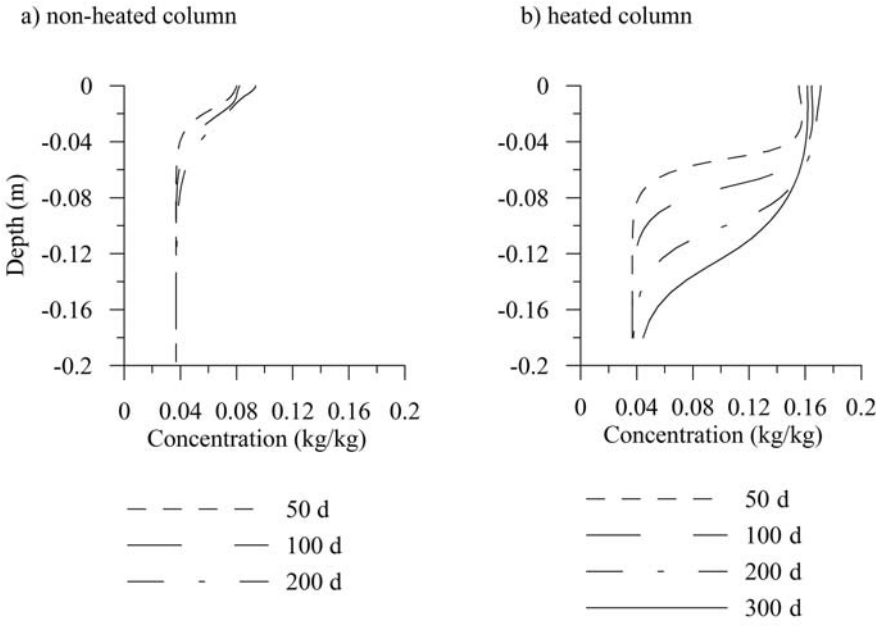

Figure 2.6: Dissolved salt concentration along the column at different times and for each test (0 is the top of the column).

2.4.4 Relative Humidity

Figure 2.7 compares the relative humidity (Eq. A.10) measured by the sensors to the results calculated by the models, for each column (non-heated and heated column) and each model (with and without dissolved salts). In the non-heated column, the model with dissolved salts and the model without have similar results. So dissolved salts do not seem to have an important effect on relative humidity, because only less than 20% of water initially present was evaporated. There is a good agreement between experimental data and the results of the model at sensor s2, s3 and s5. At sensor s1, situated at the top of the column, the model underestimates the relative humidity during the first half of the test and overestimates it during the second half. This could be related to some parameter which in reality may

depend on temperature but which the model assumes to be constant (see Figure 2.3a). The behaviour of sensor s4 is difficult to reproduce by the conceptual model used, because the relative humidity should be lower than sensor s5 according to its position in the column (see Figure 2.1). It is possible that this sensor was placed in an area in which the characteristics of concrete were slightly different, since due to the presence of coarse aggregates, the material is quite heterogeneous. As can be observed sensors s3, s4 and s5 have changes in the slope at the beginning of the test. This could be because the sensors are not perfectly sealed to the concrete. During the first 60 days the temperature rises (see figure 2.3a), which tends to decrease the relative humidity. In a porous medium this decrease is counteracted by evaporating water, retained in the pores. A small gap between concrete and sensor, however, may impede this counteracting.

The relative humidity in the heated column is displayed in Figure 2.7b. The model starts at the same initial relative humidity measured by the sensors. However, sensors s3, s4 and s5 measured an increase of the relative humidity from the first day, which hardly can be appreciated at the figure because of the scale used. This behaviour cannot be reproduced by the numerical model. Relative humidity should decrease because of evaporation. Probably it is due to measurement errors of the sensors. In this test the effect of dissolved salts gains importance because the evaporation is higher, around 40%. The difference between the models with and without dissolved salts is due to two effects. The first one is the fact that dissolved salts reduce evaporation and, as a consequence, increase the saturation. The second effect is the fact that with the same capillary pressure (and saturation) the relative humidity is lower because the salinity is higher (Eq. A.7 and A.10). At the upper part of the column (sensors s1 and s2), the relative humidity is lower for the model with dissolved salts than for the one without, because the second effect dominates. From mid column downwards (sensors s3, s4 and s5), the model with dissolved salts has a higher relative humidity, because the first effect dominates. However, the effect of dissolved salts seems

not to be very important.

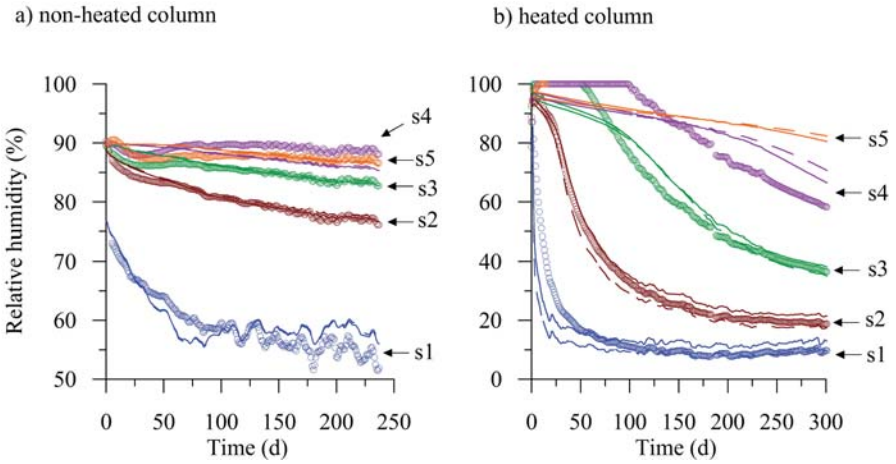

Figure 2.7: Evolution of relative humidity measured by each sensor for each column. The experimental data and results of the model with salinity and without it are compared. Points correspond to experimental data, continuous lines are model without dissolved salts results and broken lines are dissolved salts model results. The positions of each sensor are displayed in Figure 2.1

2.4.5 Loss of mass

The experimental and modelled evolution of loss of mass for each test is displayed in Figure 2.8. In the non-heated column, both models slightly overestimate the loss of mass during the first 170 days and slightly underestimate it afterwards. This error is related to the relative humidity observed for sensor s1. The relative humidity calculated by the model is lower at the beginning when evaporation is higher, and is higher at the end when there is less evaporation. In the heated column, from day 189 the experimental data show an increase in mass provably because the sample was moved to another laboratory with different conditions leading to different boundary exchange coefficients. In addition, the measurements could have lost precision due to this change. As this was not taken into account by the models, they show a continuous weight loss. As a consequence we obtained a worse

fit than for the heated column. In both columns, the loss of mass is higher for the model without dissolved salts than for the model with them. It means that, as expected, dissolved salts reduce the evaporation. However, in the non-heated column the differences between the two models are small. So the reduction of evaporation is higher when the evaporation is also higher.

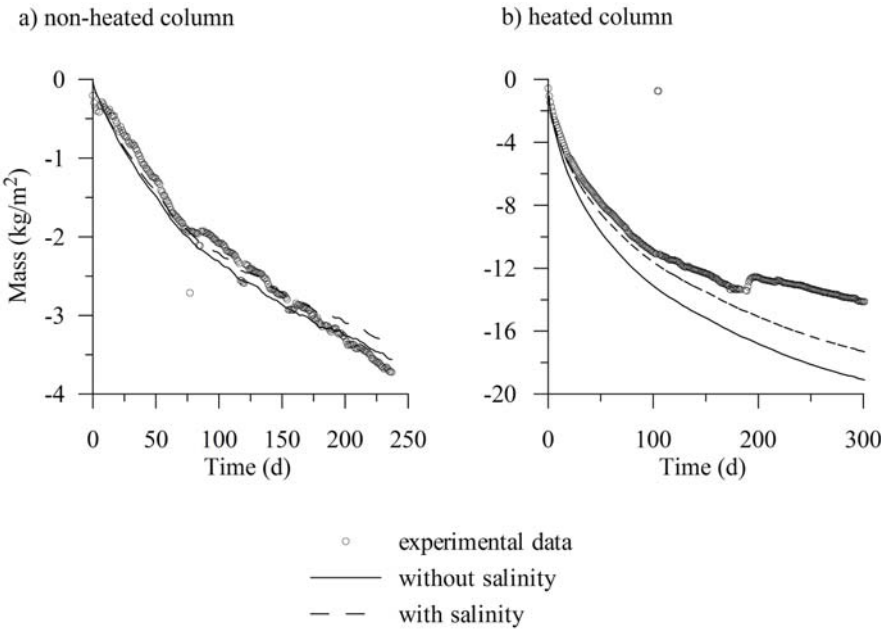

Figure 2.8: Loss of mass during evaporation test and concentration of dissolved salts effect. Both columns are displayed.

2.4.6 Saturation

The saturation at the end of the test is shown in figure 2.9 for each column. The saturation of experimental data was calculated from the gravimetric humidity in each section (Eq. A.3 and A.5). In the non-heated column there is no difference between the model with and without salinity. The saturation calculated numerically is lower at the top of the column and higher at the bottom and fits well to the measured data. For heated column, there are some

differences between the models from mid column downwards. The model with dissolved salts has higher saturation because salinity increases the saturation. The fitting for this column is not so good. In the numerical model the saturation increases with depth and the model overestimates the saturation. This error is related to the fact that our retention curve overestimates the saturation from mid column to downwards (figure 2.2). And the model underestimates the relative humidity (s4 and s5 figure 2.7).

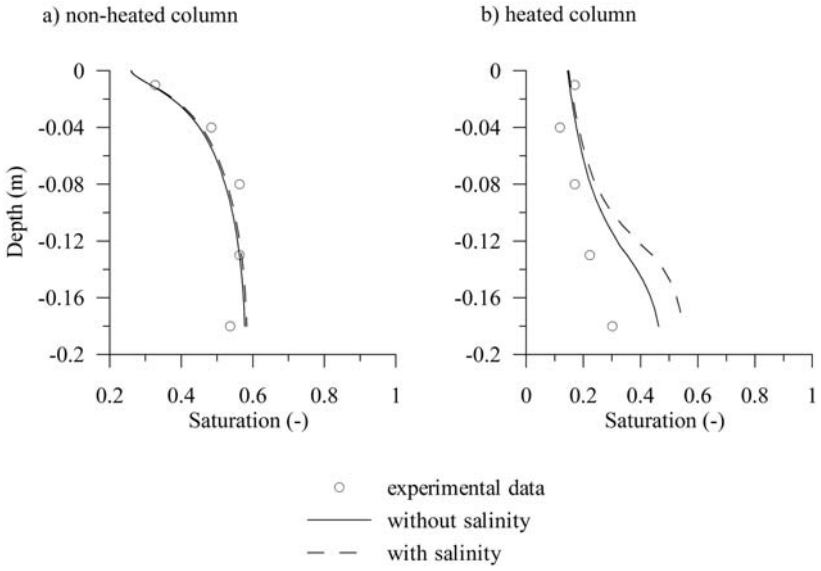

Figure 2.9: Saturation at the end of the test for each column (0 is the top of the column).

2.4.7 Flux

Figure 2.10 shows the evaporation rate for both tests. In both columns, there is a front where most evaporation takes place. In the non-heated column this front reduces with time and is near the top of the columns. In the heated column, however, the front moves downwards. There is a slight difference between the models with and without dissolved salts. In order to study the relative importance of the various processes, figure 2.11 displays advective fluxes of liquid and gas phases and diffusive flux of vapour along the column calculated by the

models at the end of the tests. For the non heated column, above the evaporation front vapour diffusion is the dominant water transport process, which has also been found in soils by *Grifoll et al.* (2005) and *Gran et al.* (2011). Below this front advection of liquid water is the dominant process. Although, gas advection appears negligible above the evaporation front, it has an important effect and the model had to include it in order to obtain an acceptable fit. This confirms the work of *Mainguy et al.* (2001) who studied the role of air pressure and advective vapour fluxes in the gas phase.

The heated column shows a higher vapour diffusion than the non-heated column. The energy from the lamp increases the evaporation and, therefore, lowers the liquid saturation, leading to a higher diffusion according to Fick's law (Eq. A.24). In addition, the lamp produces a gradient of temperature and, consequently, a gradient in vapour density. From mid column downwards of the heated column, salinity slightly reduces the vapour diffusion because the evaporation is lower and increases the liquid advection because the saturation increases (Figure 2.11b).

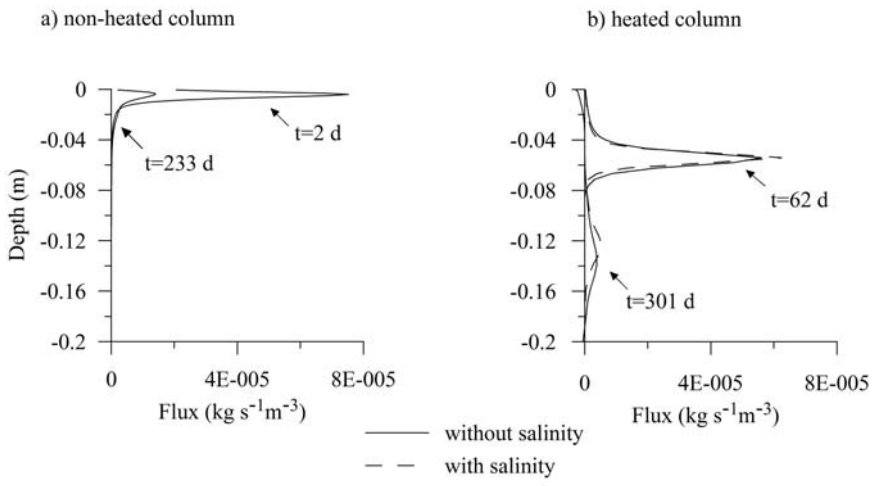

Figure 2.10: Evaporation rate along each column. Initial and final times are displayed.

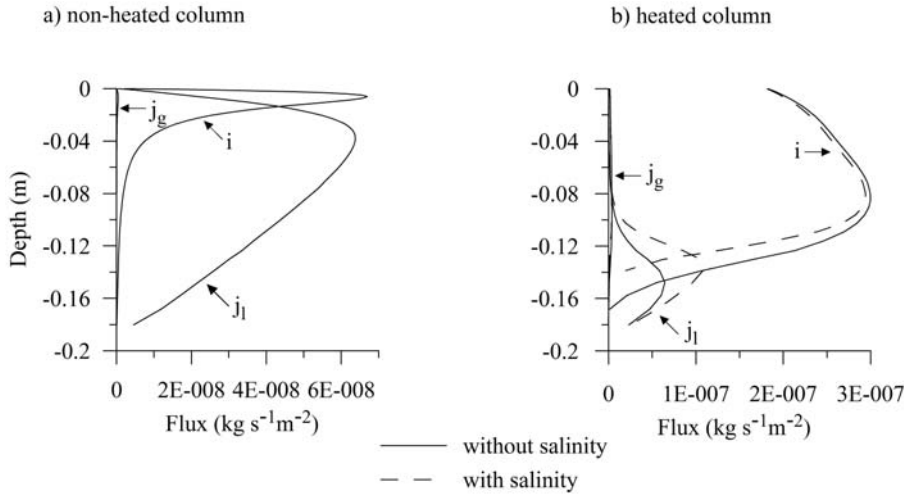

Figure 2.11: Advective flux of liquid (j_l) and gas (j_g) phase and diffusive flux (i) along each column at the end of the test.

2.5 Conclusions

Evaporation tests were performed in concrete columns, one column in room conditions and another one heated by a lamp. The calibration of models made it possible to obtain thermo-hydraulic parameters. We obtained the same values of most parameters for both the heated and the non-heated columns, which strengthens the validation of the calibrated parameter values. An exception was the tortuosity factor, which affects vapour diffusion. The difference in the estimated value of this parameter indicates enhanced vapour diffusion as discussed by *Ho and Webb* (1998). The retention curve obtained by fitting the results of the evaporation tests agrees with that determined by controlling the relative humidity in desiccators by *Villar and Romero* (2014), and shows that this concrete is a very retentive material reflected by the high entry pressure obtained. The liquid relative permeability drops considerably with saturation in comparison to granular media.

An advantage of the used method of calibrating models may be that it is not necessary to

wait several years for the system to reach a steady state, which is required for classical analyses of experiments for retention curves and relative permeabilities. This is particularly interesting for low permeability materials, such as this kind of concrete. We assume a homogeneous medium. Thus only the upper part of the column is needed to reach the steady state in order to calibrate the model.

The thermo-hydraulic multiphase flow models of these evaporation tests help to understand processes in concrete. According to our study the concentration of dissolved salts reduces evaporation to a maximum of 5%. This reduction gains importance when evaporation from the column is higher. However, it could be neglected. According to the calibrated model, in both columns, vapour diffusion is the dominant water transport above the evaporation front where water is mainly in gas phase and gas advection is negligible. Below this front advection of liquid water is the dominant process.

Chapter 3

Multiphase flow and heat transport in concrete cells for storing radioactive waste*

3.1 Introduction

It is known that concrete in constructions and buildings, exposed to variations of temperature and relative humidity can be damaged and its service life reduced by processes involving water flow, heat transport, evaporation and condensation. Several studies investigating these processes are reported. *Andrade et al.* (1999) studied experimentally the effects of daily and seasonal variations of external temperature and relative humidity on concrete columns. *Häupl et al.* (1997) studied the interaction of heat transfer, gas and humidity in materials used in construction by means of numerical models. *Lü* (2002) developed a nu-

*This chapter is based on the article: Chaparro MC and Saaltink MW, Water, vapour and heat transport in concrete cells for storing radioactive waste, in revision

merical model to predict the heat transfer and humidity in buildings, which has been tested experimentally. *Liu et al.* (2004) developed a method to solve condensation problems using numerical models and experimental data.

In soils evaporation is an important process. Hence, also an extensive amount of literature exists on the coupled transport of water vapour, liquid water and heat in this type of medium (e.g.; *Grifoll et al.* (2005); *Bittelli et al.* (2008); *Sakai et al.* (2009); *Banimahd and Zand-Parsa* (2013); *Gran-Esforzado* (2015)). In unsaturated porous media temperature gradients can cause diffusion of vapour with evaporation at the hot and condensation at the cold side. In theory, this process could saturate the cold side. However, to our knowledge a complete saturation due to temperature gradients has not been found in porous media, neither in concrete nor in soils.

This study was motivated by the transport of water and heat in the radioactive waste facility of 'El Cabril'. As it is explained in chapter 1, water is collected inside concrete cells storing the waste. This occurs in two periods of time (summer and winter). A sum of several factors contributes to the phenomenon taking place. The aquifer is approximately 3 m below the base of the cell and is hydraulically connected to the walls of the cell, allowing a capillary rise. The concrete used to build the cells has a low intrinsic permeability and high capacity of retention. So it contains water available for evaporation. A gap of air exists between the wall of the cell and the containers, causing a sufficient temperature difference for vapour diffusion to occur.

Several studies have been conducted to explain the phenomenon that takes place in 'El Cabril' using numerical models. First, a 1D model was developed to see whether the hypothesis of evaporation and condensation by temperature gradients could explain the observed water leaking from the drain (*Saaltink et al.*, 2005). Although it showed that this hypothesis was feasible, it could only be used for qualitative interpretations. Then, several

2D models were made improving the geometry of the cell, giving possible remediations to the problem and adding a multilayer cover (*Massana and Saaltink*, 2006; *Zuloaga et al.*, 2006; *Saaltink*, 2006; *Gamazo et al.*, 2007). Nevertheless, they did not take into account the real data of temperature and relative humidity measured in the cells. Moreover, they used thermo-hydraulic parameters from literature instead of parameters of the concrete to build the cells. Furthermore, results were also qualitative because they only considered the roof and one wall of the cell instead of simulating the temperature gradients in the whole cell.

The objective of this work is to study the processes that are taking place inside the cell by means of numerical models. To do so, we take into account the temperature and relative humidity measured by sensors placed inside and outside the cells. Also we used thermo-hydraulic parameters of the concrete used to build the cells. These parameters have been obtained from laboratory tests of the concrete (*Villar et al.*, 2009) and thermo-hydraulic multiphase flow models of evaporation experiments (Chapter 2). Moreover, we give some possible scenarios in order to remediable and avoid this problem.

3.2 Conceptual model

Figure 3.1 displays a scheme of a concrete cell where the radioactive waste is stored, and the conceptual model that explains why water is collected in the drain. 'El Cabril' has 28 cells, each one measures 19.3 m by 23.8 m by 9 m. The cells are filled with concrete containers, of 2.20 m by 2.25 m by 2.25 m. Each one contains the drums with the radioactive waste. The cells have 4 zones with containers, each zone has 80 containers. The 4 zones are separated with gravel. The wall of the cell and the containers do not fit perfectly. So between them a small gap of air exists. At the base of the containers there is porous concrete followed by a layer of baytec. Each cell has a drain at the center, which can be accessed through a

gallery. This gallery connects all the cells in the platform. The cell is partly buried (3 m) into the underlying rock. The rest of it is exposed to the atmosphere with its temperature oscillations. The temperature outside the cell oscillates between 40 °C in summer and 5 °C in winter. The water table is about 4 m below the base of the cell.

The conceptual model considers that water can ascend from the phreatic level to the wall of the cell due to capillary rise through the unsaturated rock. In summer, the wall of the cell is hotter and the wall of the container is colder because the air gap is acting as a thermal insulation. Thus, water can evaporate from the wall of the cell. Vapour diffuses through the air gap due to the gradient of temperature between the wall of the cell and the wall of the container. Water condensates at the wall of the container because it is colder. Consequently, condensed water runs off to the drain. In winter, the wall is colder and the container is hotter. Hence, water evaporates at the container and condenses at the wall. So, water again runs off to the drain. This only occurs in summer and winter because only then the temperature difference across the air gap is large enough to produce this phenomenon.

To understand and quantify these processes it is worth to remember some basic psychrometric properties and relations. The saturated vapour pressure as function of temperature can be expressed as:

$$P^{w}_{g,sat} = a \exp\left(\frac{-b}{T}\right) \tag{3.1}$$

Where T is the temperature in K, a and b have values of $1.36075 \cdot 10^{11}$ Pa and $5.2397 \cdot 10^{3}$ K, respectively (*Olivella et al.*, 1996a). Suction can be related to the saturated and actual vapour pressure through Kelvin's law.

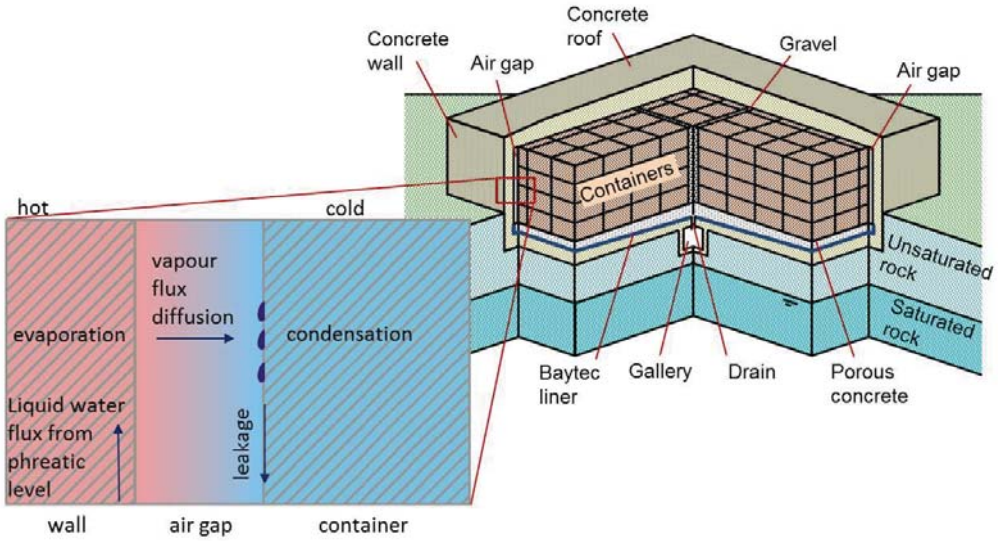

Figure 3.1: Scheme of a concrete cell and conceptual model. Situation in summer: water ascends from phreatic level, evaporates at hot side (wall of the cell), vapour diffuses through the air gap and water condensates at the cold side (wall of container).

$$RH = \frac{P_g^w}{P_{g,sat}^w} = \exp\left(\frac{-\psi M^w}{R\rho_l T}\right) \tag{3.2}$$

Where RH is relative humidity, P_g^w is the actual vapour pressure, ψ is the suction pressure ρ_l is the density of liquid water (1000 kg m^{-3}), R is the gas constant (8.314 J $mol^{-1}K^{-1}$) and M^w is the molecular weight of water (0.018 kg mol^{-1}). Vapour diffusion can be expressed by means of Fick's law.

$$i_g^w = \frac{-DM^w}{RT} \nabla P_g^w \tag{3.3}$$

Where i_g^w is the flux vapour diffusion (kg $m^{-2}s^{-1}$) and D is the diffusion coefficient (m^2s^{-1}).

Figure 3.2 shows the classical case of condensation in a cooling volume of air with

constant amount of water. Air with a temperature of 30 °C and relative humidity of 80% is cooled. As a result the relative humidity increases maintaining a constant vapour pressure, until it reaches a value of 100%. At this point (so called dew point) water starts to condensate and vapour pressure starts to drop.

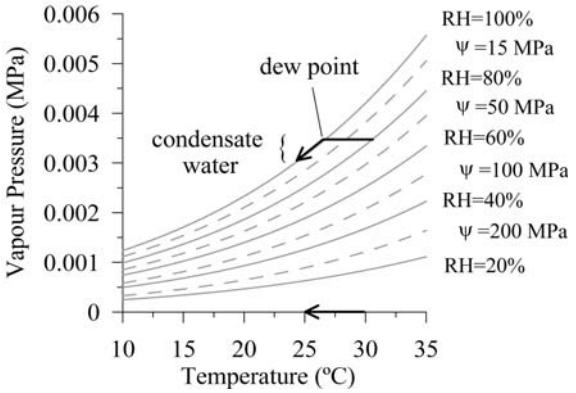

Figure 3.2: Psychrometric chart. Relation between temperature, vapour pressure, relative humidity and suction. When a temperature of an air decrease, their relative humidity decreases until it reach the dew point. From then on, if the temperature continues decreasing, water condenses.

When there is a temperature difference across an air gap, we can look at two extreme cases. The first case considers complete saturation at both ends of the gap ($P_g^w = P_{g,sat}^w$ and $\psi = 0$), that is, both ends are on the line of 100% relative humidity of figure 2. Given the temperature difference we can calculate the vapour diffusion by substituting Equation 3.2 into 3.3:

$$i_g^w = \frac{-DM^w}{RT} \nabla P_{g,sat}^w = \frac{-DM^w}{RT} \frac{dP_{g,sat}^w}{dT} \nabla T = \frac{-DM^w b P_{g,sat}^w}{RT^3} \nabla T \tag{3.4}$$

For a temperature of 293.15 K (20 °C) a diffusion coefficient of $10^{-5} m^2 s^{-1}$, an air gap of 0.02 m and a total gap surface of 800 m^2, this would lead to a total diffusive flux of 37 l d^{-1} for a one degree temperature difference. The second extreme case considers a situation

where the cold side is saturated whereas the hot side has dried up to a point where its vapour pressure equals that of the cold side and, consequently, no further diffusion takes place. That is, both sides are on a horizontal line in figure 3.2. Then we can calculate the suction at the hot side by substituting equation 3.1 into 3.2.

$$\psi = \frac{R\rho_l T}{M^w} ln\left(\frac{P^w_{g,sat}(T)}{P^w_{g,sat}(T_{dew})}\right) = \frac{R\rho_l b(T - T_{dew})}{M^w T_{dew}} \Rightarrow \frac{d\psi}{dT} = \frac{R\rho_l b}{M^w T_{dew}} \tag{3.5}$$

For a temperature at the cold side of 293.15 K (20 °C), a one degree temperature difference could dry the hot side up to a suction of 8.3 MPa.

3.3 Data from monitored cells

Two cells were monitored in order to measure the temperature and relative humidity: the first and the last closed cell. The first closed cell was the first cell where water was collected in the drain several years after it was closed. Sensors to measure temperature were installed at the walls, at the roof of this cell and another one at the drain. When water started to be collected from the first cell, sensors were installed inside another cell that was still open before it was closed. For the last closed cell, both, temperature and relative humidity were measured.

3.3.1 The first closed cell

The sensors to measure temperature are thermocouples which have a maximum error of ±0.5 °C. Figure 3.3 shows the evolution of the daily average temperature outside the cell for the roof and for each wall at 6 m and at 1 m from the base of the cell.

The temperature at the roof oscillates more than those at the walls at 6 m (Figure 3.3a). Temperatures at the western and southern walls oscillate more than those at the eastern and northern walls, because the last are in the shade of other adjacent cells. The maximum and minimum temperatures are approximately 37 °C and 5 °C, respectively (Figure 3.3a). At 1 m from the base of the cells sensors are below surface (Figure 3.3b). The sensor at the southern wall has larger oscillation of temperature because this part of the cell had been excavated to inspect potential infiltration through the junctions of the concrete. It is covered by plastic panes, which may create a greenhouse effect. Thus, sensor at the southern wall measure larger temperature oscillation, followed by west side, east side and north side of the cell. The maximum and minimum temperatures are 33 °C and 10 °C. As expected, temperature measured by the sensors at 6 m and the roof has larger oscillation than the one measured at 1 m because the last ones are below surface. Also a diver was installed in the drain in order to measure the temperature inside the cell (Figure 3.3b). This was the only place, where the interior could be monitored, because the cell was closed when water started to be collected. Temperature in the cell has little oscillation. It varies between 18.5 and 21.5 °C.

3.3.2 The last closed cell

Vaisala thermo-hygrometers were installed, that measure temperature and relative humidity of a wall of the cell, with a maximum error for temperature of ±0.5 °C and a maximum error for relative humidity of ±1.7%. Also thermocouples were used. However, as they measured practically the same temperatures as the thermo-hygrometers, they will not be further discussed. Figure 3.4 displays the position of the thermo-hygrometers and the evolution of temperature and relative humidity measured at the wall. One sensor is located at one side of the air gap, on the wall of the cell (HP_07), and another one at the other side of the air gap,

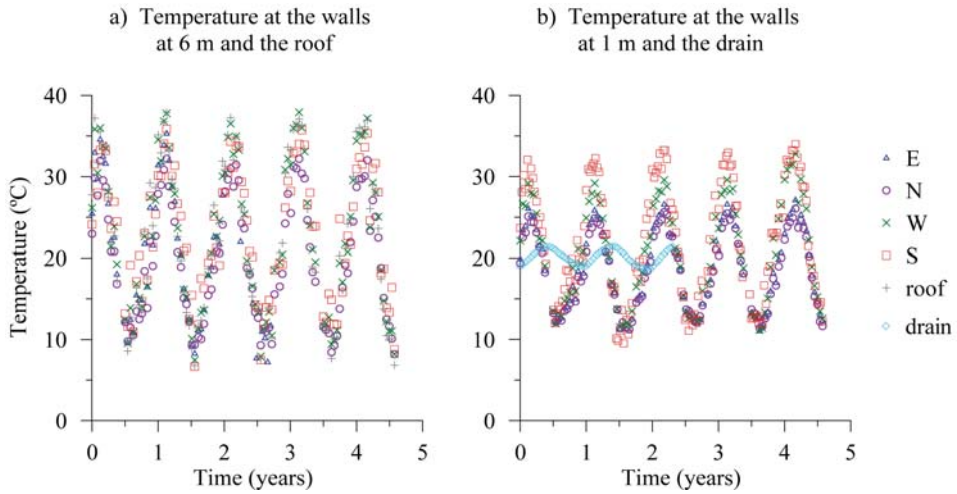

Figure 3.3: Evolution of the daily average of temperature outside the cell for the roof, in the drain and for each wall at 6 m and at 1 m from the base of the cell.

on the container (HP_12). Both are situated at 3.5 m from the base of the cell. Moreover, sensors have been installed at the interface between the containers and the gravel. One of them situated at 1.5 m and the others situated at 3.5 m from the base of the cell. Sensors situated at each side of the air gap (HP_07 and HP_12) measured a temperature difference of 2 °C. Sensors measured less temperature oscillation and more retardation, the further away from the wall of the cell (HC_11, HC_08). Sensors at the interior (HC_09, HC_10, HC_11 and HC_08) measured relative humidities that behaved oppositely to the sensors at the air gap (HP_07, HP_12). In winter, when the wall is close to saturation (RH $\approx$ 95%) sensors on the containers are dry (RH $\approx$ 60%). In summer the wall is dry (RH $\approx$ 60%) and sensors on the wall of the container are close to saturation (RH $\approx$ 95%). In general, relative humidity measured by the sensors never reaches 100%. Hence, theoretically water does not condensate enough to cause any leakage. We should be careful, however, when interpreting the relative humidity measured by the sensors at the air gap. The sensors are not located inside the concrete, but were placed on top of it. As the size of the sensors (about 1 cm) is only a bit smaller than the width of the air gap (about 2 cm), they measure the relative hu-

midity at some point in the middle of the air gap, which may be similar for the two sensors. Therefore, the measurements probably do not reflect the situation at the concrete of either the container or the wall. Nevertheless, we feel that temperature measurements by these sensors do reflect the container or the wall because of the large thermal conductivity of the sensors with respect to that of air. This is also demonstrated by the fact that these sensors measured temperatures practically identical to those measured by the thermocouples, which are much smaller.

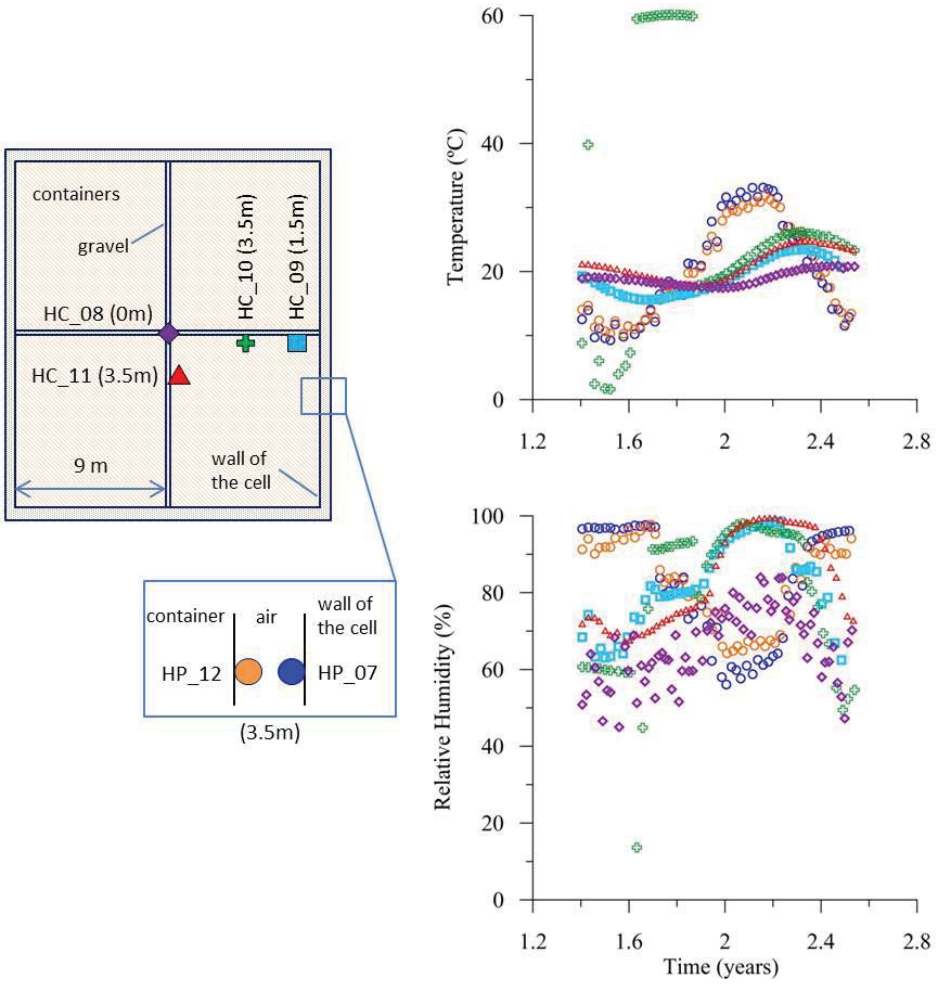

Figure 3.4: Position of the sensors and evolution of temperature and relative humidity inside the last closed cell.

3.4 Numerical model

We first developed a numerical model of the first closed cell, because here water is collected from the drain. We use the temperature measured by the sensors (outside the cell and at the drain), and the leakage rate of condensed water measured at the drain. Afterwards, using the same conceptual model we simulate the last closed cell, where no water is collected, but temperature and relative humidity inside the cell were measured.

3.4.1 Balance equations

These processes have been simulated using CODE_BRIGHT, a finite element computer code that can model multiphase flow and heat transfer (*Olivella et al.*, 1996b). This code solves the balance equations for water (Eq. 3.6), air (Eq. 3.7) and energy (Eq. 3.8). For more details on each equation we refer to *Olivella et al.* (1994).

$$\frac{\partial}{\partial t}\left(\theta_{\mathrm{l}}\omega_{\mathrm{l}}^{\mathrm{w}}\rho_{\mathrm{l}}+\theta_{\mathrm{g}}\omega_{\mathrm{g}}^{\mathrm{w}}\rho_{\mathrm{g}}\right)+\nabla\cdot\left(j_{\mathrm{l}}^{\mathrm{w}}+j_{\mathrm{g}}^{\mathrm{w}}\right)=f^{\mathrm{w}} \tag{3.6}$$

$$\frac{\partial}{\partial t}\left(\theta_{\mathrm{l}}\omega_{\mathrm{l}}^{\mathrm{a}}\rho_{\mathrm{l}}+\theta_{\mathrm{g}}\omega_{\mathrm{g}}^{\mathrm{a}}\rho_{\mathrm{g}}\right)+\nabla\cdot\left(j_{\mathrm{l}}^{\mathrm{a}}+j_{\mathrm{g}}^{\mathrm{a}}\right)=f^{a} \tag{3.7}$$

$$\frac{\partial}{\partial t}\left(E_{\mathrm{s}}\rho_{\mathrm{s}}(1-\phi)+E_{\mathrm{l}}\rho_{\mathrm{l}}S_{\mathrm{l}}\phi+E_{\mathrm{g}}\rho_{\mathrm{g}}S_{\mathrm{g}}\phi\right)+\nabla\cdot\left(i_{\mathrm{c}}+j_{\mathrm{Es}}+j_{\mathrm{El}}+j_{\mathrm{Eg}}\right)=f^{Q} \tag{3.8}$$

Subscript means phase (l=liquid, g=gas and s=solid) and superscript means component (w=water and a=dry air), θ is the volumetric content ($\theta = \phi S$), ω is the water or solute mass fraction in liquid or gas phase (kg kg^{-1}), ρ is the density (kg m^{-3}), ϕ is the porosity, j

is the mass flux of component in each phase (kg $s^{-1}m^{-2}$), E is the internal energy per unit of mass for each phase (J kg^{-1}), S is the water saturation and f is the external supply of a component.

Constitutive laws are used to express the parameters of the balance equations as a function of the state variables (liquid pressure, gas pressure and temperature). Thereby, we can take into account important processes and properties such as relative humidity (Eq. 3.2), Darcy's law for an unsaturated medium, vapour diffusion (Eq. 3.3) and heat conduction. Appendix A gives a full list of all constitutive laws used in this model and *Olivella et al.* (1994) gives the details on each equation.

3.4.2 Geometry, mesh and materials

Figure 3.5 displays the geometry of the numerical model, the mesh and the materials of which the cell is composed. We considered an axisimetric geometry, that is, the geometry of the numerical model is a cylinder, its volume being equal to the real cell. We made 4 axisimetric models, each one representing a quarter of the cell. The model distinguishes between six materials: the concrete of the walls, roof and base of the cell, the containers that store the waste, the air gap between the wall and the containers, the gravel that separates the four zones of containers, the porous concrete underlying the containers and the rock underlying the cell. The mesh consist of 6811 nodes and 6672 quadrilateral elements. It has been refined near the air gap where evaporation and condensation are expected to take place.

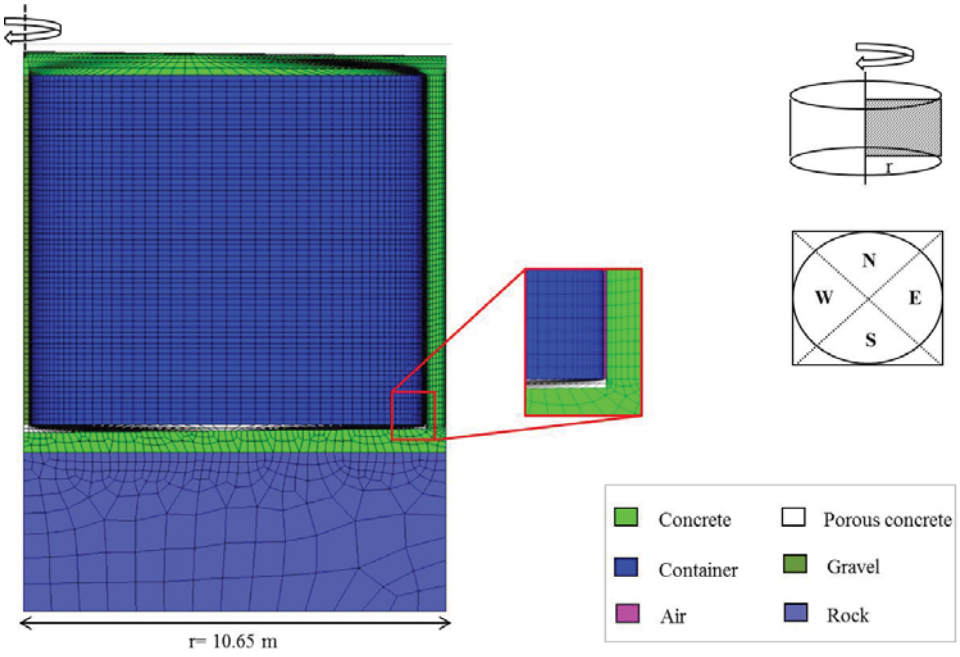

Figure 3.5: Geometry, mesh and materials of the numerical model

3.4.3 Thermo-hydraulic parameters

Some thermo-hydraulic parameters of the concrete (porosity and intrinsic permeability) used in our numerical model were obtained from experimental tests (*Villar et al.*, 2009) and from the calibration of thermo-hydraulic multiphase flow models of evaporation tests chapter 2. These parameters were used for the concrete of both the cells and the containers. Other parameters (retention curve, relative permeability and thermal conductivity) were calibrated. For the other materials (porous concrete, gravel and rock) we used the same parameters as *Massana and Saaltink* (2006). Table 3.1 summarises the parameters used in the numerical model. The further details of all the parameters definitions used in the numerical model are in Appendix A.

Porosity

The porosity of the concrete used to build the cells and containers is 0.17 (Chapter 2). The porous concrete has a higher value, 0.3. We used the same porosity for the gravel. The underlying rock has micro fractures filled with clay. So we used a value of 0.2 (*Massana and Saaltink*, 2006).

Intrinsic permeability

The intrinsic permeability of the concrete is 1×10^{-18} m^2 (Chapter 2). We used the same value for the cell and containers. For porous concrete, gravel and the rock we used a values of 1×10^{-10}, 1×10^{-11} and 1×10^{-15} m^2 respectively (*Massana and Saaltink*, 2006).

Retention curve

We used the van Genuchten model in order to simulate the retention curve:

$$S_e = \left(1 + \left(\frac{P_g - P_l}{P_0 \frac{\sigma_T}{\sigma_0}}\right)^{\frac{1}{1-m}}\right)^{-m} \tag{3.9}$$

where S_e is the effective water saturation, P_g and P_l are the gas and liquid pressure respectively (MPa), P_0 is the entry pressure (MPa), m is a shape parameter and σ_0 is the surface tension at 20°C (0.072 N/m) and σ_T is the surface tension at temperature T.

Calibration of the retention curve for concrete to measured leakage rates at the drain resulted in a P_0 of 3 MPa and a m of 0.34. Although the value of m is the same as that found in Chapter 2, the value of P_0 is different (7.7 versus 3 MPa). The difference is probably

due to hysteresis. In the previous Chapter is determined the retention curve in evaporation tests, where saturation always decreases, whereas in this case saturation increases as well as decreases. For porous concrete and gravel we used an entry pressure of 0.0003 MPa and a m of 0.9. The rock has a P_0 of 1 MPa and a m of 0.3 (*Massana and Saaltink*, 2006).

Relative Permeability

We used the van Genuchten model for the relative permeability as a function of saturation.

$$k_{\mathrm{rl}} = \sqrt{S_{\mathrm{e}}}\left(1 - \left(1 - S_{\mathrm{e}}^{1/\mathrm{m}}\right)^{\mathrm{m}}\right)^2 \tag{3.10}$$

where k_{rl} is the relative permeability of the liquid phase and m has the same value as the retention curve.

Thermal conductivity

The solid thermal conductivity (λ_{s}) of the concrete was calibrated. To do this, the model results were fitted to the measured temperature inside the drain. The thermal conductivity of the concrete cell and the concrete containers are different. This is because containers have metal drums inside and the thermal conductivity of metal is larger than that of concrete. The value calibrated is 1.56 W $\mathrm{m}^{-1}\mathrm{K}^{-1}$ for the concrete wall and 3 W $\mathrm{m}^{-1}\mathrm{K}^{-1}$ for the concrete containers. We used a value of 1.5 W $\mathrm{m}^{-1}\mathrm{K}^{-1}$ for the porous concrete and a value of 2.9 W $\mathrm{m}^{-1}\mathrm{K}^{-1}$ for the gravel and the rock (*Massana and Saaltink*, 2006).

Table 3.1: Thermo-hydraulic parameters used in the numerical model

	ϕ	k_i (m^2)	P_0 (MPa)	m	λ_s ($W\,m^{-1}K^{-1}$)
Concrete wall	0.17	1×10^{-18}	3	0.34	1.56
Concrete container	0.17	1×10^{-18}	3	0.34	3
Gravel	0.3	1×10^{-11}	0.0003	0.9	2.9
Porous concrete	0.3	1×10^{-10}	0.0003	0.9	1.5
Rock	0.2	1×10^{-15}	1	0.3	2.9

3.4.4 Initial and Boundary conditions

The initial conditions are different for the model of the first and last closed cell. For the first closed cell no data were available of the interior. We used an initial temperature of 19 °C, which was measured at the drain. For the initial liquid pressure we tried various configurations. Good fits could be obtained with an initial liquid pressure of -0.9 MPa within the cell with a linear increase to 0.1 MPa at the water table for the subjacent material. For the last closed cell data from the sensors inside this cell were used for initial temperature and liquid pressure. We consider a constant initial value of liquid pressure of -6.9 MPa for the wall, the roof and the concrete of the base of the cell, a value of -49.9 MPa for the container and -99.9 MPa for the gravel and porous concrete. The liquid pressure decreases linearly through the subjacent rock from a value of 0.1 MPa at the water table to -0.9 MPa at the base of the cell. The initial gas pressure is 0.1 MPa for all models.

Table 3.2 shows the boundary conditions that have been used. The temperature was fixed and varies with time at the wall and roof of the cell, using the daily average temperature measured by the sensors situated outside the cell (Figure 3.3). These temperatures were used for the model of both the first and last closed cell. The difference is that the first starts at the summer of 2007 when data became available and the last starts about a year later, when the

cell was closed. A leakage boundary condition was applied to the gap of air between the wall and the container allowing water to leave the cell only when liquid pressure exceeds atmospheric pressure. This represents the leakage to the drain. Finally, at the bottom of the model the water table was simulated by fixing the liquid pressure to 0.1 MPa.

Table 3.2: Boundary condition applied in the numerical model

	Water	Heat
Air gap	$q_\mathrm{l} = \gamma_\mathrm{l}\left(P_\mathrm{g} - P_\mathrm{l}\right)$ if $P_\mathrm{l} \geq P_\mathrm{g}$ $q_\mathrm{l} = 0$ if $P_\mathrm{l} < P_\mathrm{g}$	$j_\mathrm{E} = q_l E_\mathrm{l}(T)$
Wall/roof	$q_\mathrm{l} = 0$	$T = T_\mathrm{atm}(t)$
Water table	$P_\mathrm{l} = P_\mathrm{atm}$	$j_\mathrm{E} = q_\mathrm{l} E_\mathrm{l}(T)$ if $q_\mathrm{l} > 0$ $j_E = q_\mathrm{l} E_\mathrm{l}(T^\mathrm{ext})$ if $q_\mathrm{l} < 0$

Where q_l is the leakage rate of condensed water, γ_l is the boundary liquid exchange coefficient (kg $\mathrm{s}^{-1}\mathrm{m}^{-2}\mathrm{MPa}^{-1}$), T is the temperature (°C) and subscript atm means atmospheric and superscript ext means external.

3.5 Results and discussion

3.5.1 The first closed cell

Figure 3.6 displays the results obtained for the numerical model of the cell that was closed first. Figure 3.6a shows the evolution of temperature calculated by the model, taking into account the external temperature of the west wall (Figure 3.3). The others are similar (not shown). Two periods every year can be distinguished: summer where the temperature is around 30°C and winter where the temperature is around 10°C. The temperature of the wall has a larger amplitude than that of the container, which means that the wall is hotter than the container in summer and colder in winter, causing a temperature difference of

approximately 3°C. This gradient of temperature allows vapour to diffuse from the wall of the cell to the wall of containers through the air gap in summer, and the opposite in winter.

Temperature inside the cell is displayed at Figure 3.6b. The model results are the average of the temperature calculated by the 4 axisimetric models. Each model takes into account the external temperature of one wall of the cell. As shown, temperature at the drain oscillates between 19 and 22°C. The model reproduces this variation with the same amplitude but with some retardation with respect to the measurements. This retardation could be due to the simplicity of the geometry. We consider the cell as a cylinder in order to simplify the model, which could affect the results.

Figure 3.6c shows the relative humidity calculated by the model of the wall and the container, at both sides of the air gap at 3.5 m from the base of the cell. These results are from the model that takes into account the external temperature at the west wall. The others walls are similar (not shown). Two periods every year can be distinguished: summer and winter. In summer, the wall has lower relative humidity, around 90%, because evaporation is taking place, whereas the container reaches 100% because water condenses. The reverse occurs in winter, the container is dryer and the wall of the cell is saturated. According to equation 3.5 a temperature difference of 3°C gives a pressure suction of 25 MPa, which according to equation 3.2 corresponds to a relative humidity of 83%. The model reaches a minimum of only about 90%, which means that the extreme case of a completely dried up hot side is never reached.

Vapour pressure calculated by the model is shown in Figure 3.6d. Similarly to the relative humidity and temperature, summer and winter are distinguished. For both the wall and the containers vapour pressure is higher during summer than winter, because hot air can contain more vapour than cold air. The wall has slightly higher vapour pressure than the containers in summer and lower in winter. This small difference is the cause of evaporation

at the hot and condensation at the cold side. Notice, that although vapour pressure is similar for the wall and the container, relative humidity always differs significantly, which is due to the temperature difference across the air gap.

The leakage rate from the drain is displayed in Figure 3.6e. Model results are the average of the 4 axisymmetric models. Again the two periods (summer and winter) can be distinguished. Water from the water table enters the cell; the largest being in summer with a maximum of 5 l/d, because in summer the wall of the cell is dryer so the retention is higher, and larger amount of water can ascend from the water table. Condensed water leaves the cell also in two periods with large fluxes in winter (around 15 l/d) and small fluxes in summer (less than 5 l/d). Data are only available data for the two last years, which the model reproduces well. From equation 3.3 we can calculate a maximum that can condensate in a extreme situation. Considering complete saturation and a temperature difference of 3°C we obtain a leakage rate of 111 l/d. Obviously, in our case, we are far from this situation because lower values have been measured.

3.5.2 The last closed cell

First, we considered the same conceptual model as used for the the first closed cell. This could reproduce reasonably well the data measured by the sensors situated at both sides of the air gap (sensors HP_07 and HP_12 respectively). However, it could not reproduce the relative humidity measured by the sensors inside the cell (HC_09, HC_10, HC_11). We obtained a constant value of relative humidity of about 70% without any oscillation as measured by the sensor (Figure 3.4). We conjectured that inside the gravel convection is taking place due to the gradient of temperature. Hence, we made a 2D model of the N-S section of the cell, taking into account gas flow inside the gravel. Figure 3.8 shows the results of both models.

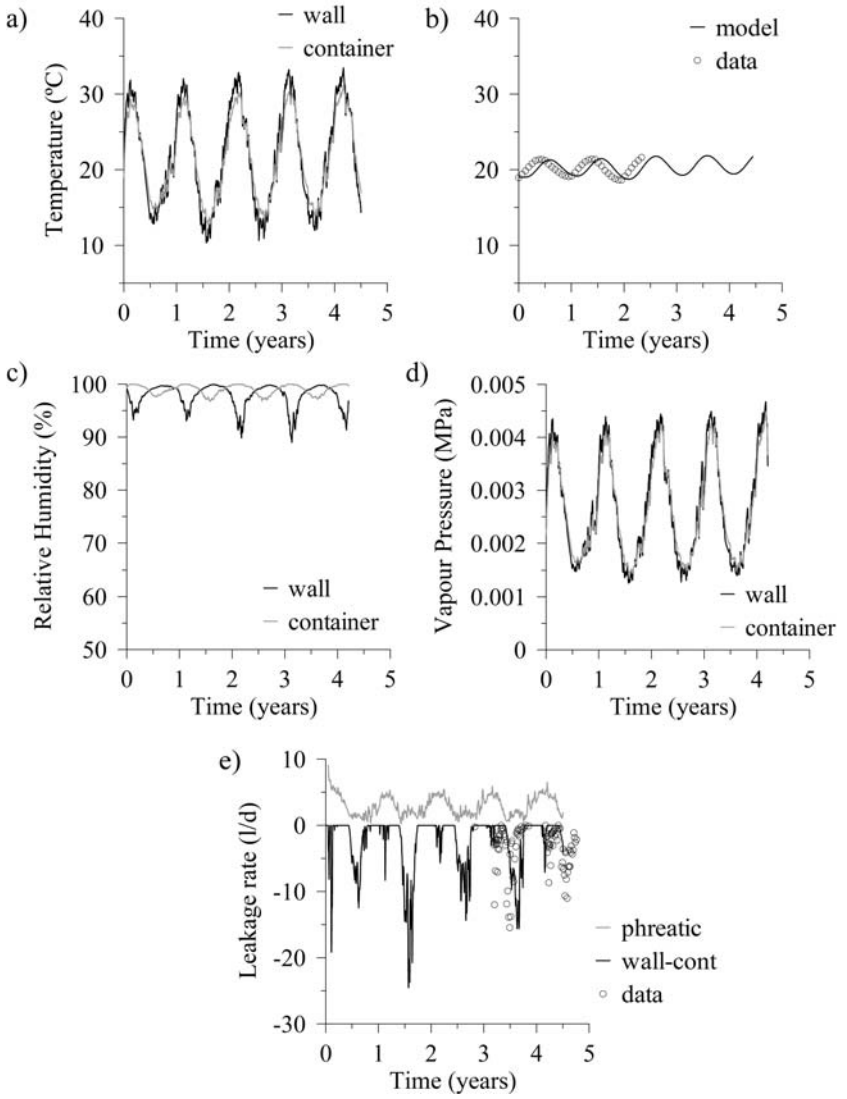

Figure 3.6: Results of the model of the first closed cell. a) Evolution of calculated temperature of wall and container. The black line means wall and grey line means container, both separated by the 2 cm of the air gap at 3.5 m from the base of the cell. b) Evolution of temperature inside the drain. Points are the measured data by the sensor located in the drain and the line is the temperature calculated by the model. c) Evolution of relative humidity calculated by the model. d) Evolution of vapour pressure calculated by the model. e) Leakage rate of condensed water calculated by the numerical model (lines) and compared with measured data (points). Positive values means that water comes in to the cell, and negative values means that water leaves the cell.

Axisymmetric model

The axisymmetric model attempts to predict the data from the sensors at the wall of the cell and at the container separated by the air gap (sensors HP_7 and HP_12, respectively). It uses the same conceptual model as used for the first closed cell, except for the initial conditions as explained in section 3.4.4. Figure 3.8a shows the results of the model together with the data measured by the sensors. The model roughly reproduces the temperatures measured by the sensor. Nevertheless, it overestimates the temperature difference between the wall and the containers. This could be due the boundary conditions, which use temperatures for the first closed cell, which may be somewhat different from that of the last closed cell. The model predicts a relative humidity similar to that of the first closed cell with high values at the containers and low values at the wall in summer and the reverse in winter. However, contrary to the first closed cell, the overall relative humidity is lower and never reaches 100% due to the drier initial conditions. Therefore, neither is there any leakage from the drain. Comparing the simulated with the measured relative humidity, we can see that the measured relative humidity shows much less difference between the wall and the containers, although both model and measurements show a higher relative humidity at the wall during winter and at the containers during summer. More importantly, during summer the measured values are much lower than the modelled results. This is also reflected by the vapour pressure, which is overestimated by the model during summer. These discrepancies can be explained partly by the size of the sensors discussed in section 3.3.2. However, it cannot explain the low relative humidity measured during the summer. We considered various scenarios to explain these measured values, such as, changing the initial values, the thermal conductivity, permeability and retention curve of the rock and concrete, but none of them resulted in better fits. A possible explanation could be that the sensors are located close to the gravel, which may be effected by convection processes, as will be discussed

in the next section. To simulate this properly a 3D model would be needed, which would require excessive number of nodes and CPU time.

Model with convection

A 2D model of the N-S section of the cell was made. This takes into account the walls of the cell (north and south) and the gravel inside the cell. Convection only takes place in the pores of the gravel, not in concrete, because the last is almost fully saturated and has low permeability. The convection causes the circulation of gas, heat and vapour due to the gradient of temperature between the top of the cell and its base, and also between the wall and the centre of cell. As this phenomenon only takes place in the gravel, we compare the results of the model with the measurements of the sensors that are attached at the containers next to the gravel (sensors HC_09, HC_10, HC_11). Figure 3.7 shows the modelled fluxes of gas in summer. As can be seen the hot wall and roof causes a circular flow with gas rising near the wall and descending at the centre of the cell. This flow pattern is reversed in winter.

Figure 3.8 compares the evolution of temperature, relative humidity and vapour pressure calculated by the model with the ones measured by sensors. Temperature calculated has some retardation and less oscillation than the one measured by the sensors (Figure 3.8b). The model reproduces the relative humidity measured by the sensor qualitatively. It overestimates the relative humidity in summer and underestimates it in winter. The vapour pressure calculated by the model also overestimates the relative humidity in summer and underestimates it in winter with less oscillation, as they are a function of relative humidity and temperature (Eq. 3.2). These discrepancies are probably due to the fact that the model is a vertical 2D cross section and does not consider the third dimension. A 3D model would be necessary in order to better simulate the processes that take place into the cell. However, again, it would require a larger number of nodes, and CPU times would become excessive.

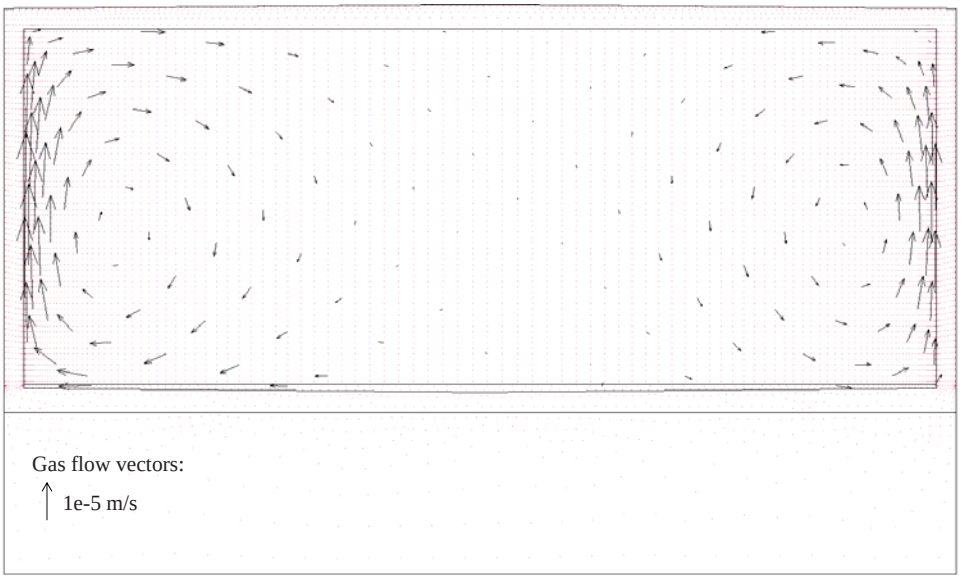

Figure 3.7: Geometry and results of the model with convection, situation in summer. Vectors of flux of gas show the convection cells

Nevertheless, the model shows that oscillations of vapour pressure and relative humidity can be increased, curiously, by enhancing mixing gas through convection.

3.6 Methods to avoid the phenomenon

We propose three scenarios to avoid or remediate the phenomenon that makes water leaving the cell. Figure 3.9 shows the evolution of temperature and flux for the three scenarios calculated by the numerical models. We simulated them with an axisimetric numerical model of the first closed cell during 10 years. We used the same boundary temperature condition from the first closed cell (Figure 3.3) for the first 4 years, which was repeated until the end (10 years).

The first scenario (Figure 3.9a) considers sand between the wall and the containers (instead of air). In this case the heat conduction gains importance, so that the difference

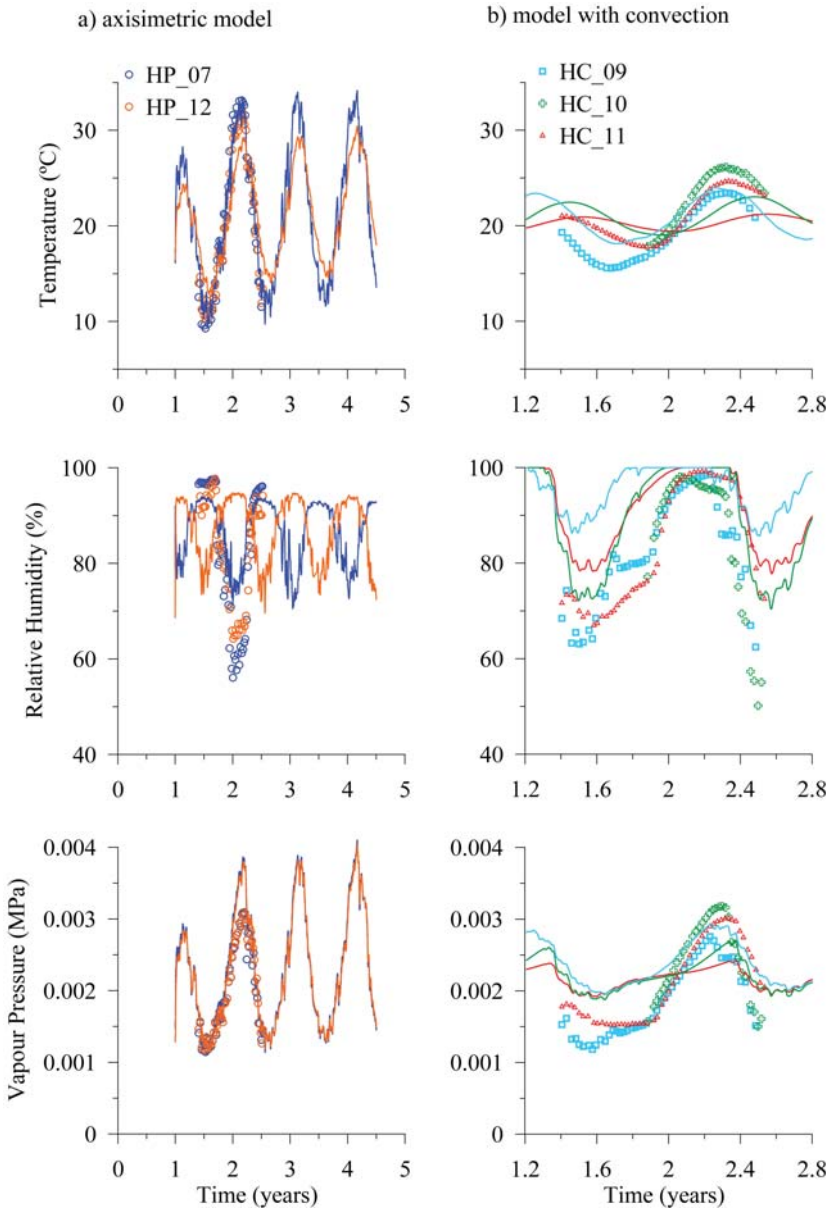

Figure 3.8: Evolution of temperature, relative humidity and vapour pressure calculated by the model taking into account convection (lines) and measured by the sensors (points)

of temperature between the wall and the containers is considerably reduced. The model shows seasonal oscillations of temperature from 30 to 10°C, but the temperature difference between the wall of the cell and the container is negligible. Consequently, there is no

leakage. However, water enters the cell at the phreatic level in summer (around 5 l/d), and leaves it in winter (around 1 l/d), thus, slowly saturating the cell. We feel that the risk of radioactive waste contaminating the groundwater is low, because the amount of incoming water is larger that the outgoing one.

The second case (Figure 3.9b) considers a cover on top of the cell. The cover can reduce the oscillation of temperature and the gradient of temperature between the wall of the cell and the container. To do so, the boundary condition of temperature was changed. We fix the temperature varying with time, on the wall and the roof of the cell, taking into account the thickness of the cover. Results show that the oscillation of temperature decreases considerably, to a maximum of 23°C and a minimum of 19°C. In this case, the difference of temperature between the wall of the cell and the wall of containers is very small, less than 0.5°C. Water does not leave the cell from the air gap between the wall of the cell and the containers. Water is always entering the cell at the water table, at a rate of 1 to 2 l/d. Probably this will continue until a hydrostatic situation is reached at the cell.

The third scenario (Figure 3.9c) considers a capillary barrier. It consist of 0.5 m of gravel, situated between the base of the cell and the underlying rock. The model shows seasonal oscillations of temperature, and also a gradient of 3°C between the wall of the cell and the containers. Water vapour can diffuse through the capillary barrier due to oscillation of temperature outside the cell, by means of the same mechanism as at the air gap (around 1 l/d). This means that water can still enter or leave the cell, although at rates lower than without capillary barrier (See figure 3.9d). Also water is still collected at the drain, but with lower rates. In the first two years 10 l/d of water is collected because of the initial condition. From then on, the rate drops to around 1 l/d with some peaks between 6 and 8 l/d.

The forth case (Figure 3.9d) not only considers a multilayer cover, but also a capillary barrier. Results show that temperature of the wall of the cell and the container is equal and

pretty much constant (around 21°C). Neither water is collected at the drain, nor water enters the cell at the phreatic level.

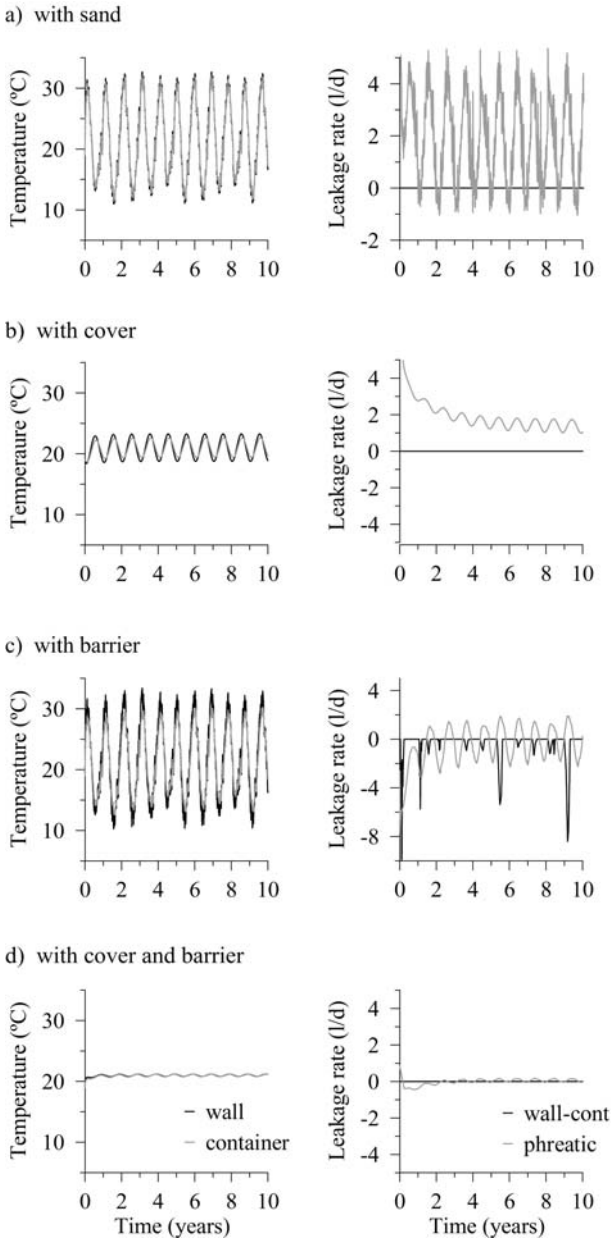

Figure 3.9: Evolution of the calculated temperature and leakage rate for the model with sand between the wall and container, with a cover, with a barrier and with a barrier and cover.

3.7 Conclusions

The model of the cell that was closed first confirms that water drains from the cells due to evaporation and condensation processes inside concrete:

- There is a gradient of temperature between the wall of the cell and the wall of the containers, which allows vapour diffusion through the air gap. The temperature inside the drain agrees with the one measured by the sensor.

- Relative humidity calculated by the model shows that in summer the wall is drier (due to evaporation) and the container is saturated (due to condensation). In winter it is the opposite.

- The model shows that water enters the cell at the phreatic level and leaves it at the drain. There is a good agreement between the modelled and measured leakage rates.

It must be said, though, that this model has only been calibrated by measurements at the drain in the centre of the cell. So, it may not be able to confirm more details on the processes. In the last closed cell sensors for temperature and relative humidity were installed, which permits the study of these processes at more detail. The model of this last closed cell, with the same assumptions as that of the first closed cell, shows some discrepancies with the measured data. Measured vapour pressure near the air gap are lower than those predicted by the model, this could indicate air instabilities due to temperature differences. Also the model cannot reproduce oscillations of relative humidity, measured inside the cell. However, a model that simulated flow of gas through the gravel shows that these oscillations can be caused by convection.

The numerical models suggest that the design of this kind of structures should take into account: temperature gradients, vapour diffusion inside the cells through air gaps, capillary rise from the phreatic level and possibly gas flow through air gaps and gravel.

The temperature gradients can be avoided filling the air gap with sand or they can be highly reduced with a cover. Using a cover and a capillary barrier the flux from the phreatic level could be considerably reduced. In all of these cases no water is collected at the drain. Using only a capillary barrier the rate of leakage to the drain is considerably reduced, but not eliminated.

Chapter 4

Modelling of Matrix Diffusion in a Tracer Test in Concrete*

4.1 Introduction

Concrete is a porous material that consists of cement paste and coarse and fine aggregates. The cement paste is composed of the hydration products of the cement, mainly CSH (calcium silicate hydrate), portlandite, ettringite and/or monosulfate together with smaller amounts of other hydration products. The way these phases are arranged geometrically can be quite complex. The microstructure of concrete around the aggregates is different from that of the bulk cement. In this so called interfacial transition zone the porosity can be higher (*Taylor*, 1997; *Scrivener et al.*, 2004).

Most studies consider diffusion as the main transport mechanism in cement based materials

*This chapter is based on the article: Chaparro MC, Saaltink MW, Soler JM, Slooten LJ, Mäder UK (2016), Modelling of matrix diffusion in a tracer test in concrete, Transport in Porous Media, 111:27-40, DOI 10.1007/s11242-015-0579-5.

and use tracer tests to study it. Traditionally, diffusion coefficients of different solutes are determined by means of diffusion cells, where the samples can only be a few mm thick because of the slow diffusion in this kind of material. For instance, *Goto and Roy* (1981) and *Atkinson and Nickerson* (1984) studied the effect of water/cement ratio, temperature, electric potential and/or curing time on the diffusion coefficient of Na^+, Cl^-, I^- and Cs^+ in cement pastes. The diffusion coefficients were obtained analytically. *Tits et al.* (2003) used numerical models to analyze their diffusion experiments with tritium and Na^+ and obtained the effective diffusion coefficient and the capacity factor of a high permeability cement. Although they used a single porosity model, they suggested the existence of a second type of porosity. Also, *Kamali-Bernard et al.* (2009) used numerical models for tritiated water diffusion tests in cementitious materials to investigate the changes in their microstructure due to mineral leaching. In recent years models have been proposed that take into account the heterogeneity caused by the complex structure of concrete. An example is the work of *Dridi* (2013), who made numerical models of tritium transport in cement pastes and concrete, explicitly simulating the geometry of the aggregates, interfacial transition zone and cement paste.

All these studies focused on diffusion, which makes sense in most cases, because concrete has a low permeability and water flow is often negligible. However, when concrete is exposed to evaporation, pressure gradient may become high and flow of water and, hence, advection and dispersion play a more important role. This is the case of the facility at ”El Cabril”. In this work we study solute transport in concrete taking into account diffusion, dispersion and advection. We treat the heterogeneity of concrete by means of matrix diffusion. Matrix diffusion has been applied to hydrogeological studies, particularly fractured aquifers (*Carrera et al.*, 1998; *Jakob et al.*, 2003; *Heer*, 2004). The goal of this work is to improve the understanding of processes and transport properties in concrete where advection is important. In particular, we studied the concrete from the radioactive waste disposal

facility at ”El Cabril”.

List of symbols

A_{matrix}	matrix area (m^2)
c	concentration (kg m^{-3})
c_{im}	concentration of species in the immobile zone (kg m^{-3})
c_{mo}	concentration of species in the mobile zone (kg m^{-3})
D_{im}	pore diffusion coefficient of species in the immobile zone (m^2s^{-1})
D_{mo}	combined dispersion-diffusion coefficient of species in the mobile zone (m^2s^{-1})
D_{disp}	dispersion coefficient (m^2s^{-1})
D_{diff}	pore diffusion coefficient (m^2s^{-1})
D_0	diffusion coefficient in the free liquid (m^2s^{-1})
F	exchange between the mobile and immobile zones
f_{matrix}	volumetric fraction of matrix (m^3m^{-3})
im	(subscript) immobile zone
mo	(subscript) mobile zone
n_{conc}	number of measured concentration
L_c	characteristic length (m)
q	darcy flux ($m^3m^{-2}s^{-1}$)
R	retardation factor
R_{im}	retardation factor of species in the immobile zone
R_{mo}	retardation factor of species in the mobile zone
t_c	characteristic time (s)
V_{matrix}	matrix volume (m^3)

V_p	pore volume (m^3)
$V_{p,im}$	pore volume of the immobile zone (m^3)
$V_{p,mo}$	pore volume of the mobile zone (m^3)
V_{total}	total volume (m^3)
$v_{cal,i}$	calibrated value
$v_{obs,i}$	observed value
x_D	dimensionless distance
α_L	longitudinal dispersivity (m)
σ_0	specific surface (m^2m^{-3})
σ_x	specific surface at depth x (m^2m^{-3})
τ	tortuosity factor
ϕ_{im}	porosity of the immobile zone
ϕ'_{im}	matrix porosity
ϕ_{mo}	porosity of the mobile zone
ϕ_t	total porosity

4.2 Experimental set up

4.2.1 Material

The concrete was manufactured by ENRESA (Spanish Nuclear Waste Management Company) following the same procedure as in the Radioactive Waste Disposal Facility at "El Cabril". It has a low intrinsic permeability, which is between 4.5×10^{-18} and 8×10^{-19} m^2, measured using a constant-head permeameter with water, and its w/c ratio was 0.44. The composition of the concrete is shown in table 4.1.

Table 4.1: Concrete composition. Values within parenthesis refer to minimum and maximum size (mm) of the aggregate or sand.

Component	Quantity
Aggregates (4/16)	1023 kg/m^3
Sand (0/4)	434 kg/m^3
Sand (0/2)	403 kg/m^3
Ordinary Portland Cement I-42.5 R/SR	400 kg/m^3
Rheobuild 1222 additive (superplasticizer)	6.5 kg/m^3
Water	175 L/m^3

4.2.2 Sample preparation

A cylindrical sample with a diameter of 5.5 cm and 10 cm in length was drilled from a cylindrical concrete block cured during approximately 6 months at room conditions. The sample was cut in three parts. The first one had a length of 5.5 cm and was used to perform the infiltration test. The second one was used to measure the water content using an oven at 105 °C and had a length of approximately 2.5 cm. The last one was not used.

The specimen used to perform the infiltration test was waterproofed in order to avoid infiltration of water through its lateral sides. Firstly, the lateral sides of the sample was covered with a layer of mortar to fill large pores. Then, a titanium filter, with a porosity of 0.28, and a titanium cylindrical piece were placed at both the bottom and the top of the sample. Finally, the setup was wrapped with several layers of Teflon, two layers of latex and several layers of insulating tape. Following this procedure, the core was ready to be introduced into the infiltration apparatus.

4.2.3 The infiltration test

We used a high-pressure core infiltration apparatus in order to perform the tracer tests in a reasonable time span. This device not only has been used to study tracer transport but also to investigate chemical rock-water interaction (*Adler et al.*, 2001; *Mäder et al.*, 2004, 2006; *Soler and Mäder*, 2007, 2010; *Dolder et al.*, 2013; *Jenni et al.*, 2013).

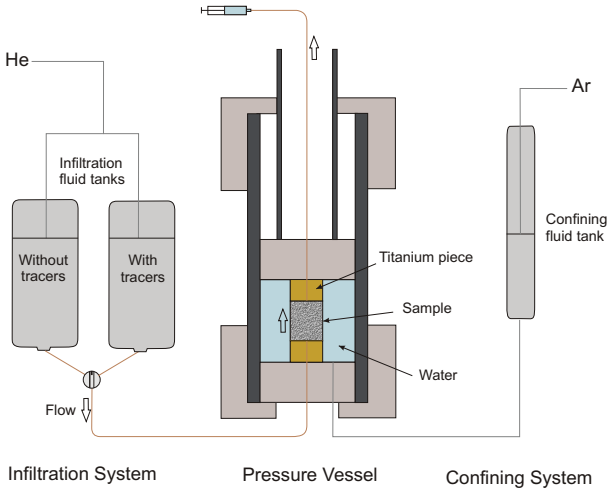

Figure 4.1: Scheme of the infiltration apparatus.

It was composed of three parts: the pressure vessel, the confining system and the infiltration system (Figure 4.1). The pressure vessel surrounds the core, containing the sample, confined with water of a pressure of 50 bars. This pressure was applied by connecting the pressure vessel to the confining system containing highly pressurized argon. The infiltration system consisted of pressurized helium (20 bars) connected to two tanks containing infiltration solutions, one with and one without tracers. Through a valve either one or the other solution could be injected into the sample. Both solutions consisted of distilled water with 10.6 g/l of KOH and 0.1 g/l of $Ca(OH)_2$, which gave a pH of 13.4. The tracer solution also had 155 mg/l of bromide and 576 mg/l of deuterium together in the same solution.

We performed the tracer test using a pulse injection. To do so, the solution without tracers was injected into the core during 4 days. Then, we switched to the tracer solution during 2 days. Finally, we injected again the solution without tracers during several weeks. The water leaving the outlet was collected by syringes. Afterwards, the solutions were analysed. Deuterium was analysed using Picarro L2130-i which is an isotopic water analyser for δD and δ^{18}O. Bromide and lithium were analysed using Ion Chromatography analysis with an 850 ProfIC An/Cat apparatus with MCS CO_2 Suppression from Metrohm.

4.3 Conceptual model

Following *Carrera et al.* (1998) our conceptual model is based on matrix diffusion, which is a transport mechanism that allows solute transfer between a mobile zone and an immobile zone. The mobile zone represents the well connected pores with solute transport by advection, dispersion and diffusion. The immobile zone represents the matrix, where solutes are transported only by diffusion. We compared three geometries of the porous medium so as to represent the immobile zone: slabs, spheres and tubes (Figure 4.2; *Carrera et al.* (1998)). A characteristic length, L_c, defines the size of the immobile zone for all geometries.

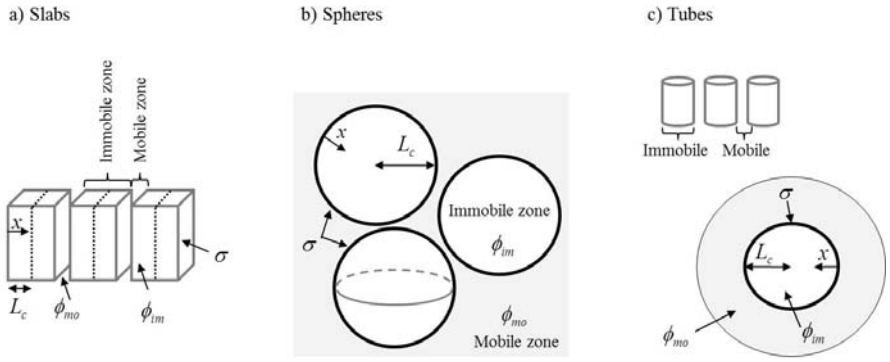

Figure 4.2: Geometries (immobile and mobile zones) for each conceptual model.

4.3.1 Parameters definitions

The conceptual model considers double porosity, which means that there is a porosity for the mobile zone, and another one for the immobile zone. The sum of the mobile and immobile porosities is the total porosity (Eq. 4.1, Eq. 4.2 and Eq. 4.3).

$$\phi_t = \frac{V_p}{V_{total}} = \phi_{mo} + \phi_{im} \tag{4.1}$$

$$\phi_{mo} = \frac{V_{p,mo}}{V_{total}} \tag{4.2}$$

$$\phi_{im} = \frac{V_{p,im}}{V_{total}} = \frac{V_{p,im}}{V_{matrix}} \frac{V_{matrix}}{V_{total}} = \phi'_{im} f_{matrix} \tag{4.3}$$

Subscripts *mo* and *im* refer to mobile and immobile respectively. ϕ_t is the total porosity, ϕ_{mo} is the porosity of the mobile zone, ϕ_{im} is the porosity of the immobile zone, ϕ'_{im} is the porosity of the matrix. V_{total} is the total volume (m^3), V_p is the pore volume (m^3), $V_{p,mo}$ and $V_{p,im}$ are the pore volume of the mobile and immobile zone respectively (m^3), V_{matrix} is the volume of the matrix (e.g. $A_{matrix}L_c$ for slabs, in m^3) and f_{matrix} is the volumetric fraction of the matrix (m^3m^{-3}).

A useful transport parameter is the characteristic time for diffusion in the immobile zone over a characteristic length . It can be formulated as:

$$t_c = \frac{L_c^2}{D_{im}} \tag{4.4}$$

t_c is the characteristic time (s), L_c is the characteristic length (m) and D_{im} is the diffusion coefficient of a species in the mobile zone ($m^2 s^{-1}$).

Another parameter is the specific surface, which is the interface area between the mobile and immobile zone divided by the total volume of the concrete sample. It depends on the geometry (Figure 4.2, Eq. 4.5, Eq. 4.6, Eq. 4.7 and Eq. 4.8).

$$\sigma_0 = \frac{A_{matrix}}{V_{matrix}} \frac{V_{matrix}}{V_{total}} \tag{4.5}$$

$$\text{Slabs:} \quad \sigma_0 = \frac{1}{L_c} f_{matrix} \tag{4.6}$$

$$\text{Spheres:} \quad \sigma_0 = \frac{3}{L_c} f_{matrix} \tag{4.7}$$

$$\text{Tubes:} \quad \sigma_0 = \frac{2}{L_c} f_{matrix} \tag{4.8}$$

σ_0 is the specific surface and A_{matrix} is the area of the matrix.

4.3.2 Mass balance equations

The numerical model solves the balance equations for the mobile and immobile zones (Eq. 4.9 and Eq. 4.10).

$$R_{mo}\phi_{mo}\frac{\partial c_{mo}}{\partial t} = \phi_{mo}D_{mo}\frac{\partial^2 c_{mo}}{\partial y^2} - q\frac{\partial c_{mo}}{\partial y} + F \quad \text{with} \quad R = 1 \quad \text{(no retardation)} \tag{4.9}$$

$$R_{im}\phi_{im}\sigma_x\frac{\partial c_{im}}{\partial t} = \phi_{im}\frac{\partial}{\partial x}\left(D_{im}\sigma_x\frac{\partial c_{im}}{\partial x}\right) \quad \text{with} \quad c_{im}\mid_{x=0} = c_{mo} \tag{4.10}$$

x refers to the direction in which matrix diffusion takes place (from mobile to immobile zones) and y refers to the direction where advection takes place in the mobile zone. The left hand term for both equations corresponds to storage. R is the retardation factor and it is defined as:

$$R = 1 + \frac{(1-\phi_{im})}{\phi_{im}}\rho_{solid}k_d \tag{4.11}$$

ρ_{solid} is the solid density and k_d is the distribution coefficient.

σ_x is the specific surface at distance x, defined as:

$$\text{Slabs:} \quad \sigma_x = \sigma_0 \tag{4.12}$$

$$\text{Spheres:} \quad \sigma_x = \sigma_0\frac{(L_c - x)^2}{L_c^2} \tag{4.13}$$

$$\text{Tubes:} \quad \sigma_x = \sigma_0\frac{L_c - x}{L_c} \tag{4.14}$$

The first term of the right hand side of Eq. 4.9 corresponds to the sum of diffusion and dispersion, where c_{mo} is the concentration of spices in the mobile zone (kg m^{-3}) and D_{mo} is the combined dispersion-diffusion coefficient of species in the immobile zone ($m^2 s^{-1}$). This is defined as:

$$D_{mo} = D_{disp} + D_{diff} \tag{4.15}$$

$$D_{disp} = \alpha_L q \tag{4.16}$$

$$D_{diff} = \tau D_0 \tag{4.17}$$

D_{disp} and D_{diff} are the dispersion coefficient and pore diffusion coefficient respectively ($m^2 s^{-1}$), α_L is the longitudinal dispersivity (m), q is the darcy flux ($m^3 m^{-2} s^{-1}$), τ is the tortuosity factor and D_0 is the diffusion coefficient in the free liquid ($m^2 s^{-1}$).

The right hand side of Eq. 4.10 refers to matrix diffusion, where c_{im} is the concentration of species in the immobile zone (kg m^{-3}), D_{im} is defined like in Eq. 4.17.

The third term of Eq. 4.9 corresponds to advection and the last one, F, is the exchange between the mobile and immobile zones which is defined as:

$$F = \sigma_0 \phi'_{im} D_{im} \frac{\partial c_{im}}{\partial x} \tag{4.18}$$

We can define a dimensionless distance, x_D, as:

$$x_D = \frac{x}{L_c} \tag{4.19}$$

and taking into account the definitions of specific surface (Eq. 4.6, Eq. 4.7 or Eq. 4.8) and the characteristic time (Eq. 4.4), we can rewrite the balance equation for the immobile zone (Eq. 4.10) as:

$$\text{Slabs:} \quad R_{im}\phi_{im}\frac{\partial c_{im}}{\partial t} = \phi_{im}\frac{1}{t_c}\frac{\partial^2 c_{im}}{\partial x_D^2} \tag{4.20}$$

$$\text{Spheres:} \quad R_{im}\phi_{im}\left(1-x_D\right)^2\frac{\partial c_{im}}{\partial t} = \phi_{im}\frac{1}{t_c}\frac{\partial}{\partial x_D}\left(1-x_D\right)^2\frac{\partial c_{im}}{\partial x_D} \tag{4.21}$$

$$\text{Tubes:} \quad R_{im}\phi_{im}\left(1-x_D\right)\frac{\partial c_{im}}{\partial t} = \phi_{im}\frac{1}{t_c}\frac{\partial}{\partial x_D}\left(1-x_D\right)\frac{\partial c_{im}}{\partial x_D} \tag{4.22}$$

By substituting the definitions of the specific surface (Eq. 4.6, Eq. 4.7 or Eq. 4.8), the immobile porosity (Eq. 4.3) and the characteristic time (Eq. 4.4) into Eq. 4.18, we obtain the following exchange term for each geometry:

$$\text{Slabs:} \quad F = \phi_{im}\frac{1}{t_c}\frac{\partial c_{im}}{\partial x_D} \tag{4.23}$$

$$\text{Spheres:} \quad F = 3\phi_{im}\frac{1}{t_c}\frac{\partial c_{im}}{\partial x_D} \tag{4.24}$$

$$\text{Tubes:} \quad F = 2\phi_{im}\frac{1}{t_c}\frac{\partial c_{im}}{\partial x_D} \tag{4.25}$$

Using a dimensionless distance our model can be described by means of 4 parameters: the immobile and mobile porosities, the characteristic time and the retardation factor.

4.4 Numerical model

The simulations were carried out with PROOST (Process Oriented Optimization and Simulation Tool; *Slooten et al.*, 2010), which is a general purpose hydrological modelling tool.

4.4.1 Geometry and mesh

A two-dimensional domain represented by a finite element mesh was used. We distinguished a mobile zone and an immobile zone. The mobile zone was represented by the y axis with 51 nodes and 50 one-dimensional elements. From each of these nodes there is a series of one-dimensional elements in the x axis representing the immobile zone. Each immobile zone was composed of 10 nodes and 10 one-dimensional elements with dimensionless lengths varying from 0.0025 to 0.3. Therefore, the whole mesh had 561 nodes and 560 elements.

4.4.2 Boundary conditions and initial conditions

A prescribed time-dependent mass flux boundary condition (qc) was applied at the inlet. Both flux (q) and concentration (c) vary in time (Figure 4.3). Initial concentration in the domain were zero for bromide and 4.346 mg/l for deuterium.

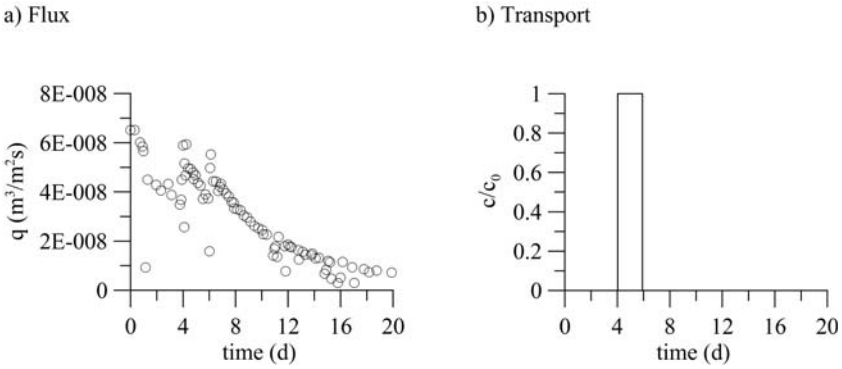

Figure 4.3: Boundary conditions. Evolution of flux and concentration.

4.4.3 Data and calibration

Prior to a calibration of the matrix diffusion model of section 4.3, we calibrated a single porosity model without matrix diffusion to see whether this simpler model was capable of reproducing the experimental data (Figure 4.4).

Calibration of the matrix diffusion models were performed by fitting the model to the measured breakthrough curves of bromide and deuterium. Some parameters were fixed in the model and some of them were calibrated. We used a porosity of 0.17 (Eq. 4.1), obtained from experimental data and numerical models (chapter 2) and calibrated a dispersivity of 0.001 m (Eq. 4.16) and pore diffusion coefficient of 5×10^{-10} m^2s^{-1} (D_{diff}, Eq. 4.17). These values gave good fits for the double porosity model. For deuterium we calibrated the porosity of the mobile zone (ϕ_{mo}; Eq. 4.2) and the characteristic time (t_c; Eq. 4.4). For bromide we first tried to calibrate the characteristic time, porosity of the mobile zone and the retardation coefficient of the immobile zone (R_{im}; Eq. 4.20, Eq. 4.21 or Eq. 4.22). The retardation coefficient of the mobile zone, (R_{mo}), was set to 1, because data show the same early arrival time for both tracers (Figure 4.4). However, the results showed that the porosity of the mobile zone and retardation coefficient were correlated, which means that only one of them can be estimated. Therefore, we fixed the porosity of the mobile zone at

a value equal to that obtained from the deuterium breakthrough curve. So, we calibrated the retardation coefficient for the immobile zone and the characteristic time. We use an automated calibration based on the minimization of the following objective function:

$$OF = \sum_{i=1}^{n_{conc}} (v_{obs,i} - v_{cal,i})^2 \tag{4.26}$$

v_{obs} and v_{calc} are the observed and calculated values respectively and n_{conc} is the number of measured concentrations.

The numerical method for this optimization was Marquardt's method (*Marquardt*, 1963).

4.5 Results and discussion

4.5.1 Experimental data

Lithium, bromide and deuterium were used as tracers. The breakthrough curves obtained for deuterium and bromide and the evolution of the cumulative mass (recovery) are displayed in Figure 4.4. Few data were obtained for lithium because the concentrations of the majority of the samples were under the detection limit of the Ion Chromatography analysis. Hence, the lithium concentrations were not used in the numerical models due to the lack of data. Note that the peak for bromide is lower than the one for deuterium. While the recovery for deuterium is 94%, the one for bromide is 67%. It seems that bromide suffers some form of retention which reduces its mobility.

4.5.2 Numerical model results

Figure 4.4 compares experimental data with the single porosity model. The breakthrough curves of bromide and deuterium and the cumulative mass are showed. The single porosity model cannot reproduce the measured data. It overestimates concentration at early time arrival and cannot reproduce the tailing at later times. Therefore, a double porosity model is necessary.

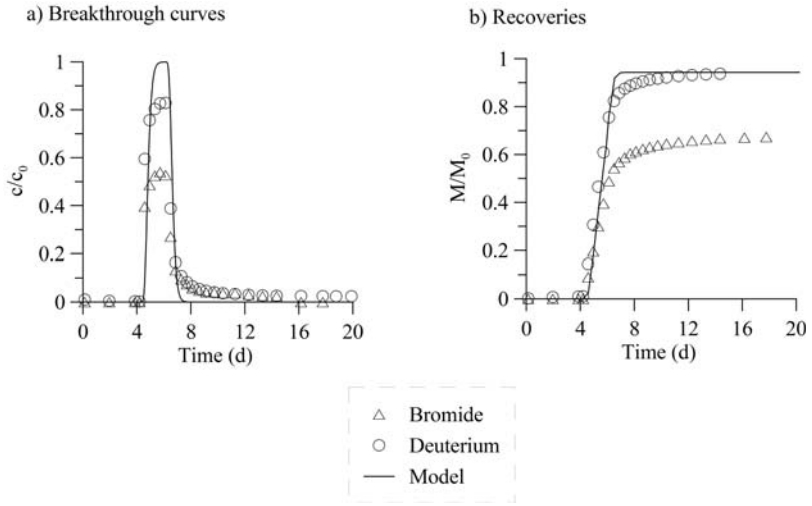

Figure 4.4: Evolution of relative concentration and cumulative mass for deuterium and bromide. Single porosity model results (lines) are compared with the experimental data (points).

Figure 4.5 compares best fits of the model taking into account matrix diffusion with the experimental data. The relative concentration, the log-log plot of the breakthrough curves and the cumulative mass with respect to time are displayed for each tracer (deuterium and bromide), and also for each geometry (slabs, spheres and tubes). Model results for deuterium fitted perfectly well the experimental data. Hence, the deuterium results show that the double porosity conceptual model can be applied in order to model conservative transport in concrete. Theoretically a $t^{-3/2}$ dependency on a log-log plot is an indication of

matrix diffusion (*Hadermann and Heer*, 1996; *Haggerty et al.*, 2000). Figure 4.5 do not clearly show such dependency. It would require longer time periods with a tailing covering several orders of magnitude. In our experiments, this would cause problems with respect to precision and detection limits of concentration measurements. To avoid this, larger concentration of tracers should have been added. Moreover, the flux of water in our test is not constant which also could have an effect on the shape of the breakthrough curve. Contrary to deuterium, the bromide data cannot be reproduced. Even when linear sorption is applied (Eq. 4.20, Eq. 4.21 or Eq. 4.22), the numerical model overestimates the recovered mass. Furthermore, slightly different results are obtained for each geometry. This suggests that some other processes or reactions are at work. It is difficult to determinate these processes from our results. However, some research has been published on anionic uptake in cementitious materials. *Baur and Johnson* (2003) found a strong sorption of selenate to monosulfate (AFm); they suggest a substitution of sulfate by selenate in monosulfate. Results obtained by *Bonhoure et al.* (2006), who also investigated the uptake of selenate, agreed with the previous finding. The iodide uptake by monosulfate was investigated by *Aimoz et al.* (2012); they found that the formation of AFm-I_2 could retard the mobility of ^{129}I. Hence, we suggest that similarly to selenate and iodide, the retardation of bromide could be due to uptake by monosulfate. Probably this cannot be described well enough by the linear retardation of our model. More research is needed in order to understand the retention of bromide.

For both tracers the breakthrough curves are similar for each geometry of the immobile zone (slabs, spheres and tubes). This means that we cannot deduce the geometry from concentration measurements at the outlet. However, the models reveal that concentrations in the immobile zone do depend on the type of geometry. This is illustrated in figure 4.6. It shows the relative concentrations of deuterium versus dimensionless distance (Eq. 4.19)

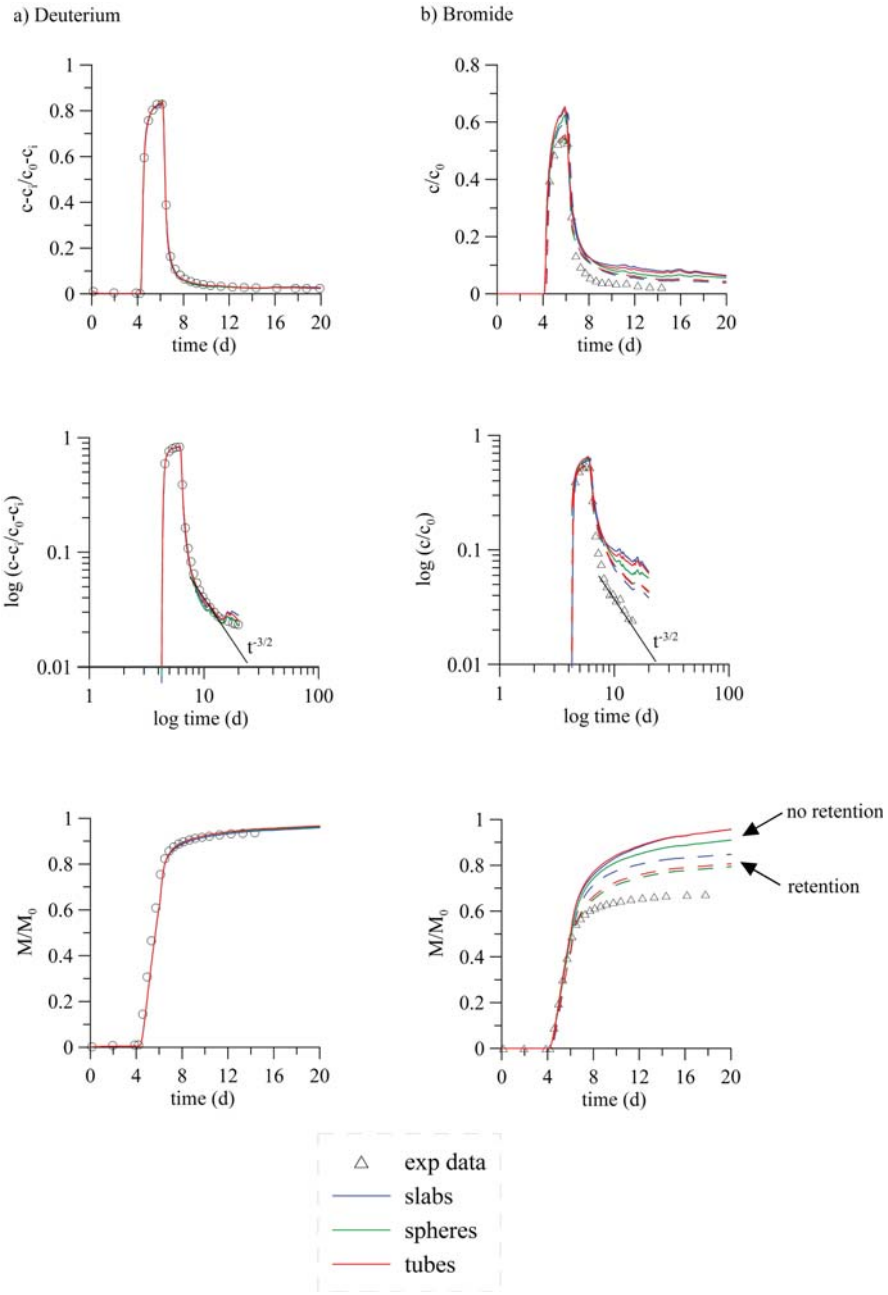

Figure 4.5: Evolution of relative concentration, log-log plot of the breakthrough curves and cumulative mass for deuterium and bromide. Double porosity model results (lines) are compared with the experimental data (points).

at the inlet of the sample (y=0 cm) for three different times (fourth, sixth and eighth day). For all geometries, just after the injection of the tracer (t=4 days) the relative concentration at the inlet is 1. Thereafter, the concentration of deuterium is moving towards the outlet of the sample and to the immobile zone (x axis), obtaining the maximum concentration in the breakthrough curve after 6 days. From then on, the concentration of deuterium in the immobile zone is higher than that in the mobile zone and deuterium diffuses back into the mobile zone, causing the tail in the breakthrough curve (Figure 4.5). Although the concentrations in the mobile zones are very similar in the three geometries, the slab geometry shows the deepest penetration of deuterium into the immobile zone. Spheres gives the shortest penetration.

The parameters obtained from the calibration of both tracers are shown in table 4.2. For deuterium the calibrated parameters were the mobile porosity (ϕ_{mo}; Eq. 4.2) and the characteristic time (t_c; Eq. 4.4). The immobile porosity was calculated from the total porosity and the mobile porosity (Eq. 4.1). The calibrated porosity of the mobile phase is similar for all the geometries. It is much smaller than the porosity of the immobile phase. There is less pore volume in the mobile zone, but the connection between pores is probably better than in the immobile zone. Values obtained for the characteristic time are different for each geometry due to the specific surface, which depends on the geometry (Figure Eq. 4.6, Eq. 4.7 or Eq. 4.8). Note that the spheres give a characteristic time about 8 times larger than that of slabs, while characteristic time for tubes is intermediate between spheres and slabs. This partly reflects the factors 1, 3 and 2 in Eq. 4.23, 4.24 and 4.25 respectively. Partly it reflects the deeper penetration into the immobile zone, hence lower concentration gradient ($\partial c_{im}/\partial x_D$) in the slabs (Figure 4.6). Large characteristic times were obtained for bromide because of retention. Similar values of retardation factor are calculated by the model. We cannot estimate a characteristic length independently of the diffusion coefficient of the im-

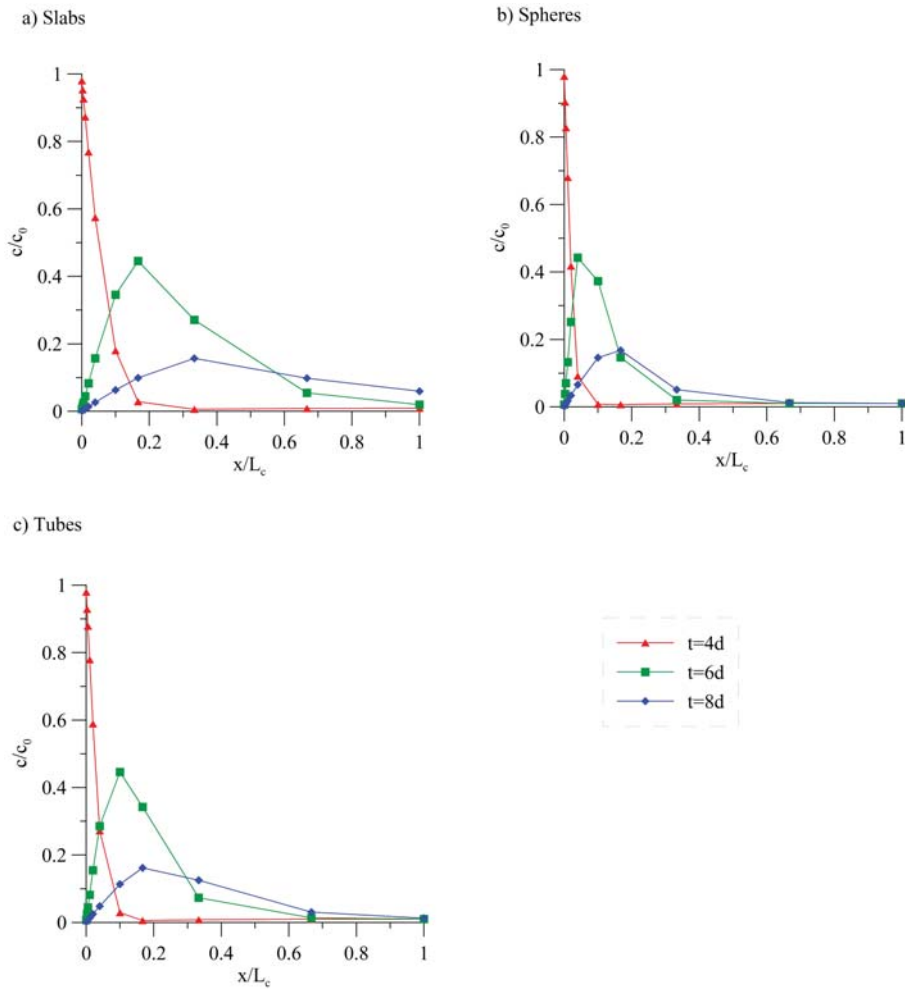

Figure 4.6: Relative concentration against dimensionless length (immobile zone) for all geometries in the deuterium model

mobile zone. However, considering a characteristic length of 100 μm (based on electron microscopy observations) we would obtain a pore diffusion coefficient between 2.8×10^{-15} and 3.6×10^{-16} m^2s^{-1}, depending on the geometry. These values are low compared to other diffusion coefficient measured in cementitious materials (*Goto and Roy* (1981); *Dridi* (2013); *Du et al.* (2014)). One explanation could be a higher characteristic length. An increase of the characteristic length by a factor of 10 would increase the diffusion coefficient with a factor of 100. Another explanation is that our pore diffusion coefficient only represents

small and poorly connected pores in the C-S-H gel that we assume constitutes the immobile zone, whereas the diffusion coefficients of *Goto and Roy* (1981); *Dridi* (2013); *Du et al.* (2014) represent the whole domain.

Table 4.2: Calibrated parameters by the numerical models.

Tracer	Geometry	ϕ_{mo}	ϕ_{im}	t_c (d)	R
Deuterium	Slabs	0.029±0.002	0.141	40.7± 6.0	
	Spheres	0.027±0.002	0.143	316.0± 58.6	
	Tubes	0.027±0.002	0.143	140.9± 23.3	
Bromide	Slabs			440.5±176.6	71.4±33.2
	Spheres			2232.9±477.2	73.4±28.9
	Tubes			1398.4±308.6	91.2±32.6

4.6 Conclusions

With the aim of improving the characterization of the transport properties of the concrete from the Radioactive Waste Disposal Facility at El Cabril (Spain), we performed a tracer test in a high-pressure core infiltration device using lithium, bromide and deuterium as tracers. We modelled the breakthrough curves of deuterium and bromide obtained from the experimental data. The conceptual model takes into account matrix diffusion, considering a mobile zone where advection, dispersion and diffusion are the transport mechanisms and an immobile zone where there is only diffusion. We assumed the immobile zone to consist of slabs, spheres or tubes. The models have been calibrated acquiring the mobile porosity and characteristic time. Analysing the results, we obtain the following conclusions:

- A single porosity model without matrix diffusion cannot reproduce the experimental

data.

- Excellent agreement between numerical model and experimental data for deuterium has been obtained. The double porosity conceptual model can be applied to model conservative transport in concrete.

- Bromide behaviour cannot be reproduced using a conservative transport model. Even when a retardation coefficient is applied the results are not satisfactory. Similarly to *Baur and Johnson* (2003), *Bonhoure et al.* (2006) or *Aimoz et al.* (2012), this could be caused by an uptake of bromide by the monosulfate phase.

- From the calibration of deuterium, similar porosities are obtained for all geometries. We found porosities of the immobile zone much higher than that of the mobile zone (about 0.14 and 0.028. respectively). However, the characteristic time depends on the geometry considered; the values obtained are between 40.7 and 316 days.

- For conservative tracers, such as deuterium, the fits for the three geometries were practically identical. This means that this type of tracer test cannot be used to determine the geometry of the immobile zone. To do so, a detailed structural characterization of the concrete should be performed. Theoretically, the geometry could also be deduced if tracer concentration distributions inside the immobile zone of the concrete could be measured. However, to our knowledge there is no experimental method for obtaining these types of measurements.

- Our findings suggest that double porosity models should be taken into account in models of transport in concrete, such as transport of radioactive contaminants in the concrete of the facility at ”El Cabril”.

Chapter 5

Reactive Transport Models of a High-pH Infiltration Test

5.1 Introduction

This work has been motivated by the previous chapter, where a tracer test in a concrete sample was carried out. In this experiment, hyperalkaline solution (K-Ca, pH 13.4) was injected into concrete. During the performance of the test the permeability decreased by a factor of 1000. This could be due to mineral precipitation. Hence, a reactive transport model has been carried out to study the changes in mineralogy that took place during the test.

In the literature works have been published on the hydration of cementitious materials (*Lothenbach and Winnefeld*, 2006; *Lothenbach et al.*, 2008), as well as on the geochemical interaction of the cement pore water with granite or clay materials (*Pfingsten et al.*, 2006; *De Windt et al.*, 2008; *Kosakowski and Berner*, 2013; *Soler*, 2013, 2016). However, few works have studied infiltration tests in concrete. One of them is the work of *Chapwanya*

et al. (2009), who modelled re-wetting experiments in concrete. They consist at placing dry concrete samples in a liquid bath and observing the progress of the wetting front. Both water and isopropanol were used as infiltration solutions. Reactions were produced when water was used as infiltration solution. Residual alite and belite dissolved,and as a consequence C-S-H gel precipitated reducing porosity. Reactive transport models in hardened cement were also reported by *Soler et al.* (2011) and *Soler* (2012). They studied the changes in mineralogy and porosity produced by the interaction between water and a cementitious grout by means of numerical models.

None of them applied reactive transport in a double porosity model under advective flow through the concrete. The objective of this work is to study the reactive transport in concrete taking into account the matrix diffusion conceptual model explained in the previous chapter.

5.2 Materials and Methods

In this work we used the same experiment as the previous chapter (Chapter 4). Hence the concrete samples and their composition are described in Section 4.2. Table 5.1 gives the composition of the cement used for preparing the concrete. It is the same cement used in the Radioactive Waste Disposal Facility at ”El Cabril” (Spain).

In short, the test consisted of injecting a high pH solution (pH=13.4) with tracers (lithium, bromide and deuterium) into the sample using a pulse injection. Afterwards, the same solution but without tracers was injected until the end of the test. A device that allows injecting the solution with a high infiltration pressure was used (Section 4.2.3). The infiltration solutions were composed of distilled water with 10.6 g/l of KOH and 0.1 g/l of $Ca(OH)_2$ giving a pH of 13.4. The outlet solution was collected by syringes. These samples were analysed using ion chromatography analysis with an 850 ProfIC An/Cat apparatus

Table 5.1: Cement composition (Ordinary Portland Cement I-42.5 R/SR).

Component	Quantity (kg/kg)
SiO_2	19.2×10^{-2}
Al_2O_3	1.2×10^{-2}
Fe_2O_3	4.5×10^{-2}
CaO	66.1×10^{-2}
MgO	1.2×10^{-2}
SO_3	3.1×10^{-2}
K_2O	3.3×10^{-3}
$CaCO_3$	5×10^{-2}
Total	1.01

with MCS CO_2 Suppression from Metrohm. The measured components were Ca, SO_4, K, Na and the pH. The pH was measured with a pH-meter. Data obtained are compared with the ones calculated by the numerical model (Figure 5.3). During the experiment, the hydraulic conductivity decreased with time by a factor of 1000, which could be due to mineral precipitation. Figure 5.1 shows the evolution of the hydraulic conductivity during the test.

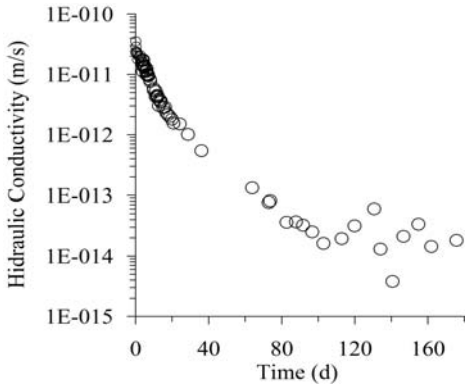

Figure 5.1: Evolution of hydraulic conductivity.

5.3 Numerical Model

To interpret the experiment and deduce processes and chemical reactions a reactive transport model was developed. It takes into account matrix diffusion as described in the previous chapter (Section 4.3). The domain consists of a mobile zone representing the well connected pores with advection, dispersion and diffusion, and an immobile zone representing the matrix, where there is only diffusion. Slabs were considered as the geometry of the immobile zone. Figure 5.2 displays the mesh used in the numerical model, where both zones are represented. The mesh is composed of 561 nodes and 560 linear elements. The *y* axis represents the mobile zone with a length of 5.52 cm, and contains 50 nodes. For each node of the mobile zone there is an immobile zone (*x* direction) with 10 nodes, which is dimensionless. The calibrated parameters for deuterium (porosity of the mobile zone and characteristic time) obtained in the previous chapter were used (Table 4.2). The simulations were carried out using the reactive transport code Retraso-CodeBright (*Saaltink et al.*, 2004).

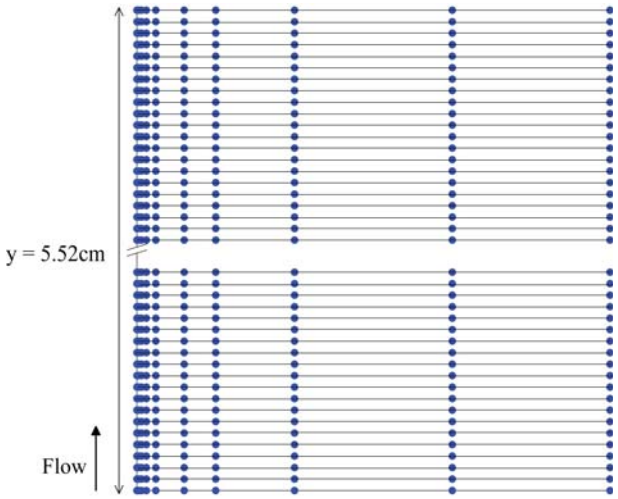

Figure 5.2: Mesh used for the numerical model, where *y* axis represents the mobile zone and *x* the immobile zone

5.3.1 Mineral Phases

Table 5.2 shows the phases taken into account in the numerical model. The minerals considered by the numerical model were detected by X-ray diffraction. The cement paste is composed of alite and belite, which are the residual clinker, C-S-H gel, gypsum, calcite, portlandite and ettringite. Aggregates are composed mainly of quartz. Monosulphate or other minor phases were not considered because they were not found by X-ray diffraction. The C-S-H gel is not a pure phase, but a solid solution with varying Ca/Si ratios. As the reactive transport code can only handle pure minerals, this is modelled by assuming 19 pure minerals with Ca/Si ratios ranging from 0.83 to 1.67 as was done by *Trapote-Barreira et al.* (2014). We used the C-S-H-1667 gel as primary phase and the others as secondary phases. We did not consider minerals in the mobile zone, all of them are located in the immobile zone, which represents the matrix. We used a porosity for the mobile zone of 0.029 and one for the immobile zone equal to 0.141 (Table 4.2). The volumetric fractions of the phases (Table 5.2) were calculated from Equations 5.1, 5.2 and 5.3. The initial reactive areas of calcite, ettringite, portlandite and C-S-H gel are from *Trapote-Barreira* (2015). The ones for alite, belite, gypsum and quartz were calibrated by fitting the model results to the experimental data.

$$\mathbf{u}_i = \mathbf{S}_i^{ox} M_i^{ox} \rho^{cem} \omega_i \tag{5.1}$$

$$\mathbf{c}_j = (\mathbf{S}_i^{min})^{-1} \mathbf{u} \tag{5.2}$$

$$f_j = \mathbf{c}_j f^{cem} v_j \tag{5.3}$$

Where sub index i and j refers to elements (Ca, Si, Al, S and C) and minerals (C-S-H gel, portlandite, ettringite, gypsum, calcite alite and belite) respectively. Super index ox, min and cem mean oxide, mineral and cement respectively. $\mathbf{u}_i$ is the concentration of element (mol/cm^3), **S** is a stoichiometric matrix, M the molecular weigh (g), ρ density (g/cm^3), ω is the mass fraction of oxide (Table 5.1), **c** is the concentration of mineral (mol/cm^3), v_j is the molar volume (cm^3/mol), f_j volumetric fraction of the mineral (cm^3/cm^3) and f^{cem} is the volumetric fraction of the cement (cm^3/cm^3).

Table 5.2: Phases used in the numerical model for the mobile and immobile zones.

Phase	Mobile V_{phase}/Vt	σ_{mo} (m^2m^{-3})	Immobile V_{phase}/Vt	σ_{im} (m^2m^{-3})	Total V_{phase}/Vt
Alite	0	0	5.63×10^{-3}	0.7 [(a)]	5.63×10^{-3}
Belite	0	0	4.01×10^{-3}	0.7 [(a)]	4.01×10^{-3}
Gypsum	0	0	1.17×10^{-3}	0.01 [(a)]	1.17×10^{-3}
Calcite	0	0	6.12×10^{-3}	5073 [(b)]	6.12×10^{-3}
Quartz	0	0	0.63*	10 [(a)]	0.63*
Ettringite	0	0	3.21×10^{-2}	116007 [(b)]	3.21×10^{-2}
Portlandite	0	0	6.92×10^{-2}	8270 [(b)]	6.92×10^{-2}
C-S-H-1667	0	0	7.97×10^{-2}	1649468 [(b)]	7.97×10^{-2}
Porosity	0.029		0.141		0.17
Total	0.029		0.971		1

* Volume of aggregates with respect to the total volume of the sample. a) calibrated, b) *Trapote-Barreira* (2015).

5.3.2 Thermodynamic Data

Table 5.3 shows the thermodynamic data used in the numerical model, at 25 °C. For the clinker phases alite and belite, irreversible kinetics have been used. Data for gypsum, calcite and quartz are taken from the EQ3/6 database (*Wolery et al.*, 1990). The data of the

discretized C-S-H gel are taken from *Trapote-Barreira et al.* (2014), were calculated from the solid solution model reported by *Kulik and Kersten* (2001). The thermodynamic data of portlanidte is taken form *Hummel et al.* (2002) and the one for ettringite is from *Lothenbach and Winnefeld* (2006). Also aqueous complexation reactions were included. These were selected by means of a speciation calculation with PHREEQC (*Parkhurst and Appelo*, 1999).

Table 5.3: Equilibrium constants taken into account in the numerical model. Only the end-members are shown in the C-S-H solid solution. Reactions are written as the dissolution of mol of mineral in terms of the primary species Ca^{2+}, $SiO_2(aq)$, $Al(OH)_4^-$, H^+, SO_4^{2-} and HCO_3^-) are written as dissolution of 1 mol mineral. They are taken from a) EQ3/6 database (*Wolery et al.*, 1990), b) *Trapote-Barreira et al.* (2014) c) *Hummel et al.* (2002) d) *Lothenbach et al.* (2008).

Solid	Formula	log K_{eq}
Alite	C_3S ($3CaO{\cdot}SiO_2$)	irreversible
Belite	C_2S ($2CaO{\cdot}SiO_2$)	irreversible
Gypsum	$CaSO_4 \cdot H_2O$	-4.48 [(a)]
Calcite	$CaCO_3$	1.84 [(a)]
Quartz	SiO_2	-3.99 [(a)]
C-S-H-083	C-S-H ss, Ca/Si=0.83	11.15 [(b)]
C-S-H-1667	C-S-H ss, Ca/Si=1.667	29.13 [(b)]
Portlandite	$Ca(OH)_2$	22.80 [(c)]
Ettringite	$Ca_6Al_2(SO_2)_3(OH)_{12}26H_2O$	-44.90 [(d)]

5.3.3 Kinetic Rate Laws

A kinetic approach is used for the dissolution-precipitation of mineral phases, although sometimes the reaction is fast enough to be practically at equilibrium. The kinetic rate constants used in the numerical model are showed in table 5.5. Two types rate laws have

Table 5.4: Secondary species with their equilibrium constants (log K_{eq}) taken into account in the numerical model.

Formula	log K_{eq}	Formula	log K_{eq}
$Al(OH)_6SiO^-$	-3.60	$CaHCO_3^+$	-1.04
$Al(OH)_3(aq)$	16.15	$CO_2(aq)$	-6.34
$Al(OH)_2^+$	10.09	KOH(aq)	14.46
$AlOH^{2+}$	5.01	KSO_4^-	-0.87
$AlSiO(OH)_3^{2+}$	-7.40	$NaCO_3^-$	-0.51
$AlSO_4^+$	-3.01	NaOH(aq)	14.18
$AlSO_4^{-2}$	-4.9	$NaSO_4^-$	-0.82
$CaCO_3(aq)$	7.00	$NaHCO_3(aq)$	-0.15
$CaOH^+$	12.85	HSO_4^-	-1.97
$CaSO_4(aq)$	-2.11	$SiO(OH)_3^-$	9.80
$CaSiO_2(OH)_2$	-4.60	$SiO_2(OH)_2^{2-}$	23.13
$CaSiO(OH)_3^+$	-1.20		

been considered. We used irreversible rates for alite and belite (Equation 5.4). The rates for the other minerals correspond to Equation 5.5. The log k for alite and belite have been taken from *Savage et al.* (2011). Data for the other minerals are from *Trapote-Barreira et al.* (2014).

$$r = k\sigma \tag{5.4}$$

$$r = k\sigma a_{H_+}^n (1 - \Omega) \tag{5.5}$$

r is the mineral dissolution-precipitation rate (mol m^{-2} s^{-1}), k is the kinetic rate constant (mol m^{-2} s^{-1}), σ is the surface area (m^2m^{-3}), a_{H^+} is the activity of H^+, n is a coefficient

determined experimentally and Ω is the ratio between the ion activity product and the equilibrium constant.

Table 5.5: Rate constants (log k) used in the numerical model. They are from a) *Savage et al.* (2011) or b) *Trapote-Barreira et al.* (2014)

Solid	log k (mol m^{-2} s^{-1})	n
Alite	-5.5 [(a)]	0
Belite	-6.5 [(a)]	0
Gypsum	-6 [(b)]	0
Calcite	5.81 [(b)]	0
Quartz	-14.9 [(b)]	-0.4
C-S-H-083	-10.99 [(b)]	0
C-S-H-1667	-8.40 [(b)]	0
Portlandite	-5.14 [(b)]	0
Ettringite	-8.80 [(b)]	0

5.3.4 Solution Composition

The initial compositions of the pore water and the infiltration water are given in Tables 5.6, 5.7 and 5.8. The pore waters for the mobile and immobile zones are different. In the immobile zone (Table 5.6) the water is assumed to be electrically neutral and in equilibrium with C-S-H-1667, ettringite, calcite and portlandite, and the total aqueous concentrations of Na, K and SO_4 equal the measured values. However, the pore water in the mobile zone (Table 5.7) is not in equilibrium with the cement phases. Total concentrations of Ca, Si and Al are adjusted to fit the numerical model to the first measured breakthrough data. Na and CO_3 concentrations are calculated assuming charge balance and equilibrium with calcite. We used the measured values for pH and K and S concentrations.

The infiltration water (Table 5.8) contains Ca and K, which were measured. CO_3 con-

centration and pH were calculated assuming equilibrium with calcite and charge balance. Concentrations of other components are practically zero.

Table 5.6: Initial composition of pore water in the immobile zone

Component	Concentration (mol L^{-1})	Constraint
Ca^{2+}	2.62×10^{-3}	charge balance
$SiO_2(aq)$	2.99×10^{-5}	equilibrium C-S-H-1667
$Al(OH)_4^-$	3.11×10^{-6}	equilibrium ettringite
K^+	0.132	measured
Na^+	0.0253	measured
SO_4^{2-}	1.9×10^{-3}	measured
CO_3^{2-}	2.67×10^{-5}	equilibrium calcite
pH	13.04	equilibrium portlandite

Table 5.7: Initial composition of pore water in the mobile zone

Component	Concentration (mol L^{-1})	Constraint
Ca^{2+}	1×10^{-5}	adjusted
$SiO_2(aq)$	4.3×10^{-4}	adjusted
$Al(OH)_4^-$	2.65×10^{-5}	adjusted
K^+	0.132	measured
Na^+	0.18	charge balance
SO_4^{2-}	1.9×10^{-3}	measured
CO_3^{2-}	3.45×10^{-2}	equilibrium calcite
pH	13.2	measured

Table 5.8: Composition of the infiltration water

Component	Concentration (mol L^{-1})	Constraint
Ca^{2+}	1.21×10^{-3}	measured
$SiO_2(aq)$	1×10^{-15}	
$Al(OH)_4^-$	1×10^{-15}	
K^+	0.159	measured
Na^+	1×10^{-15}	
SO_4^{2-}	1×10^{-15}	
CO_3^{2-}	5.27×10^{-5}	equilibrium calcite
pH	13.2	charge balance

5.4 Results and discussion

5.4.1 Solution composition

The evolution of the measured concentrations at the oulet of the experiment are compared with the model results in Figure 5.3. Only Ca, SO_4, K, Na and pH were measured. There are no experimental data for Si, Al and CO_3. Two models are compared, one with an initial surface area of portlandite (σ) of 8270 m^2m^{-3}, where the solution is practically in equilibrium with portlandite, and another one with an initial surface area of 0.0827 m^2m^{-3}, where portlandite dissolution is controlled by kinetics. Both models give identical results for K and Na (because these components are conservative) and have similar results for CO_3 and pH, obtaining good fits. However, they differ for the other components. The model where portlandite is in equilibrium (σ=8270 m^2m^{-3}) does not fit well measured Ca. The model predicts constant Ca concentrations of 2.5×10^{-3} mol/l, whereas measured data indicate an under-saturation of portlandite at the beginning of the test, and afterwards an

over-saturation. This is reflected better by the model with σ=0.0827 m^2m^{-3}. Similar results for Si are obtained for both models, but the concentration of Si increases rapidly at the beginning in the model where σ is 0.0827 m^2m^{-3}, because the concentration of Ca increases slowly. Likewise, the concentrations of SO_4 and Al increase rapidly at the beginning in the model with σ=0.0827 m^2m^{-3}. Both models have a good fit for SO_4.

Figures 5.4 and 5.5 show concentrations versus dimensionless distance into the immobile zone at the inlet (y=0 cm) and outlet (y=5.5 cm) of the sample and for two different times (at 0.2 and 14 days). In the x axis, 0 represents the mobile zone and the immobile zone starts from there, according with Figure 5.2. Figure 5.4 displays the results of the model with σ=8270 m^2m^{-3} and Figure 5.5 the ones with a σ=0.0827 m^2m^{-3}. A similar concentration of Ca is obtained for the whole domain and all times, when portlandite is in equilibrium (σ=8270 m^2m^{-3}). However, when portlandite is in kinetics (σ=0.0827 m^2m^{-3}), the concentration of Ca increases with time and also throughout the immobile zone, due to the dissolution of the clinker phases (alite and belite). Both models have the identical results for K and Na as these are conservative components. K increases slightly with time because the infiltration water has a higher concentration of K than the pore water. On the other hand, Na decreases with time because the infiltration water does not contain Na. For all the other components, both models have similar results with only small differences due to the pore water composition of the mobile zone.

5.4.2 Mineral variation

The variation of volumetric fraction of minerals versus dimensionless length (of immobile zone) are displayed in Figures 5.6 and 5.7. Like in the previous subsection, they compare the mineral variation at the inlet and outlet of the sample (y=0 cm and y=5.5 cm respectively) and two different times (0.2 and 14 days). Figure 5.6 shows the model results when

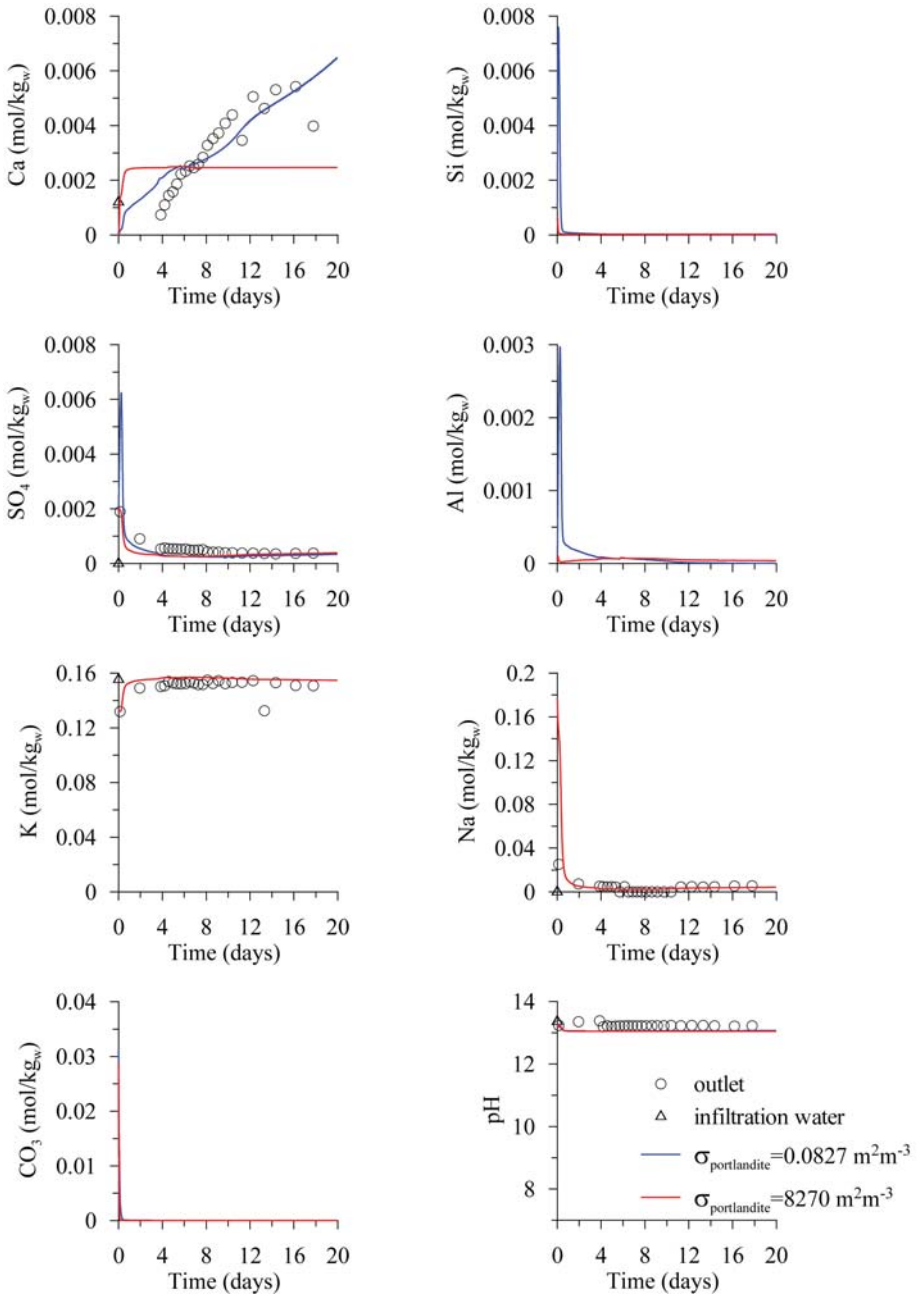

Figure 5.3: Evolution of the measured concentration (points) compared with the ones calculated by the numerical model (lines). The triangles represent the concentration of the infiltration water. No data were available for Si, Al and CO_2.

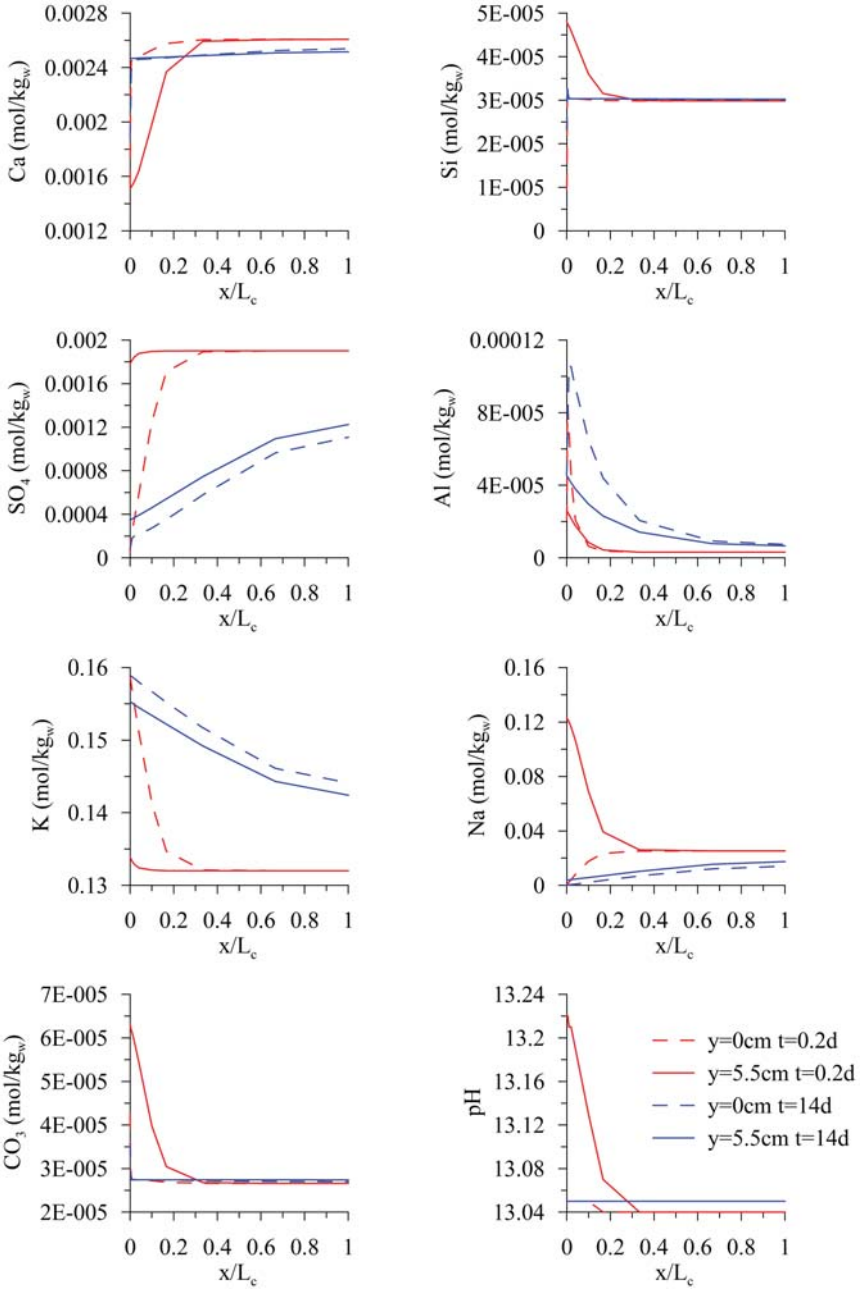

Figure 5.4: Concentration of each component against dimensionless length (immobile zone), for a σ=8270 m^{2}m^{-3}

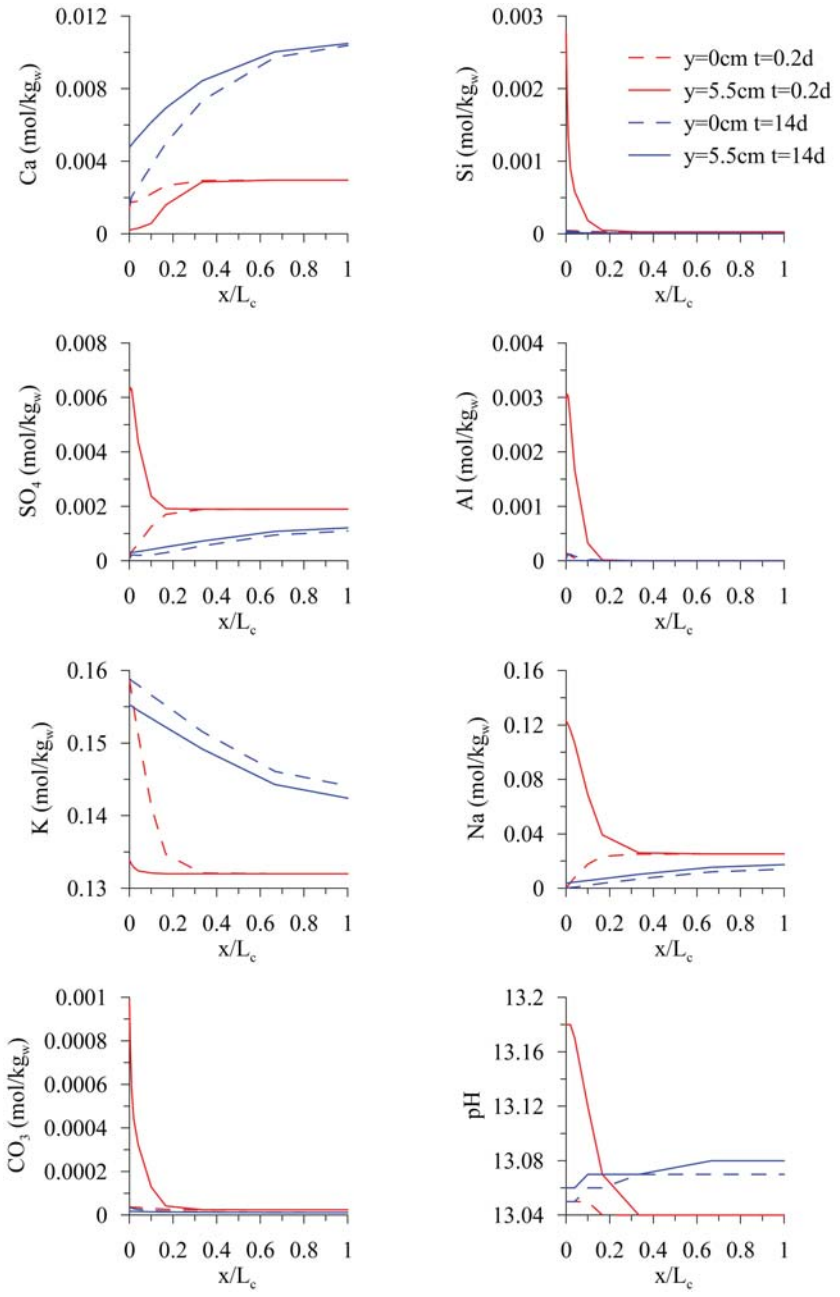

Figure 5.5: Concentration of each component against dimensionless length (immobile zone), for a σ=0.0827 m^{2}m^{-3}

portlandite is in equilibrium (σ=8270 m^2m^{-3}) and Figure 5.7 when the portlandite is controlled by kinetics (σ=0.0827 m^2m^{-3}). Both models show a dissolution of alite and belite that is constant in the whole domain, because of the simplicity of their irreversible rate laws (Equation 5.4). Gypsum and quartz are also dissolving in both models in a similar way as the clinker phases. On the other hand, calcite precipitates at the beginning of the immobile zone (near x=0). Ettringite is dissolving near the mobile zone. Both models show similar results for C-S-H gel, which is dissolving near the mobile zone ant then it precipitates, due to clinker dissolution. When σ of portlandite is 8270 m^2m^{-3} there is higher precipitation of portlandite and calcite than the model with lower σ, giving a constant value of Ca (Figure 5.4). Hence, lower precipitation of portlandite (σ=0.0827 m^2m^{-3}) gives a better fit for Ca (Figure 5.3).

5.4.3 Porosity

Modelled porosity only changes in the immobile zone, because the surface area of all mineral in the mobile zone are zero. Hence, this conceptual model cannot reproduce the decrease of the hydraulic conductivity. Another conceptual model with minerals in both mobile an immobile zone was also considered. The initial pore water in the mobile zone was in equilibrium with portlandite. However, the first measured solid composition at the outlet is not at equilibrium with portlandite (first under-saturated and then over-saturated). The numerical model could not fit the experimental data for Ca when there is portlandite in the mobile zone. It was for this reason that we did not consider minerals in the mobile zone, starting with an initial pore water in the mobile zone consistent with the first measured data at the outlet of the sample. According to the model, porosity change occurs in the immobile zone, which theoretically does not affect permeability. So the question on the causes of the permeability reduction is still open. One explanation is to consider that

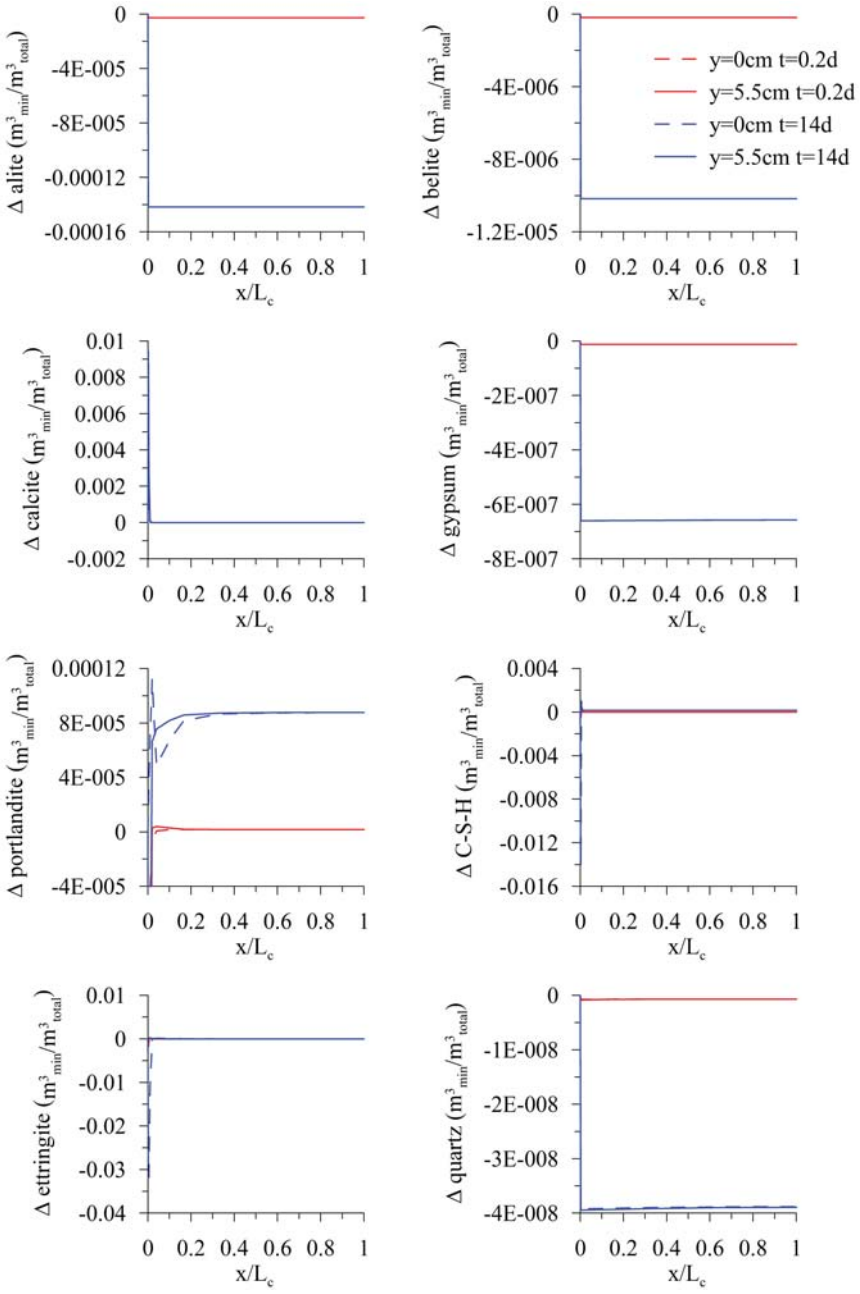

Figure 5.6: Variation of volumetric fraction of minerals against dimensionless length (immobile zone), for a σ=8270 m^2m^{-3}. Positive values mean precipitation and negative ones mean dissolution.

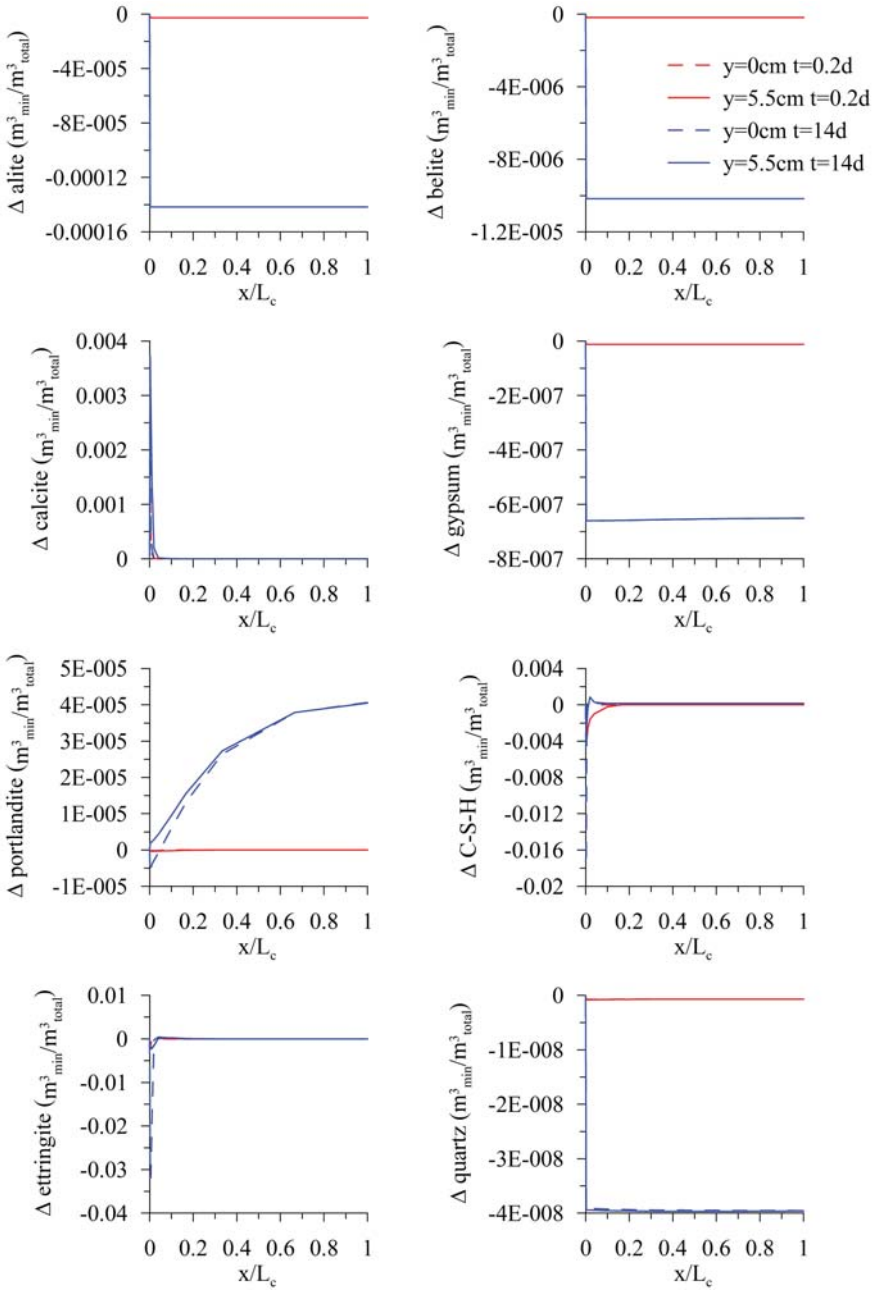

Figure 5.7: Variation of volumetric fraction of minerals against dimensionless length (immobile zone), for a σ=0.0827 m^2m^{-3}. Positive values mean precipitation and negative ones mean dissolution.

the immobile zone not only represents the pores inside the matrix but also the edges of the connecting pores. Precipitation at these edges (calcite, C-S-H, portlandite), though in the immobile zone, could narrow the pores of the mobile zone. Another explanation could be that dissolution could cause the detachment of solid particles that clog smaller pores, thus reducing permeability. This has been observed for carbonate materials (*Garing et al.*, 2015).

The variation of porosity in the immobile zone for both models is displayed in Figure 5.8. Both cases show an increase in porosity due to mineral dissolution in the matrix, being higher, around a factor of 2, when portlandite is considered in equilibrium (large surface area). The minerals that are dissolving are alite, belite, gypsum and ettringite.

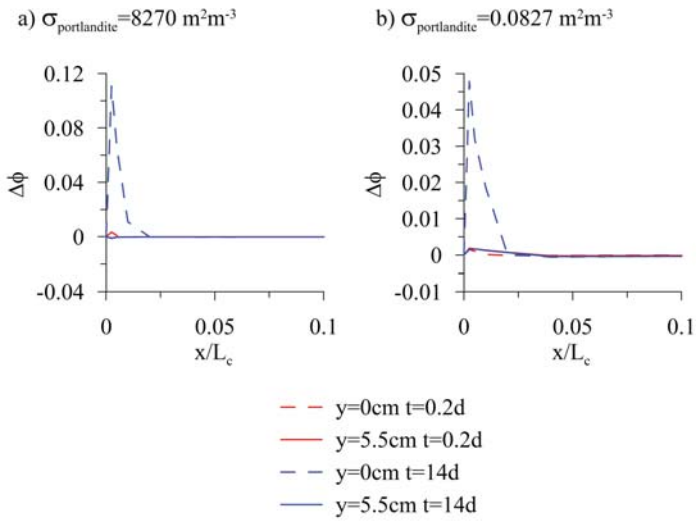

Figure 5.8: Variation of porosity against dimensionless length (immobile zone).

5.5 Conclusions

Reactive transport models of a high-pH infiltration test in concrete have been developed taking into account matrix diffusion. The model domain consists of a mobile zone representing the well connected pores (with advection, dispersion and diffusion) and an immobile zone representing the matrix (only diffusion). All mineral phases are located in the immobile zone. The cement phases that are taken into account in the numerical model are alite and belite (residual clinker), gypsum, calcite, C-S-H gel, portlandite and ettringite. The aggregates are composed of quartz. The initial pore water in the immobile zone is in equilibrium with the cement phases, but the initial pore water in the mobile zone is consistent with the first measured concentrations (early breakthrough). This conceptual model allows a reasonable fit of the model to the experimental data.

Two different models are compared, one with portlandite in equilibrium (hight initial surface area) and another one with portlandite reaction controlled by kinetics (low initial surface area). When porlandite is in equilibrium, modelled Ca concentrations are practically constant and cannot reproduce the measured data, where Ca is first under-saturated with portlandite and then over-saturated. The model with porlandite controlled by kinetics can reproduce this behaviour. The other components are similar for both models obtaining a good fit to the measured data.

The changes in mineralogy calculated for the models show a dissolution of alite, belite, gypsum and quartz. Near the mobile zone ettringite dissolves and calcite precipitates. Both models have similar results for C-S-H gel; it first dissolves near the mobile zone and then precipitates due to clinker dissolution. When the initial surface area is higher there is higher precipitation of portlandite and calcite, keeping the Ca concentration constant. But the measured data suggest slower precipitation of portlandite (low surface area) because a better

fit for Ca is obtained.

The numerical model cannot reproduce the changes in permeability because the surface area in the mobile zone is zero. However, the permeability could have decreased due to mineral precipitation (calcite, portlandite and C-S-H gel). In the immobile zone, both models show an increase of porosity because of mineral dissolution (clinker phases, ettringite and gypsum).

Chapter 6

General conclusions

This thesis focused on the study of transport of water (liquid and gas), heat and solutes in the concrete used to store radioactive waste. The main contributions of this thesis are summarized in this concluding chapter.

Two evaporation test in concrete columns have been analysed by means of numerical models. One at room conditions and the other heated by a lamp. The calibration of these models allowed to obtain the retention curve, the relative permeability, the thermal conductivity and the tortuosity factor. The drying retention curve estimated by the measured relative humidity and gravimetric water content shows that this concrete is a very retentive material, reflected by a high entry pressure. Relative permeability, the thermal conductivity and the tortuosity factor are obtained by fitting the numerical model results to the experimental data. According to the models vapour diffusion is the dominant water transport above the evaporation front, where water is mainly in the gas phase. Below this front, the dominant process is advection of liquid water. Assuming a homogeneous medium, only the upper part of the column is necessary to reach steady state in order to estimate the thermo-

hydraulic parameters. Hence, in comparison to classical methods for obtaining retention curves and relative permeabilities this method is useful especially for low-permeability materials because it accelerates the acquirement of the thermo-hydraulic parameters.

Numerical models have been carried out in order to explain why water is collected at the drain of the concrete cells where radioactive waste is stored. Measured temperature and relative humidity, thermo-hydraulic parameters from laboratory tests and measured leakage rate are used in the models. The numerical models suggest that a combination of the following processes have to be taken into account: the seasonal temperature gradients affecting the cell; diffusion thought the air gap between the wall of the cell and the containers; the phreatic level; and gas flow through the gravel separating different zones of containers. The models demonstrate that there is a temperature gradient between the wall of the cells and the wall of the containers allowing vapour diffusion through the air gap between them. Models also demonstrate that the leakage is produced by condensation and evaporation processes inside the cell. Calculated relative humidity shows that in summer the wall is drier due to evaporation, and the container is saturated because of condensation. In winter it is the opposite (condensation at the wall of the cell and evaporation at the container). The models also show that water enters the cell by capillary rise from the phreatic level and leaves it at the drain. Moreover, oscillations of relative humidity inside the cell measured by the sensors can be caused by gas convection inside the gravel. Different scenarios have been studied that can prevent this phenomenon. Temperature gradients can be avoided by filling the air gaps with sand or strongly reduced with a multi-layer cover. Using a cover and capillary barrier the flow of water from the phreatic level could be reduced considerably. In all of these cases no water is collected in the drain.

A tracer test in a concrete sample has been performed using a high entry pressure. Deuterium and bromide breakthrough curves has been simulated in order to find porosities and

a characteristic time for matrix diffusion by fitting the experimental data to the model results. Satisfactory fits could only be obtained by assuming a matrix diffusion conceptual model, that contains a mobile pore domain, with advection, dispersion and diffusion, and an immobile zone with only diffusion. Three geometries have been compared in order to represent the immobile zone: slabs, spheres and tubes. From the calibration of the deuterium breakthrough curve similar porosities for the three geometries are obtained, the ones for the immobile zone being the highest. In contrast the characteristic time depends on the geometry used. Similar fittings for all geometries are obtained, indicating that this kind of test cannot determinate the geometry of the immobile zone. The numerical model cannot reproduce the bromide breakthrough curve, even when linear retention is considered. Findings suggest that the double-porosity model should be taken into account for studying the transport of solutes in this kind of concrete.

Reactive transport models have also been developed in order to study the mineralogical changes in concrete during the performance of the tracer test. Matrix diffusion have also been considered, representing the immobile zone by slabs. The cement phases considered by the model are alite, belite, gypsum, calcite, C-S-H gel, portlandite and ettringite. The aggregates are composed of quartz. In order to obtain acceptable fits, all minerals are assumed to react with water in the immobile zone. The initial pore water of the immobile zone is in equilibrium with the cement phases, and the one for the mobile zone is in accordance with the measured data. Two numerical models are compared, one using a high surface area (equilibrium) and the other with a low surface area of portlandite. Only the model with a low surface area could fit the measured data of Ca. The models show dissolution of alite, belite, gypsum and quartz. There is precipitation of ettringite and calcite in both models. C-S-H gel dissolves near the mobile zone and the precipitates due to clinker dissolution. When a low surface area of portlandite is used lower precipitation of portlandite is pro-

duced. Changes in porosity of the mobile zone cannot be reproduced because the surface area of the minerals is zero. However, the permeability could decrease due to mineral precipitation (calcite, portlandite and C-S-H gel). The numerical models show an increase of the porosity in the immobile zone because of mineral dissolution.

Appendix A

Constitutive laws (Chapters 2 and 3)

A.1 List of symbols

A	constant for relative permeability
a_w	activity of water
D	parameter for diffusion
D_m	molecular diffusion coefficient ($m^2 s^{-1}$)
D'_α	mechanical dispersion coefficient ($m^2 s^{-1}$)
d_l	longitudinal dispersivity (m)
E_α	internal energy per unit of mass for each phase (J kg^{-1})
E^i_α	specific internal energy (J kg^{-1})
f	external supply of component
g	gravity (m s^{-2})
HR	relative humidity
i	(superscript) component index, w water, a dry air and h salt

i_α	diffusive or dispersive flux (J s^{-1} m^{-2})
i_c	heat conductive flux (J s^{-1} m^{-2})
j^i_α	mass flux of component in each phase (J s^{-1} m^{-2})
j^w_g	vapour flux (kg s^{-1} m^{-2})
j_e	energy flux (J s^{-1} m^{-2})
j^0_e	radiation (J s^{-1} m^{-2})
k_i	intrinsic permeability (m^2)
k_r	relative permeability
M^i	molecular weight of component i (kg mol^{-1})
m	shape parameter for retention curve
n	parameter for relative permeability
P_α	pressure of phase α (MPa)
P^i_α	partial pressure of component i in phase α (MPa)
$P^w_{g,sat}$	saturated vapour pressure (MPa)
P_0	entry pressure (MPa)
P_{l0}	reference pressure (MPa)
q_α	flow rate (ms^{-1})
R	ideal gas constant (J mol^{-1} K^{-1})
S_α	saturation of phase α
S_e	effective water saturation
T	temperature (°C)
w	gravimetric humidity
α	(subscript) phase index, l liquid, s solid and g gas
β	compressibility (MPa^{-1})
β_g	boundary vapour exchange coefficient (ms^{-1})
γ	solute variation coefficient

γ_g	boundary gas exchange coefficient (kg s $^{-1}$m^{-2}MPa^{-1})
γ_e	boundary heat exchange coefficient (J s^{-1}m^{-2} °C^{-1})
ϵ	volumetric thermal expansion coefficient for liquid (°C^{-1})
λ	thermal conductivity (W m^{-1} K^{-1})
μ_α	viscosity of phase α (MPa s)
θ_α	volumetric phase content of α
ρ_α	density of phase α (kg m^{-3})
ρ_{l0}	reference density of the liquid (kg m^{-3})
σ_{l0}	Surface tension at temperature T (N m^{-1})
τ	tortuosity
ϕ	porosity
ω_α^i	mass fraction of solute i in phase α (kg kg^{-1})

A.2 Constitutive laws

A.2.1 Definition constraints

Mass fractions

$$\omega_l^w + \omega_l^a + \omega_l^h = 1 \tag{A.1}$$

$$\omega_g^w + \omega_g^a = 1 \tag{A.2}$$

Volumetric content

$$\theta_l = \frac{V_l}{V_t} = \frac{1}{\rho_l} w \rho_s (1 - \phi) \tag{A.3}$$

Saturations

$$S_l + S_g = 1 \tag{A.4}$$

$$S_l = \frac{V_l}{V_p} = \frac{\theta_l}{\phi} \tag{A.5}$$

Partial pressures

$$P_g^a + P_g^w = P_g \tag{A.6}$$

A.2.2 Equilibrium constraints

Vapour-liquid water (psychrometric law)

$$P_g^w = a_w P_{g,sat}^w \exp\left(\frac{-(P_g - P_l) M^w}{R \rho_l (273.15 + T)}\right) \tag{A.7}$$

$$P_{g,sat}^w = 136075 \exp\left(\frac{-5239.7}{273.15 + T}\right) \tag{A.8}$$

$$a_w = 1 - \left(\left(\omega_l^h \frac{1000}{M^h - 3}\right) 1.9775 \cdot 10^{-5} T + 0.035\right) \omega_l^h \frac{1000}{M^h - 3} \tag{A.9}$$

where M^h=49.37 g mol^{-1}

$$HR = \frac{P_g^w}{P_{g,sat}^w} \tag{A.10}$$

$$\omega_g^w = \frac{P_g^w M^w}{R\rho_g(273.15 + T)} \tag{A.11}$$

Dissolved-gaseous air (Henry's law)

$$\omega_l^a = \frac{P_g^a M^a}{H M^w} \tag{A.12}$$

A.2.3 Phase and interphase properties

Retention curve (van Genuchten law)

$$S_e = \left(1 + \left(\frac{P_g - P_l}{P_0 \frac{\sigma_T}{\sigma_0}}\right)^{\frac{1}{1-m}}\right)^{-m} \tag{A.13}$$

where P_0=7.7 Mpa, m=0.34, σ_T is the surface tension at temperature T and σ_0=0.072 N/m at 20°C

Relative permeability

$$k_{rl} = AS_{el}^n \tag{A.14}$$

where A=0.01 and n=7

$$k_{rg} = AS_{eg}^{n} \tag{A.15}$$

where A=1 and n=3

Properties of liquid

$$\rho_l = \rho_{l0} \exp\left(\beta(P_l - P_{l0}) + \epsilon T + \gamma\omega_l^h\right) \tag{A.16}$$

where ρ_{l0}=1002.6 kg m^{-1}, P_{l0}=0.1 MPa, β=4.5·10^{-4} MPa^{-1}, γ=0.6923 and ϵ=3.4·10^{-4} $^{\circ}$C^{-1}

$$\mu_l = 2.1 \cdot 10^{-12}\left(\frac{1808.5}{273.15 + T}\right) \tag{A.17}$$

$$\sigma_T = \left(1 - 0.625\left(\frac{273.15 + T}{647.3}\right)\right)\left(0.2358\left(\frac{273.15 + T}{647.3}\right)^{1.256}\right) + 0.04055\omega_l^h \tag{A.18}$$

$$E_l = E_l^w\omega_l^w + E_l^a\omega_l^a \tag{A.19}$$

where E_l^w=4184T J kg^{-1} and E_l^a=1000T J kg^{-1}

Properties of gas

$$\rho_g = \frac{P_g^w M^w}{R(273.15 + T)} + \frac{P_g^a M^w}{R(273.15 + T)} \tag{A.20}$$

where M_g^a=0.02895 kg mol^{-1} and H=10000 MPa

$$\mu_g = \frac{1.48 \cdot 10^{-12}\sqrt{273.15+T}}{1+\frac{119.4}{T+273.15}} \frac{1}{1+\frac{0.14-1.2\cdot 10^{15}k_i}{P_g}} \tag{A.21}$$

$$E_g = E_g^w \omega_g^w + E_g^a \omega_g^a \tag{A.22}$$

where E_g^w=2.5·10^6+1900T J kg^{-1} and E_g^a =1000T J kg^{-1}

Properties of solid

The density of the solid phase (ρ_s) is 2360 kg m^{-1} and E_s =780T J kg^{-1}

A.2.4 Fluxes

Darcy's flux

$$q_\alpha = -\frac{k_i k_{r\alpha}}{\mu_\alpha}(\nabla P_\alpha - \rho_\alpha g) \tag{A.23}$$

where k_i=4.2·10^{-18} m^2

Diffusive flux (Fick's law)

$$i^i_{\alpha,dif} = -(\tau\phi\rho_\alpha S_\alpha D^i_m) \nabla \omega^i_\alpha \tag{A.24}$$

where $\tau_{non-heated}$=0.08 and τ_{heated}=0.3

$$D_m^{vapor} = D\left(\frac{(273.15+T)^n}{P_g}\right) \tag{A.25}$$

where D=5.9·10^{-6} m s^{-1} K^{-n} Pa and n=2.3

$$D_m^{solute} = D \exp\left(\frac{-24530}{R(273.15 + T)}\right) \tag{A.26}$$

where D=1.1·10^{-4} m^2 s^{-1}

Dispersive flux (Fick's law)

$$i^i_{\alpha,dis} = -(\rho_\alpha D'_\alpha) \nabla \omega^i_\alpha \tag{A.27}$$

$$D'_\alpha = d_l q_\alpha \tag{A.28}$$

where d_l=0.015 m

Mass flux

$$j^i_\alpha = q_\alpha \rho_\alpha \omega^i_\alpha + i^i_{\alpha,dis} + i^i_{\alpha,dif} \tag{A.29}$$

Conductive flux of heat (Fourier's law)

$$i_c = -\lambda \nabla T \tag{A.30}$$

$$\lambda = \lambda_{sat}^{S_l} \lambda_{dry}^{1-S_l} \tag{A.31}$$

where λ_{sat}=1.14 W m K^{-1} and λ_{dry}=0.66 W m K^{-1}

Advective flux of heat

$$j_{E\alpha} = q_\alpha E_\alpha \tag{A.32}$$

Appendix B

List of publications

Journal Articles

Chaparro, MC, Saaltink MW, Villar MV (2015) Characterization of concrete by calibrating thermo-hydraulic multiphase flow models, Transport in Porous Media 109:147-167, DOI 10.1007/s11242-015-0506-9.

Chaparro, MC, Saaltink MW, Soler JM, Slooten LJ, Mäder UK (2016), Modelling of matrix diffusion in a tracer test in concrete, Transport in Porous Media, 111:27-40, DOI 10.1007/s11242-015-0579-5.

Chaparro, MC and Saaltink MW. Water, vapour and heat transport in concrete cells for storing radioactive waste. In Revision.

Conferences

Chaparro, MC, Soler JM, Saaltink MW, and Mäder UK, (2015), Modelling of reactive transport in a high-pH infiltration test in concrete, 6th Workshop of the PhD network on Reactive Transport Modeling and Experiments, Forschungszentrum Jülich, Germany.

Chaparro, MC and Saaltink MW (2015), Multiphase flow models of concrete cells of the radioactive waste disposal facility at 'El Cabril', 7th Workshop of CODE_BRIGHT Users, Barcelona, Spain, p.1-4.

Chaparro, MC and Saaltink MW (2014), Monitorización y procesos capilares en las estructuras de almacenamiento de C.A. de El Cabril, VI Jornadas de investigación y desarrollo tecnológico en gestión de residuos radioactivos, Cuenca, Spain.

Chaparro, MC and Saaltink MW (2014), Modelling of multiphase flow in concrete cells of the radioactive waste storage facility at 'El Cabril' (Spain), 2nd International symposium on cement-based materials for nuclear waste (Nuwcem), Avignon, France, p.1-8.

Chaparro, MC, Saaltink MW, Soler JM, Slooten LJ and Mäder UK, (2014), Modelling matrix diffusion in high-pH infiltration test in concrete columns, European Geosciences Union General Assembly 2014, Vienna, Austria.

Chaparro, MC, Saaltink MW, Soler JM, Slooten LJ and Mäder UK, (2013), Modelling high-pH infiltration tests in concrete columns, 3rd Workshop of the PhD network on Reactive Transport Modeling and Experiments, Paul Scherrer Institut (PSI), Switzerland.

Chaparro, MC, Saaltink MW and Villar MV (2013), Interpretation of evaporation test in concrete columns by means of multiphase flow models, 5th Workshop of CODE_BRIGHT Users, Barcelona, Spain, p.1-4.

Chaparro, MC, Saaltink MW and Villar MV, (2013), Modelling of multiphase flow in evaporation test in concrete columns, European Geosciences Union General Assembly 2013, Vienna, Austria.

Chaparro, MC, Saaltink MW and Villar MV (2011), Modelación de flujo multifase en ensayos de evaporación en columna de hormigón, Estudios en la Zona no Saturada del Suelo, vol. 10, 205-210.

Technical Reports

Chaparro, MC and Saaltink MW (2012), Modelación de flujo multifase y transporte de tritio de la estructura de almacenamiento RBMA, Technical Report, UPC, Department of Geotechnical Engineering and Geosciences, 60pp.

Chaparro, MC and Saaltink MW (2010), Modelación termohidráulica de la estructura de almacenamiento RMBA y modelación de ensayos de evaporación de columnas de hormigón, Technical Report, UPC, Department of Geotechnical Engineering and Geosciences, 66pp.

Bibliography

Acero, P., C. Ayora, J. Carrera, M. W. Saaltink, and S. Olivella (2009), Multiphase flow and reactive transport model in vadose tailings, *Applied Geochemistry*, *24*(7), 1238–1250, doi:10.1016/j.apgeochem.2009.03.008.

Adler, M., U. Mäder, and H. Waber (2001), Core infiltration experiment investigating high-pH alteration of low-permeability argillaceous rock at 30 °C, *In: Cidu, R. (Ed.), Proceedings WRI-10 (10th International Symposium on Water-Rock Interaction). Balkema, Villasimius, Italy*, pp. 1299–1302.

Aimoz, L., E. Wieland, C. Taviot-Guého, R. Dähn, M. Vespa, and S. V. Churakov (2012), Structural insight into iodide uptake by AFm phases, *Environmental Science & Technology*, *46*, 3874–3881, doi:10.1021/es204470e.

Andrade, C., J. Sarría, and C. Alonso (1999), Relative humidity in the interior of concrete exposed to natural and artificial weathering, *Cement and Concrete Research*, *29*, 1249–1259, doi:http://dx.doi.org/10.1016/S0008-8846(99)00123-4.

Arya, S. P. (2001), *Introduction to Micrometeorology*, vol. vol 79, International Geophysics Series.

Atkinson, A., and A. K. Nickerson (1984), The diffusion of ions through water-saturated cement, *Journal of Materials Science*, *19*, 3068–3078.

Banimahd, S., and S. Zand-Parsa (2013), Simulation of evaporation, coupled liquid water, water vapor and heat transport through the soil medium, *Agricultural Water Management*, *130*, 168 – 177, doi:http://dx.doi.org/10.1016/j.agwat.2013.08.022.

Baroghel-Bouny, V. (2007), Water vapour sorption experiments on hardened cementitious materials: Part i: Essential tool for analysis of hygral behaviour and its relation to pore structure, *Cement and Concrete Research*, *37*(3), 414 – 437, doi:10.1016/j.cemconres.2006.11.019.

Baur, I., and C. A. Johnson (2003), Sorption of selenite and selenate to cement minerals, *Environmental Science & Technology*, *37*, 3442–3447, doi:10.1021/es020148d.

Bittelli, M., F. Ventura, G. S. Campbell, R. L. Snyder, F. Gallegati, and P. R. Pisa (2008), Coupling of heat, water vapor, and liquid water fluxes to compute evaporation in bare soils, *Journal of Hydrology*, *362*, 191 – 205, doi:http://dx.doi.org/10.1016/j.jhydrol.2008.08.014.

Bonhoure, I., I. Baur, E. Wieland, C. A. Johnson, and A. M. Scheidegger (2006), Uptake of Se(IV/VI) oxyanions by hardened cement paste and cement minerals: An X-ray absorption spectroscopy study, *Cement and Concrete Research*, *36*, 91–98, doi:http://dx.doi.org/10.1016/j.cemconres.2005.05.003.

Brue, F., C. A. Davy, F. Skoczylas, N. Burlion, and X. Bourbon (2012), Effect of temperature on the water retention properties of two high performance concretes, *Cement and Concrete Research*, *42*(2), 384–396, doi:10.1016/j.cemconres.2011.11.005.

Carlier, J., and N. Burlion (2011), Experimental and numerical assessment of the hydrodynamical properties of cementitious materials, *Transport in Porous Media*, *86*(1), 87–102, doi:10.1007/s11242-010-9607-7.

Carrera, J., X. Sánchez-Vila, I. Benet, A. Medina, G. Galarza, and J. Guinerà (1998), On matrix diffusion: Formulations, solution methods and qualitative effects, *Hydrogeology Journal*, *6*, 178–190.

Chaparro, M. C., and M. W. Saaltink (2014), Modelling of multiphase flow in concrete cells of the radioactive waste storage facility at El Cabril (Spain), *2nd International symposium on cement-based materials for nuclear waste (Nuwcem), Avignon, France*, pp. 1–8.

Chaparro, M. C., M. W. Saaltink, and M. V. Villar (2015), Characterization of concrete by calibrating thermo-hydraulic multiphase flow models, *Transport in Porous Media*, *109*, 147–167, doi:10.1007/s11242-015-0506-9.

Chapwanya, M., J. Stockie, and W. Liu (2009), A model for reactive porous transport during re-wetting of hardened concrete, *Journal of Engineering Mathematics*, *65*(1), 53–73, doi:10.1007/s10665-009-9268-0.

Chen, W., J. Liu, F. Brue, F. Skoczylas, C. A. Davy, X. Bourbon, and J. Talandier (2012), Water retention and gas relative permeability of two industrial concretes, *Cement and Concrete Research*, *42*(7), 1001–1013, doi:10.1016/j.cemconres.2012.04.003.

De Windt, L., F. Marsal, E. Tinseau, and D. Pellegrini (2008), Reactive transport modeling of geochemical interactions at a concrete/argillite interface, tournemire site (france), *Physics and Chemistry of the Earth*, *33*, S295–S305, doi:10.1016/j.pce.2008.10.035.

Dolder, F., U. Mäder, A. Jenni, and N. Schwendener (2013), Experimental characterization of cement-bentonite interaction using core infiltration techniques and 4D computed tomography, *Physics and Chemistry of the Earth, Parts A/B/C*, doi:http://dx.doi.org/10.1016/j.pce.2013.11.002.

Dridi, W. (2013), Analysis of effective diffusivity of cement based materials by multi-scale modelling, *Materials and Structures*, *46*, 313–326, doi:10.1617/s11527-012-9903-5.

Du, X., L. Jin, and G. Ma (2014), A meso-scale numerical method for the simulation of chloride diffusivity in concrete, *Finite Elements in Analysis and Design*, *85*, 87 – 100, doi:http://dx.doi.org/10.1016/j.finel.2014.03.002.

Gamazo, P., M. W. Saaltink, J. Carrera, and P. Zuloaga (2007), Modelación de procesos de evaporación y condensación en el interior de una celda de residuos, *Estudios en la Zona no Saturada del Suelo*, *8*, 319–326.

Garing, C., P. Gouze, M. Kassab, M. Riva, and A. Guadagnini (2015), Anti-correlated porosity-permeability changes during the dissolution of carbonate rocks: Experimental evidences and modeling, *Transport in Porous Media*, *107*, 595–621, doi:10.1007/s11242-015-0456-2.

Goto, S., and D. Roy (1981), Diffusion of ions through hardened cement pastes, *Cement and Concrete Research*, *11*, 751–757.

Gran, M., J. Carrera, S. Olivella, and M. W. Saaltink (2011), Modeling evaporation processes in a saline soil from saturation to oven dry conditions, *Hydrology and Earth System Sciences*, *15*(7), 2077–2089, doi:10.5194/hess-15-2077-2011.

Gran-Esforzado, M. (2015), Coupled heat and water flow dynamics in dry soils. application to a multilayer waste cover., Ph.D. thesis, Universitat Politècnica de Catalunya (UPC).

Grifoll, J., J. M. Gastó, and Y. Cohen (2005), Non-isothermal soil water transport and evaporation, *Advances in Water Resources*, *28*(11), 1254 – 1266, doi:http://dx.doi.org/10.1016/j.advwatres.2005.04.008.

Hadermann, J., and W. Heer (1996), The grimsel (switzerland) migration experiment: integrating field experiments, laboratory investigations and modelling, *Journal of Contaminant Hydrology*, *21*, 87–100, doi:http://dx.doi.org/10.1016/0169-7722(95)00035-6.

Haggerty, R., S. McKenna, and L. Meigs (2000), On the late-time behavior of tracer test breakthrough curves, *Water Resources Research*, *36*, 3467–3479, doi:10.1029/2000WR900214.

Häupl, P., J. Grunewald, H. Fechner, and H. Stopp (1997), Coupled heat air and moisture transfer in building structures, *International Journal of Heat and Mass Transfer*, *40*, 1633 – 1642, doi:http://dx.doi.org/10.1016/S0017-9310(96)00245-1.

Heer, W. (2004), Nuclide transport and diffusion in veins and fracture flow. nagra technical report ntb 04-03., *Tech. rep.*, Nagra, Wettingen, Switzerland.

Ho, C. K., and S. W. Webb (1998), Review of porous media enhanced vapor-phase diffusion mechanisms, models, and data - does enhanced vapor-phase diffusion exist?, *Journal of Porous Media*, *1*(1), 71–92.

Hummel, W., U. Berner, E. Curti, F. Pearson, and T. Thoenen (2002), Nagra/psi chemical thermodynamic data base 01/01, *Tech. rep.*, Universal Publishers/uPUBLISH.com, USA, also published as Nagra Technical Report NTB 02-16, Nagra, Wettingen, Switzerland.

Jakob, A., M. Mazurek, and W. Heer (2003), Solute transport in crystalline rocks at Äspö-II : Blind predictions, inverse modelling and lessons learnt from test {STT1}, *Journal of Contaminant Hydrology*, *61*, 175 – 190, doi:http://dx.doi.org/10.1016/S0169-7722(02)00136-5.

Jenni, A., U. Mäder, C. Lerouge, S. Gaboreau, and B. Schwyn (2013), In situ interaction between different concretes and opalinus clay, *Physics and Chemistry of the Earth, Parts A/B/C*, doi:http://dx.doi.org/10.1016/j.pce.2013.11.004.

Kamali-Bernard, S., F. Bernard, and W. Prince (2009), Computer modelling of tritiated water diffusion test for cement based materials, *Computational Materials Science*, *45*, 528–535.

Khan, M. I. (2002), Factors affecting the thermal properties of concrete and applicability of its prediction models, *Building and Environment*, *37*(6), 607 – 614, doi: 10.1016/S0360-1323(01)00061-0.

Kim, K.-H., S.-E. Jeon, J.-K. Kim, and S. Yang (2003), An experimental study on thermal conductivity of concrete, *Cement and Concrete Research*, *33*(3), 363 – 371, doi:10.1016/S0008-8846(02)00965-1.

Kosakowski, G., and U. Berner (2013), The evolution of clay rock/cement interfaces in a cementitious repository for low- and intermediate level radioactive waste, *Physics and Chemistry of the Earth*, *64*, 65–86, doi:10.1016/j.pce.2013.01.003.

Kulik, D. c., and M. Kersten (2001), Aqueous solubility diagrams for cementitious waste stabilization systems: Ii, end-member stoichiometries of ideal calcium silicate hydrate solid solutions, *Journal of the American Ceramic Society*, *84*, 3017–3026.

Leech, C., D. Lockington, and R. D. Hooton (2006), Estimation of water retention curve from mercury intrusion porosimetry and van genuchten model, *ACI Structural Journal*, *103*(2), 291–295.

Liu, J., H. Aizawa, and H. Yoshino (2004), CFD prediction of surface condensation on walls and its experimental validation, *Building and Environment*, *39*, 905 – 911, doi: http://dx.doi.org/10.1016/j.buildenv.2004.01.015.

Lothenbach, B., and F. Winnefeld (2006), Thermodynamic modelling of the hydration of portland cement, *Cement and Concrete Research*, *36*(2), 209 – 226, doi:10.1016/j.cemconres.2005.03.001.

Lothenbach, B., T. Matschei, G. Möschner, and F. P. Glasser (2008), Thermodynamic modelling of the effect of temperature on the hydration and porosity of portland cement, *Ce-*

ment and Concrete Research, *38*, 1–18, doi:http://dx.doi.org/10.1016/j.cemconres.2007.08.017.

Lü, X. (2002), Modelling of heat and moisture transfer in buildings: I. model program, *Energy and Buildings*, *34*, 1033 – 1043, doi:http://dx.doi.org/10.1016/S0378-7788(02)00021-X.

Mäder, U., H. Waber, and A. Gautschi (2004), New method for porewater extraction from claystone and determination of transport properties with results for Opalinus Clay (Switzerland), *In: Wanty, R.B., Seal, R.R. (Eds.), Proceedings WRI-10 (11th International Symposium on Water-Rock Interaction). Balkema, Saratoga Springs, New York, USA*, pp. 445–448.

Mäder, U., T. Fierz, B. Frieg, J. Eikenberg, M. Rüthi, Y. Albinsson, A. Möri, S. Ekberg, and P. Stille (2006), Interaction of hyperalkaline fluid with fractured rock: Field and laboratory experiments of the HPF project (Grimsel Test Site, Switzerland), *Journal of Geochemical Exploration*, *90*, 68–94.

Mainguy, M., O. Coussy, and V. Baroghel-Bouny (2001), Role of air pressure in drying of weakly permeable materials, *Journal of Engineering Mechanics-ASCE*, *127*(6), 582–592, doi:10.1061/(ASCE)0733-9399(2001)127:6(582).

Marquardt, D. (1963), An algorithm for least-squares estimation of nonlinear parameters, *Journal of the Society for Industrial and Applied Mathematics*, *11*, 431–441, doi:10.1137/0111030.

Marshall, A. L. (1972), The thermal properties of concrete, *Building Science*, *7*(3), 167 – 174, doi:10.1016/0007-3628(72)90022-9.

Massana, J., and M. W. Saaltink (2006), Modelo 2D de la celda 16, report, *Tech. rep.*, Dept. Geotechnical Engineering and Geosciences, Universitat Politècnica de Catalunya.

Monlouis-Bonnaire, J. P., J. Verdier, and B. Perrin (2004), Prediction of the relative permeability to gas flow of cement-based materials, *Cement and Concrete Research*, *34*(5), 737 – 744, doi:10.1016/S0008-8846(03)00071-1.

Olivella, S., J. Carrera, A. Gens, and E. E. Alonso (1994), Non-isotermal multiphase flow of brine and gas through saline media, *Transport in Porous Media*, *15*, 271–293, doi: 10.1016/0148-9062(95)93271-P.

Olivella, S., J. Carrera, A. Gens, and E. Alonso (1996a), Porosity variations in saline media caused by temperature gradients coupled to multiphase flow and dissolution/precipitation, *Transport in Porous Media*, *25*(1), 1–25, doi:10.1007/BF00141260.

Olivella, S., A. Gens, J. Carrera, and E. E. Alonso (1996b), Numerical formulation for a simulator (code_bright) for the coupled analysis of saline media, *Engineering Computations*, *13*(7), 87–112, doi:10.1108/02644409610151575.

Parkhurst, D. L., and C. Appelo (1999), *User's Guide to PHREEQC (Version 2) - A Computer Program for Speciation, Batch-reaction, One-dimensional Transport, and Inverse Geochemical Calculations.*, US Geol. Surv. Water-Resour. Invest. Rep. 99-4259.

Pfingsten, W., B. Paris, J. Soler, and U. Mäder (2006), Tracer and reactive transport modelling of the interaction between high-ph fluid and fractured rock: Field and laboratory experiments, *Journal of Geochemical Exploration*, *90*, 95–113, doi:10.1016/j.gexplo. 2005.09.009.

Pintado, X., A. Ledesma, and A. Lloret (2002), Backanalysis of thermohydraulic bentonite properties from laboratory tests, *Engineering Geology*, *64*(2-3), 91–115, doi:10.1016/ S0013-7952(01)00110-7.

Poyet, S. (2009), Experimental investigation of the effect of temperature on the first des-

orption isotherm of concrete, *Cement and Concrete Research*, *39*(11), 1052 – 1059, doi: http://dx.doi.org/10.1016/j.cemconres.2009.06.019.

Poyet, S. (2013), Determination of the intrinsic permeability to water of cementitious materials: Influence of the water retention curve, *Cement and Concrete Composites*, *35*(1), 127–135, doi:10.1016/j.cemconcomp.2012.08.023.

Saaltink, M. W. (2006), Modelos bidimensionales de posibles medidas de remediación en las celdas de cabril, *Tech. rep.*, Dept. Geotechnical Engineering and Geosciences, Universitat Politècnica de Catalunya.

Saaltink, M. W., F. Batlle, C. Ayora, J. Carrera, and S. Olivella (2004), Retraso, a code for modeling reactive transport in saturated and unsaturated porous media, *Geologica Acta*, *2*, 235–251.

Saaltink, M. W., X. Sánchez-Vila, and J. Carrera (2005), Estudio cualitativo sobre la posibilidad que el agua recogida en la celda 16 proceda de un proceso de condesación, report, *Tech. rep.*, Dept. Geotechnical Engineering and Geosciences, Universitat Politècnica de Catalunya.

Sakai, M., N. Toride, and J. Šimůnek (2009), Water and vapor movement with condensation and evaporation in a sandy column, *Soil Science Society of America Journal*, *73*, 707–717, doi:10.2136/sssaj2008.0094.

Savage, D., et al. (2011), A comparative study of the modelling of cement hydration and cement-rock laboratory experiments, *Applied Geochemistry*, *26*, 1138–1152, doi: 10.1016/j.apgeochem.2011.04.004.

Scrivener, K., A. Crumbie, and P. Laugesen (2004), The interfacial transition zone (ITZ) between cement paste and aggregate in concrete, *Interface Science*, *12*, 411–421, doi: 10.1023/B:INTS.0000042339.92990.4c.

Slooten, L. J., F. Batlle, and J. Carrera (2010), An XML based problem solving evirontment for hydrological problems, *XVIII International Conference on Water Resources (CMWR), Barcelona, Spain*, pp. 1–8.

Soler, J. (2012), High-ph plume from low-alkali-cement fracture grouting: Reactive transport modeling and comparison with ph monitoring at ONKALO (finland), *Applied Geochemistry*, *27*, 2096–2106, doi:10.1016/j.apgeochem.2012.05.014.

Soler, J., M. Vuorio, and A. Hautojärvi (2011), Reactive transport modeling of the interaction between water and a cementitious grout in a fractured rock. application to ONKALO (finland), *Applied Geochemistry*, *26*, 1115–1129, doi:10.1016/j.apgeochem.2011.04.001.

Soler, J. M. (2013), Reactive transport modeling of concrete-clay interaction during 15 years at the tournemire underground rock laboratory, *European Journal of Mineralogy*, *25*, 639–654, doi:10.1127/0935-1221/2013/0025-2324.

Soler, J. M. (2016), Two-dimensional reactive transport modeling of the alteration of a fractured limestone by hyperalkaline solutions at maqarin (jordan), *Applied Geochemistry*, *66*, 162–173, doi:http://dx.doi.org/10.1016/j.apgeochem.2015.12.012.

Soler, J. M., and U. K. Mäder (2007), Mineralogical alteration and associated permeability changes induced by a high-ph plume: Modeling of a granite core infiltration experiment, *Applied Geochemistry*, *22*, 17 – 29, doi:http://dx.doi.org/10.1016/j.apgeochem.2006.07.015.

Soler, J. M., and U. K. Mäder (2010), Cement-rock interaction: Infiltration of a high-ph solution into a fractured granite core, *Geologica Acta*, *8*, 221–233, doi:DOI:10.1344/105.000001531.

Taylor, H. F. W. (1997), *Cement Chemistry*, Thomas Telford Ltd.

Tits, J., A. Jakob, E. Wieland, and P. Spieler (2003), Diffusion of tritiated water and $^{22}Na^{+}$ through non-degraded hardened cement pastes, *Journal of Contaminant Hydrology*, *61*, 45–62.

Trapote-Barreira, A. (2015), Dissolution kinetics of c-s-h gel and durability of mortar, Ph.D. thesis, Universitat Politècnica de Catalunya.

Trapote-Barreira, A., J. Cama, and J. Soler (2014), Dissolution kinetics of c-s-h gel: Flow-through experiments, *Physics and Chemistry of the Earth*, *70-71*, 17–31, doi:10.1016/j.pce.2013.11.003.

Šelih, J., A. C. M. Sousa, and T. W. Bremner (1996), Moisture transport in initially fully saturated concrete during drying, *Transport in Porous Media*, *24*(1), 81–106, doi:10.1007/BF00175604.

Van Genuchten, M. T. (1980), A closed-form equation for predicting the hydraulic conductivity of unsaturated soils, *Soil Science Society of America Journal*, *44*(5), 892–898.

Villar, M. V., and F. J. Romero (2014), Determination of water retention curves of concrete, *2nd International symposium on cement-based materials for nuclear waste (Nuwcem), Avignon, France*, pp. 1–9.

Villar, M. V., P. L. Martín, and J. M. Barcala (2009), Caracterización del material de cobertera y el hormigón del C.A. El Cabril, *Technical report CIEMAT/DMA/2G205/03/09*, CIEMAT, Madrid, 55 pp.

Villar, M. V., P. L. Martín, F. J. Romero, V. Gutiérrez-Rodrigo, and J. M. Barcala (2012), Gas and water permeability of concrete, *Informes técnicos CIEMAT 1261*, CIEMAT, Madrid, 45 pp.

Wardeh, G., and B. Perrin (2006), Relative permeabilities of cement-based materials: Influence of the tortuosity function, *Journal of Building Physics*, *30*(1), 39–57, doi: 10.1177/1744259106064597.

Wolery, T. J., K. J. Jackson, W. L. Bourcier, C. J. Bruton, B. E. Viani, K. G. Knauss, and J. M. Delany (1990), Current status of the eq3/6 software package for geochemical modeling, *Chemical Modeling of Aqueous Systems II*, pp. 104–116, doi:doi:10.1021/bk-1990-0416.ch008.

Wu, M., B. Johannesson, and M. Geiker (2014), A study of the water vapor sorption isotherms of hardened cement pastes: Possible pore structure changes at low relative humidity and the impact of temperature on isotherms, *Cement and Concrete Research*, *56*(0), 97 – 105, doi:http://dx.doi.org/10.1016/j.cemconres.2013.11.008.

Zuloaga, P., C. Andrade, and M. W. Saaltink (2006), Long term water flow scenario in low-level waste disposal vaults, with particular regard to concrete structures en El Cabril, Cordoba, Spain., *J.Phys IV, France*.